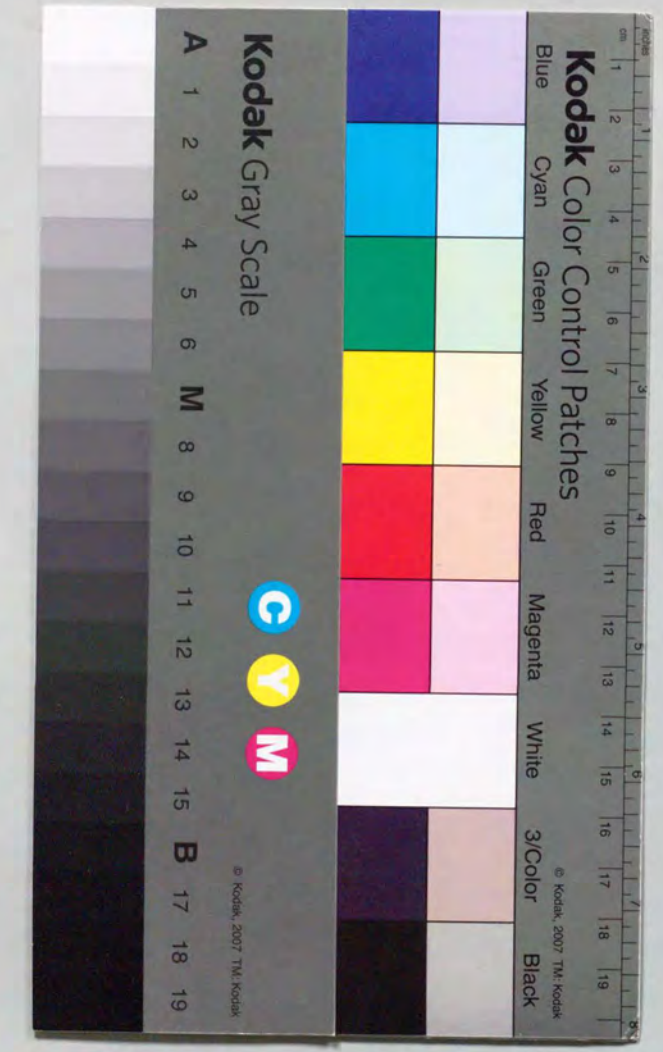

学　位　論　文

"Search for Scalar and Vector Leptoquarks in Electron-Proton Collisions at $\sqrt{S}$ = 300 GeV"

「重心系エネルギー 300 GeV の電子・陽子衝突におけるスカラー及びベクターレプトクォークの探索」

平成５年６月 博士（理学）申請

東京大学大学院 理学系研究科
物理学専攻

羽澄 昌史

Search for Scalar and Vector Leptoquarks in Electron-Proton Collisions at $\sqrt{S} = 300\ GeV$

Masashi Hazumi

Graduate School
University of Tokyo
7-3-1, Hongo
Bunkyo-ku, Tokyo, 113, Japan

A thesis submitted in partial fulfillment
of the requirements
for the degree of doctor of science

June 3, 1993

Abstract

A search for a resonant state coupled to an electron-quark pair has been performed using collisions of the electron beam of 26.7 GeV and the proton beam of 820 GeV. With the integrated luminosity of $26.6 \pm 1.6\ nb^{-1}$, scalar and vector leptoquarks have been searched for in the neutral current and charged current samples. The selected events agreed well with the prediction of the Standard Model, and no evidence has been found for production of leptoquarks decaying into $e^- + jet$ or $\nu + jet$. Limits on the coupling strength of scalar (vector) leptoquarks to electron and quark have been determined for masses from 50 (40) GeV to 225 GeV. A limit on the leptoquark mass has been also obtained at the 95% confidence level assuming that either left-handed or right-handed coupling exists to the electron-quark pair with electroweak strength. The mass limit depends on the cross section determined by the choice of quantum numbers. Leptoquarks are ruled out for masses below 216 GeV with the largest cross section and below 105 GeV with the smallest cross section.

Contents

List of Tables

List of Figures

Chapter 1

Introduction

A particle collider has been one of the central tools to understand elementary particles and their interactions especially in recent 20 years. In November 1974, a new sharp resonance with a mass of 3.1 GeV was discovered simultaneously by two different experiments; one e^+e^- annihilations at SLAC [1] and the other electron pair productions from a beryllium target with a proton beam at BNL [2]. This J/Ψ resonance was also confirmed by other e^+e^- experiments at FRASCATI [3] and DESY [4]. Some successive works including the discovery of the corresponding resonance Ψ' [5], studies of inclusive electron events [6] and decays of D-mesons [7] revealed that J/Ψ is a bound state of a charm and an anti-charm quark.

In 1975, the SLAC-LBL group found events of the form $e^+ + e^- \rightarrow e^\pm + \mu^\mp +$ missing energy, again with the e^+e^- collider SPEAR at SLAC. The observed events were consistent with the pair production of a new lepton τ decaying into $e\nu\nu$ and $\mu\nu\nu$. This interpretation was confirmed with the successive studies of two-charged prong leptonic events in e^+e^- annihilations [8] and the measurement of tau decay branching ratios [9].

Yet another big discovery with an e^+e^- experiment took place in 1979. With the benefit of high total center-of-mass energy (more than 30GeV) of the e^+e^- collider PETRA at DESY, all the four detectors TASSO, PLUTO, MARK J, and JADE found clear 3-jet events which are the evidence of gluon bremsstrahlung [10]. The characteristics of the events agreed with the predictions of quantum chromodynamics (QCD).

Colliders with proton and anti-proton beams also gave striking results. In 1983, UA1 and UA2 detectors at the $p\bar{p}$ collider S$p\bar{p}$S at CERN caught the signal of the intermediate vector boson postulated by the unified theory of weak and electromagnetic interactions [11]. The measured masses of $W^\pm$ and Z^0 were in good agreement with the predictions of the Weinberg-Salam model [12].

The above history is not the whole story, but the quite important part to construct the Standard Model of elementary particle physics. Nowadays new e^+e^- and $p\bar{p}$ colliders

with higher and higher energy such as LEP, SLC, Tevatron are in operation, which aim to test the Standard Model more precisely as well as search for new phenomena beyond the Standard Model.

While experiments at these colliders are being carried on, there exists another stream; the lepton-nucleon scattering. This method has long been the best way to study the inner structure of protons and neutrons. In 1969, SLAC-MIT group succeeded to observe electrons scattered from a proton deeply inelastically, up to $7.4GeV^2$ of squared momentum-transfer (Q^2) beyond the resonance region [13]. The cross section did not depend on Q^2 greatly, which meant that a proton could not be regarded as a simple electromagnetic cloud. The systematic study of inelastic scattering suggested the existence of a core-like object inside a proton. The same behavior was also observed at neutrino-nucleon scattering experiments [14] (which also led to a discovery of the neutral current scattering [15]). Right after SLAC-MIT group presented the result, R. P. Feynman advocated the 'parton model' [16], in which a proton is regarded as 'gas of partons'. A parton is a hypothetical point-like particle which does not interact each other, does not have a specific mass, nor momentum transverse to the proton momentum. There is no constraint on the number of partons inside a proton. The only constraint is that the net 4-momentum of partons should be equal to that of a proton. A deep inelastic scattering (DIS) between an electron and a proton is interpreted as the elastic scattering between the electron and a parton. Thus the scaling behavior appears automatically as a nature of the interaction between point-like particles. The inelasticity of the reaction is attributed to the mass (or energy) of the struck parton. This simple but rather bold model could explain the qualitative features of DIS phenomena. However, more fundamental understanding was postponed until 1973, when the 'asymptotic freedom' of QCD was discovered by young theoretical physicists [17]. The asymptotic freedom means that the strong interaction becomes weaker when particles are getting closer, and thus the particles asymptotically become free from the influence of other particles. QCD is a quantum field theory to describe the strong interaction with SU(3) local gauge symmetry. The interaction of particles with 'color charge' is mediated by 'gluons', which also have color by nature of the non-Abelian symmetry. As a result, a gluon is able to emit gluons which finally makes anti-shielding color cloud. This is the origin of the asymptotic freedom. The situation is the opposite to the case in QED.[1] This feature is consistent with the naive parton model where partons do not interact inside a proton. By identifying the partons as quarks and gluons, the quark-parton model based upon QCD became the most promising theory to describe the inner structure of the nucleons. In addition, the weak violation of the scaling law can be calculated with this model, and can reproduce the experimental results on the Q^2 dependence of the structure functions up to $Q^2 \sim 300GeV^2$. As the summary, the

[1]The color cloud by quarks shields a bare charge as the case in QED. Therefore asymptotic freedom breaks down if there are 16 or more flavors of quarks.

fixed-target lepton-nucleon scattering experiments have also played a very important role in the construction of the Standard Model, as well as the collider experiments.

HERA, the first electron-proton collider in the world, is a meeting point of these two trends. On one hand, HERA is a 'super-microscope' to look into the structure of protons. With proton beam energy of 820GeV and electrons of 26.7GeV so far obtained, the maximum momentum transfer is $\sim 10^5 GeV^2$ which corresponds to a resolving power of $\sim 10^{-18}$ cm. On the other hand, HERA can be regarded as an 'electron-quark collider' to search for new particles beyond the Standard Model with masses of up to $\sim$ 300 GeV. Among a lot of predicted new particles, leptoquarks are the most suitable objects for HERA since the signal would be a sharp resonance of the electron-quark state. The main motivation of HERA is to study the inner structure of protons which is to be described with the quark-parton model and QCD. It may find, however, a new resonance by leptoquarks which is beyond the Standard Model. In fact we already encountered the similar situation: The main motivation of the experiment at BNL in 1974 was to study the Drell-Yan process described with the quark-parton model. It found, however, the J/Ψ resonance which was beyond the standard SU(3) symmetry framework at that time.

After a long construction period, the ZEUS detector at HERA observed the first luminosity on 31 May 1992, and since then it recorded data of $32.6nb^{-1}$ in 1992. In this thesis, the search for leptoquarks is carried out with all good luminosity data in 1992 with integrated luminosity of $26.6 \pm 1.6nb^{-1}$. In Chapter 2, the standard and exotic physics at HERA are explained with the special emphasis on leptoquarks. In Chapters 3 and 4, the experimental apparatus and the ZEUS data taking system are described. Since the author has been working in the Global First Level Trigger (GFLT) group, and GFLT played the essential role in the data taking in 1992, the principle and performance of GFLT are described in detail. After explaining the ZEUS offline software and Monte Carlo technique in Chapter 5, the analysis and results are given in Chapters 6 and 7.

Chapter 2

Physics at HERA

2.1 Deep Inelastic Scattering at HERA

The main motivation of HERA is to observe deep inelastic scattering (DIS) process

$$e + p \to l + X$$

where l is the scattered lepton (e or ν_e) and X the final hadronic system. Fig. 2.1 is a diagram of this process. Generally the final-state hadronic system X consists of a current jet originating from a struck parton, and remnant particles. An interaction mediated by a neutral vector boson (γ or Z^0) is called the neutral current (NC) process. The charged current (CC) process is mediated by the exchange of a W boson.

The kinematics of DIS process is completely determined by any combination of two independent variables. One of such variables often used is the squared-momentum transfer (Q^2):

$$Q^2 \equiv -q^2 = -(p_e - p_l)^2$$

where p_e and p_l are the 4-momenta of the beam electron and the scattered lepton. The variable ν is also commonly used and can be interpreted as the energy transfer to the final-state hadronic system in the proton rest frame:

$$\nu \equiv \frac{P \cdot q}{M_P}$$

where P and M_P are 4-momentum and mass of the beam proton. Yet other convenient variables are Bjorken-x and y:

$$x \equiv \frac{Q^2}{2P \cdot q} = \frac{Q^2}{2M_P \nu}$$

$$y \equiv \frac{P \cdot q}{P \cdot p_e} = \frac{2P \cdot q}{s}$$

where $s(= (p_e + P)^2)$ is the total invariant mass squared. According to the parton description, the 4-momentum of the parton on interaction is xP, i.e. x is regarded as the momentum fraction of the parton.[1] In the proton rest frame, $(1 - y)$ is regarded as the elasticity because

$$1 - y = \frac{E_{l'}}{E_e},$$

where E_e is the energy of the beam electron and $E_{l'}$ the energy of the scattered lepton. Conventionally the combination (x, Q^2) or (x, y) is used most frequently to determine event kinematics. With neglecting the mass of electron, the physically-allowed ranges of these variables are as follows [18]:

$$0 \leq x \leq 1, \quad 0 \leq y \leq 1, \quad 0 \leq Q^2 \leq 2M_P\nu, \quad 0 \leq \nu \leq (s - M_P^2)/2M_P.$$

The cross section of the neutral current electron-proton scattering is expressed generally with the product of the electron tensor ($L^e_{\mu\nu}$) and the hadron tensor ($W^{\mu\nu}$):

$$d\sigma \sim L^e_{\mu\nu} W^{\mu\nu}.$$

In the above formula, other factors not important in the current argument are omitted for simplicity. The electron tensor is obtained with $L^e_{\mu\nu} \sim j_\mu j_\nu$, where $j_\mu \sim \bar{u}_e \gamma_\mu u_e$ is the electron current. To determine the hadron tensor, we have to consider how to describe the structure of a proton. In case of the elastic scattering, $e + p \to e + p$, where the final state proton is not destroyed, the structure of a proton is described with form factors based upon an idea that a proton is 'an electromagnetic cloud'. Then the hadron tensor is obtained in a similar manner to the electron tensor; i.e. $W^{\mu\nu} \sim J^\mu J^\nu$ where $J^\mu \sim \bar{u}_P \Gamma^\mu u_P$ is the proton current and the generalized vertex factor Γ^μ is described with the form factors. In case of DIS, however, the proton is destroyed into hadrons in the final state. Therefore not the vertex factor but the hadron tensor itself should be parametrized. The form of the hadron tensor is obtained with some general constraints [19]. First of all, it must be formed in terms of the four-momenta P and q only. The most general tensor with this constraint is a linear combination of $g^{\mu\nu}$, $P^\mu P^\nu$, $q^\mu q^\nu$, $P^\mu q^\nu$, $q^\mu P^\nu$ and $\varepsilon^{\mu\nu\alpha\beta} P_\alpha q_\beta$. From the electron current conservation, however, we obtain $L^e_{\mu\nu} q^\mu = L^e_{\mu\nu} q^\nu = 0$ and hence only three terms survive in the most general expression of $W^{\mu\nu}$:

$$W^{\mu\nu} = c_1 F_1(x, Q^2) g^{\mu\nu} + c_2 F_2(x, Q^2) P^\mu P^\nu + c_3 F_3(x, Q^2) \varepsilon^{\mu\nu\alpha\beta} P_\alpha q_\beta,$$

where the dimensionless coefficients $F_1(x, Q^2)$, $F_2(x, Q^2)$ and $F_3(x, Q^2)$ are so called 'structure functions' which are measured experimentally and express the structure of a proton.[2]

[1] This is derived from the massless condition of the scattered parton; i.e. $(xP + q)^2 = 0$.

[2] The coefficients c_1, c_2 and c_3 contain rest of the required factors.

Then we obtain the differential cross section of the DIS process, $e^- + p \to e^- + X$, in leading order standard electroweak theory [20]:

$$\frac{d^2\sigma_{NC}}{dxdQ^2} = \frac{4\pi\alpha^2}{xQ^4}[y^2xF_1(x,Q^2) + (1-y)F_2(x,Q^2) + (y - \frac{y^2}{2})xF_3(x,Q^2)].$$

The contributions from both γ and Z^0 are contained in the cross section. The pure γ exchange dominates at low Q^2. However, in the Q^2 region at HERA, both the γ/Z^0 interference term and the pure Z^0 exchange term become important as shown in Fig. 2.2 [20].

In the above cross section formula, three variables, x, y and Q^2, are used simultaneously for convenience. But any one of them can be replaced using the following equation:

$$s \cdot x \cdot y = Q^2.$$

Related to this equation, we show in Fig. 2.3 the accessible kinematical region at HERA. It is clearly seen that HERA can access a completely new region. With the design luminosity ($200pb^{-1}/year$), the number of NC events is expected to be $O(10^7)/year$ in the region defined with $Q^2 > 4GeV^2$ and $x > 10^{-3}$.

According to the parton model, the structure functions can be replaced by more fundamental 'parton density functions'. In the naive parton model where partons do not interact with each other, we can regard the DIS process as the reaction $e + parton \to e + parton$ assuming that the four-momentum of the parton is xP. The cross section is calculated in the similar way to the reaction of two pointlike particles such as $e + \mu \to e + \mu$, except the fact that we have to introduce the 'parton density function' which gives the probability of the parton having the momentum xP. For simplicity, first we consider the pure γ exchange process which was dominant in the DIS experiments before HERA. Assuming that the spin of a parton is $1/2$, we obtain the following relations:

$$F_2(x) = \sum_i e_i^2 x f_i(x)$$

$$2xF_1(x) = F_2(x)$$

$$F_3(x) = 0$$

where $f_i(x)$ is the density function of parton i, and e_i is its charge. From the first equation, it is seen that we can obtain the parton density function by the measurement of $F_2(x)$. The second equation is known as the Callan-Gross relation [21]. $F_3(x) = 0$ comes from the parity conservation. One remarkable feature is that once we fix the variable x, the structure functions (and consequently the cross section) do not depend on Q^2 any more. This phenomenon is known as 'Bjorken scaling' which is understood in the following way: The photon couples to the charge of the target and probes the interior of the target at a distance of $\sim 1/\sqrt{Q^2}$. As described in Fig. 2.4 (a), if the target is 'a cloud of charge',

F_2 falls off as Q^2 increases since the photon couples to the smaller fraction of the total charge of the target. But the coupling and resulting F_2 do not depend on Q^2 if the target is made of pointlike partons with specific charges as shown in Fig. 2.4 (b).

In the QCD-based parton model, however, the density of partons (= quarks and gluons) again shows a weak Q^2 dependence originating from the fact that a quark can emit and absorb gluons as described in Fig. 2.4 (c). As a result, the NC structure functions in leading order QCD are [20]

$$F_2(x,Q^2) = \sum_f A_f(Q^2)[xq_f(x,Q^2) + x\bar{q}_f(x,Q^2)]$$

$$F_2(x,Q^2) - 2xF_1(x,Q^2) = F_L(x,Q^2)$$

$$xF_3(x,Q^2) = \sum_f B_f(Q^2)[xq_f(x,Q^2) - x\bar{q}_f(x,Q^2)]$$

where $q_f(x,Q^2)$ and $\bar{q}_f(x,Q^2)$ are quark and antiquark density functions.

$$A_f(Q^2) = e_f^2 - 2e_f v_e v_f P_Z + (v_e^2 + a_e^2)(v_f^2 + a_f^2)P_Z^2$$

$$B_f(Q^2) = -2e_f a_e a_f P_Z + 4v_e v_f a_e a_f P_Z^2$$

are flavour-dependent coefficients written with the electric charge e_f, the NC vector and axial vector couplings of quarks (v_f and a_f) and electrons (v_e and a_e), and P_Z is the ratio of the Z and γ propagators, i.e. $P_Z = Q^2/(Q^2 + m_Z^2)$. The couplings, v_f, a_f, v_e and a_e, are expressed as follows:

$$v_{f(e)} = (T_{3f(e)} - 2e_{f(e)}\sin^2\theta_W)/\sin 2\theta_W$$

$$a_{f(e)} = T_{3f(e)}/\sin 2\theta_W$$

where $T_{3f(e)}$ is the third component of the weak isospin and θ_W is the Weinberg angle. The longitudinal structure function $F_L(x,Q^2)$ appears in next to leading order QCD and is very small except in the low-x region.

Similar to the NC process, the cross section of the CC process $e^- + p \to \nu_e + X$ is also given with parton density functions [20]:

$$\frac{d^2\sigma_{CC}}{dxdQ^2} = \frac{\pi\alpha^2}{4\sin^4\theta_W(Q^2 + m_W^2)^2}\sum_{i,j}[|V_{u_i d_j}|^2 u_i(x,Q^2) + (1-y)^2|V_{u_j d_i}|^2 \bar{d}_i(x,Q^2)]$$

where $V_{u_i d_j}$ are elements of the Kobayashi-Maskawa matrix, u_i and d_i are the up- and down-type quark flavours (u,c) and (d,s), respectively, and i, j are family indices. With the design luminosity, the number of CC events is expected to be $O(10^4)/year$ in the region defined with $Q^2 > 4GeV^2$ and $x > 10^{-3}$.

Finally we discuss the qualitative features of parton density functions. Quantitative parameterizations will be explained in Chapter 5. According to the quark-parton model, a

proton primarily consists of two u-quarks and a d-quark which are called 'valence quarks'. In addition, quark-antiquark pairs, called 'sea quarks', are created through the gluon emission[3]. The density functions of the sea quarks increase rapidly at $x \sim 0$ and are suppressed strongly at $x \sim 1$. On the valence quarks, both u-quark and d-quark have components in high-x region, but experimental studies of the ratio of the neutron and proton structure functions indicated $u \gg d$ at $x \sim 1$ [22][23], which is lower than the expectation of the naive parton model, $u = 2d$. As a summary, the qualitative features of the parton density functions of u, d, s quarks and their antiquarks are as follows[4]:

$$u \gg d \gg \bar{u} \sim \bar{d} \sim s \sim \bar{s}$$

in high-x region and

$$u \sim d \sim \bar{u} \sim \bar{d} \sim s \sim \bar{s}$$

in low-x region. These are related directly to the production cross section of leptoquarks which will be discussed in Section 2.4.

2.2 Photoproduction at HERA

If the scattering angle of the final state electron in the neutral current process is very small, the electron goes down to the beampipe and is invisible with the main detector. In this case, Q^2 is very small and the exchanged particle is an almost real photon. Such a process has different features from the DIS process and is called 'photoproduction'. The photoproduction total cross section has been already measured at HERA. The result with the ZEUS detector is $154 \pm 16(stat.) \pm 32(syst.)\mu b$ in the γp centre of mass energy range $186 - 233GeV$ [24]. This is much larger than the cross section of the DIS process. Therefore we have to take care of the contamination of photoproduction events when we select DIS events, though the event shape is different and the contamination efficiency is expected to be low.

2.3 Exotic physics at HERA

Among various channels of exotic physics at HERA, there are three event types which can have sizable effects:

1. Virtual exchange of a new particle (Fig. 2.5 (a)).
   This can be checked by measuring differential cross sections of neutral and charged current events precisely. The deviation from the prediction of the Standard Model then indicates some new physics. For example, extra gauge bosons coming from higher symmetries can be found with this method provided that enough integrated luminosity is achieved after a few years of data taking.

2. Pair production of new particles via boson-gluon fusion (Fig. 2.5 (b)).
   In the γ/Z^0 boson-gluon fusion, the quantum numbers of the new particle can be cancelled out with its anti-particle. Therefore this channel allows us to access various kinds of new particles such as top-quarks, leptoquarks in 2nd and 3rd generation, and so on. In case of the W boson-gluon fusion, it is also possible to create a pair of top and anti-bottom quarks for example. However, the cross section usually falls down steeply with increasing mass of the new particles. Hence generally it is difficult to search for a new particle with a mass greater than 100 GeV with this channel.

3. Production of a new particle associated with the initial electron (Fig. 2.5 (c)).
   This channel makes it possible to search for a new particle with mass of up to the kinematical limit. One constraint is that the new particle has to have the 'electron number' unless the lepton number conservation is broken. Table2.1 shows a rough estimation of cross sections of some new particles accessible in this channel [25], together with expected number of events in the ZEUS data in 1992. In the table some arbitral parameters such as the mass of the particle are chosen to be around the present experimental bounds. It should be emphasized that leptoquarks can show the most outstanding effect if they exist.

2.4 Leptoquark

2.4.1 Theoretical motivation

Leptoquarks (LQ in the following) are hypothetical bosons which carry both baryon number and lepton number, directly couple to lepton and quark, and are triplets under $SU(3)_C$. In the Standard Model, quarks and leptons are completely independent. There is no direct coupling between them. In a theoretical point of view, however, the direct interaction between quarks and leptons mediated by LQ is often inevitable when one considers an extension of the Standard Model. For example, in case of various grand unified theories (GUTs) [26], quarks and leptons are no longer treated separately, but are likely to be in the same representation. Then the transition between quarks and leptons are mediated by LQ with a mass around the considered symmetry breaking scale.

One may claim that such LQ can cause a proton decay and thus should be very massive, i.e. around the GUT scale like X and Y bosons in the naive SU(5) GUT. However, LQ with conserving baryon number and lepton number do not mediate the proton decay, and

[3] Gluons themselves are also regarded as partons in the QCD-based quark-parton model.

[4] The density of heavy quarks (c and b) are very small because of its mass.

the mass of LQ (M_{LQ} in the following) can be of order 100 GeV [27]. There are various models which allow this type of LQ. The following are some examples:

- In superstring-inspired E_6 models [28], a scalar isosinglet LQ with electric charge $\pm 1/3$ is contained, but it is possible to avoid the proton decay since the baryon number violating couplings can be prohibited from a discrete symmetry [29]. The condition, $M_{LQ} = O(100GeV)$, is allowed in this case.

- An interesting extension of the SU(5) GUT has been proposed recently [30]. By putting a pair of LQ with $M_{LQ} = O(100GeV)$ by hand into the SU(5) GUT lagrangian, all experimental results become consistent with the minimal SU(5) GUT. Thus SU(5) GUT can be 'saved' by the LQ.[5] This is a very economical model in the sense that the number of extra particles is much smaller than that in any other models like the supersymmetric SU(5) or SO(10).

- Light LQ are also introduced in Technicolor theories [32]. The main motivation of Technicolor theories is to reduce the number of arbitrary parameters in the Standard Model by replacing the elementary Higgs field by some composite field. A new set of particles, called techniquarks and technileptons, is introduced under some new global gauge symmetry (usually SU(N) with N technifermions). The symmetry breaking scale of Technicolor is usually $\sim 1TeV$ to obtain the correct masses of weak bosons [19]. Below the symmetry breaking scale, some pseudo-Goldstone bosons can be regarded as LQ since they couple to a quark-lepton pair. The mass of such LQ is rather light; e.g. $M_{LQ} = 160\sqrt{\frac{4}{N}}$ (GeV) in the Farhi-Susskind model [32].

- In some composite models, it is also possible to form LQ which are not Goldstone bosons. For example, there is a study by J. Wudka [33] in which light LQ appear in the context of the Abbott-Farhi model [34] where all physical particles must be $SU(2)_L$ singlets. Ordinary left-handed fermions are bound states of a left-handed preonic fermion and the fundamental scalar. In addition, LQ are also introduced as the bound states of two preons or of a preon and an anti-preon.

2.4.2 Characteristics in e-p collisions

The main feature of LQ at HERA is that it can be observed as an s-channel resonance as shown in Fig. 2.6. The parton on interaction has a momentum fraction x which ranges from 0 to 1. This means that we can scan the resonant peak in x distribution. If LQ exist, we would observe a peak at

$$x_{LQ} = \frac{M_{LQ}^2}{s}.$$

[5]This result is independent of the magnitude of the lepton-quark coupling [31].

The production cross section and the width of the LQ resonance are strongly model-dependent. Instead of assuming a specific model, here we consider an effective lagrangian with the most general dimensionless, $SU(3) \times SU(2) \times U(1)$ invariant couplings of scalar and vector LQ which satisfy baryon and lepton number conservation [35]. According to this lagrangian, there are 10 types of LQ as listed in Table 2.2. In the table, S denotes a scalar leptoquark, and V a vector leptoquark. The subscript shows the weak isospin.[6] We also assume that LQ couple to particles in the first generation only. In this thesis, we adopt this general classification and search for all of them. Possible reactions for each type of LQ are also listed in Table 2.2. The reactions include the LQ coupling to an lepton-quark pair (g_L for the left-handed coupling and g_R for the right-handed coupling). Though there is no theoretical constraint on the value of these couplings in general, the usual reference value for g_L or g_R is the 'electroweak' coupling; i.e. g_L (or g_R) $= \sqrt{4\pi\alpha_{EW}} \sim 0.31$ at $Q = M_{LQ} \sim O(100)GeV$.

The partial width of the resonance for scalar LQ (Γ_S) and vector LQ (Γ_V) with a coupling g are [35]

$$\Gamma_S = \frac{g^2}{16\pi} M_{LQ}$$

and

$$\Gamma_V = \frac{g^2}{24\pi} M_{LQ},$$

respectively. Assuming $M_{LQ} = 200GeV$ and $g = 0.31$ for example, we obtain $\Gamma_S = 380MeV$ and $\Gamma_V = 250MeV$. Thus generally the peak is expected to be very narrow within the detector resolution. On the other hand, the width is sufficiently large so that LQ decay promptly in the detector.

A good estimation of the s-channel production cross section is given assuming that the resonance is described with a δ-function (narrow-width approximation):

$$\sigma(ep \to LQ) = \frac{\pi}{4s} g^2 q(x_{LQ}) \times \begin{cases} 1 & \text{for scalar LQ} \\ 2 & \text{for vector LQ} \end{cases}$$

where $q(x_{LQ})$ is parton density at $x = x_{LQ}$. The cross section is directly proportional to the parton density. LQ with F=2, where F is the fermion number, can couple to valence quarks, and the cross section are kept high up to very high-mass region. But LQ with F=0 couple to anti-quarks only, and the cross section falls down rather steeply in high-mass region.

In addition to the s-channel process, u-channel process and LQ-DIS interference also exist. However, the s-channel contribution is dominant over the mass region of interest.

Possible decay modes of LQ are $LQ \to eq$ or $LQ \to \nu q$. The former mode is identical to NC process in the final state, and the latter to CC process. The branching ratio to the

[6]The notation is based upon reference [36].

mode $LQ \to eq$ (b) depends on g_L and g_R, e.g. for S_0 we obtain

$$b = \frac{g_L^2 + g_R^2}{2g_L^2 + g_R^2}.$$

In addition to the x-distribution, the distribution of the kinematical variable y is also different between LQ and DIS. The variable y is related to the angle between the incoming proton and the decay electron in the LQ rest frame, θ_{cm}, by $y = (1 + \cos\theta_{cm})/2$. The y-dependence of the leptoquark cross section is a direct consequence of the leptoquark spin as shown below:

$$\frac{d\sigma}{dy} \propto \begin{cases} 1 & \text{for scalar LQ} \\ (1-y)^2 & \text{for vector LQ with } g_L = 0 \text{ or } g_R = 0 \\ y^2 + (1-y)^2 & \text{for vector LQ with } g_L = g_R \end{cases}$$

where we assume the unpolarized beam particles. On the other hand the cross section of NC events is approximately proportional to y^{-2}. Thus LQ would produce an anomaly in high-y region.

As a summary, if LQ exist, the cross section is sufficiently large to be detected at HERA. Though the final state of LQ and DIS are identical, the population in the kinematical $x - y$ plane is quite different. Thus some appropriate cuts in the $x - y$ plane can separate LQ events from DIS events efficiently.

2.4.3 Present Experimental Bounds

Here we mention the existing experimental bounds for masses of the 10 types of LQ introduced in the last subsection. First of all, there are studies on the direct production of scalar LQ with e^+e^- collisions and $p\bar{p}$ collisions. At LEP, the dominant process is the decay of Z^0 into a pair of LQ[37]. The mass bounds from OPAL[38], L3[39], ALEPH[40] and DELPHI[41] are similar around 45 GeV at the 95% confidence level (CL). The limit is independent of the LQ coupling to an electron-quark pair. In $p\bar{p}$ collisions, single LQ production is possible but the dominant process is a pair production independent of the LQ coupling g. From UA2 collaboration at CERN-S$p\bar{p}$S collider[42], the limit at 95% CL is 67 GeV assuming that LQ decay into eq and νq at the same rate, and 72 GeV for decaying into eq only. There is no bound yet from TEVATRON, but the preliminary mass limit by CDF is up to 113 GeV [43].

Existence of LQ causes some new signals in low energy experiments. LQ which can couple to both $\nu_L d$ and $e_R u$, or to both $\nu_L \bar{u}$ and $e_R \bar{d}$ mediate the decay $\pi^+ \to e^+\nu_e$ and hence the branching ratio would deviate from the prediction of the Standard Model. From the experimental bound $BR(\pi \to e^+\nu_e) < 1.2\times10^{-4}$, the mass bound is [27]

$$M_{LQ} > 8.8TeV \times \sqrt{g_L g_R}$$

for scalar LQ (S_0 and $S_{1/2}$). The limit for vector LQ (V_0 and $V_{1/2}$) is $M_{LQ} > 125TeV$, assuming $g_L = g_R = g_{SU(2)}$.[44]

Assuming $g_R = 0$ or $g_L = 0$, the tightest bound is from the weak universality by comparison of nuclear β-decays, which can be caused with LQ (S_0, S_1, V_0 and V_1), and μ-decays which are purely leptonic. The result is [45]

$$M_{LQ} > 1.7TeV \times g_L.$$

As the summary, Table2.3 is a list of the present experimental bounds for the 10 types of LQ. It is expected clearly that HERA allows us to examine a completely new search region. The mass limits in parentheses are from indirect searches. As one can see, some types of LQ have quite stringent mass limits. Even for them, however, a search for the direct production of these LQ at HERA would be an additional confirmation and is also worth trying.

Chapter 3

Experimental Apparatus

3.1 HERA

HERA (Hadron Electron Ring Anlage) is the first electron-proton collider in the world, located at DESY (Deutsches Electronen Synchrotron) in Hamburg, Germany. Under the nominal condition of HERA, head-on collisions of protons with the energy of 820 GeV and electrons of 30GeV take place every 96ns, with the luminosity of $1.5 \cdot 10^{31} cm^{-2} s^{-1}$. The total energy in the center-of-mass frame, $\sqrt{s}$, is 314GeV which corresponds to an electron beam energy of 51TeV for a fixed-target experiment. Fig. 3.1 is a schematic overview of HERA. It comprises two rings, a proton ring equipped with superconducting magnets and an electron ring with normal magnets. These 2 rings cross in 4 interaction regions; the south hall for the ZEUS detector, the north hall for the H1 detector, the east hall for future experiments and the west hall used mainly to install large apparatus.

Fig. 3.2 is a closer look at the injection apparatus. The proton injection procedure starts from accelerating H^- ions up to 50 MeV in the H^- LINAC. After electrons being stripped from H^- ions, protons are then injected into the new proton synchrotron DESYIII and are accelerated up to 7.5 GeV. After that they are injected into PETRA, accelerated to 40GeV and finally injected into HERA. Electrons are pre-accelerated in LINACI up to 220 MeV, then in the DESYII storage ring to 7.5GeV, in the PETRA to 14 GeV and injected into HERA. The main parameters of HERA under the nominal condition are listed in Table 3.1.

The operation condition of HERA in 1992 was not quite the same as the nominal condition. The proton beam energy was 820 GeV, the same as the nominal value, while the electron beam energy was 26.7 GeV. The CMS energy $\sqrt{s}$ was 296 GeV. Fig. 3.3 shows the bunch structure of HERA in 1992. Only 10 bunches out of 220 bunch buckets were filled for physics runs. Both electrons and protons were filled on bunch crossing numbers (BCN) from 0 to 8. Thus electron-proton collisions took place in 9 buckets. Hereafter

they are called 'collision bunches'. Only protons were filled on BCN=9 and it is called 'the proton pilot bunch'. Similarly only electrons were filled on BCN=19 and it is called 'the electron pilot bunch'. These pilot bunches are used to estimate beam-gas interaction backgrounds. The proton beam current was $1 \sim 2$ mA with a typical lifetime of about 50 hours and with a bunch length of 12-50 cm. The electron beam current was $1 \sim 2$ mA with a typical lifetime of about 15 hours and with a negligible bunch length compared with protons. The typical luminosity was several of $10^{28} cm^{-2} s^{-1}$. Fig. 3.4 shows the typical time distribution of proton and electron bunches. We can see that the electron bunch has a small secondary peak at around 8 ns before the primary peak. The effect of this 'satellite bunch' is taken into account in event selection as well as in the luminosity measurement.

3.2 Overview of the ZEUS Detector

The ZEUS detector is a multipurpose detector at HERA. Fig. 3.5 is the layout of the ZEUS detector, where the proton beam comes from upper-right side of the BEAMPIPE. Fig. 3.6 is a cross section of the ZEUS detector in the azimuthal plane. The main components are (from inside to outside) a vertex detector (VXD), a central tracking detector (CTD), a rear tracking detector (RTD), a forward tracking detector (FTD) with a transition radiation detector (TRD) interleaved, a thin magnetic solenoid (SOLENOID) giving a high magnetic field to these tracking devices, uranium scintillator calorimeters for forward (FCAL), barrel (BCAL) and rear (RCAL) regions, a hadron electron separator (HES) inserted in RCAL, a backing calorimeter (BAC), barrel and rear muon detector (BMUON and RMUON), and a forward muon spectrometer (FMUON). Due to the asymmetric nature of the two beams, the detector also has asymmetric structure to ensure the uniform response for entire $x - Q^2$ region.

There are also some detectors located upstream of the main detector with respect to the proton beam. For shielding purpose against secondary particles from the proton beam halo, a big iron wall (VETOWALL) is placed upstream with regard to the proton beam. A small scintillation counter (called the C5 veto counter) is also equipped around the beampipe between VETOWALL and RCAL to reject background events. The luminosity monitoring system (LUMI) is located far upstream of the proton beam.

In the analysis in this thesis, we used CAL, CTD, LUMI and C5 veto counter. Some details of these detectors are described in the following sections.

3.3 Uranium Scintillator Calorimeter (CAL)

3.3.1 Mechanical Design

The Uranium Scintillator Calorimeter (CAL) is the most important component of ZEUS for both the trigger and the offline analysis. Among various requirements for CAL, the most significant one is to achieve very good energy resolution for energetic hadrons and jets. For this purpose, the sampling-type calorimeter made of depleted uranium (DU) plates interleaved with plastic scintillator tiles is chosen. This choice realizes the equal response to electromagnetic-interacting particles and hadronic-interacting particles [46] (e/h = 1, where e is the average signal of CAL for electrons and h is the average signal for hadrons with the same incident energy). Thus the energy resolution for hadrons is insensitive to the fraction of π^0 produced in the hadronic shower. In addition, plastic scintillators give very good time resolution which is crucial for ZEUS to distinguish beam-collision events from background events. They are also radiation-hard enough to survive for 10 years with 20 rad/day near the beampipe region [47].

Fig. 3.7 is the layout of CAL. [48]. It comprises the following three parts:

- Forward Calorimeter (FCAL) ($2.2° < \theta < 39.9°$),
- Barrel Calorimeter (BCAL) ($36.7° < \theta < 129.1°$),
- Rear Calorimeter (RCAL) ($128.1° < \theta < 176.5°$).

The entire CAL covers 99.8% of the forward hemisphere and 99.5% of the rear hemisphere. FCAL and BCAL are segmented longitudinally into three parts, an electromagnetic section (EMC) with a depth of 25 radiation lengths (X_0) or 1 interaction length (λ) and two hadronic sections (HAC1,2) with a total depth of $2 \times 3.1\lambda$ in FCAL and $2 \times 2.1\lambda$ in BCAL. RCAL is divided longitudinally into two sections, an EMC (1λ) and a HAC (3.1λ) section. The total depth in each calorimeter is determined to contain at least 95% of the energy for 90% of the maximum energy showers at any polar angle [48]. Detailed sizes and structure of EMC and HAC towers are given in Table 3.3. FCAL extends from Z = 221 cm to Z = 451 cm. FCAL consists of 24 modules with the size of 20cm horizontally and from 2.2m to 4.6m vertically. Fig. 3.8 shows a FCAL module. Each module consists of supertowers stacked vertically. Fig. 3.9 shows a schematic overview of a supertower. Each supertower contains one HAC1, one HAC2 and 4 EMC towers. HAC1 and HAC2 towers have the transverse dimension of $20 \times 20cm^2$. An EMC tower has $5 \times 20cm^2$. RCAL extends from Z = -146 cm to Z = -307 cm and basically has the same structure as FCAL, except that each supertower contains 2 EMC towers, i.e. the transverse size of each EMC is $10 \times 20cm^2$. The sampling ratio of DU and scintillator plates is unique in the whole

calorimeter; 3.3mm thick DU plates ($\simeq 1X_0$) and 2.6mm thick plastic scintillator plates [1]

Fig. 3.10 is a cross section of BCAL in the azimuthal plane. The inner and outer radii of BCAL are 1.22m and 2.29m. BCAL consists of 32 identical wedge-shaped modules which are tilted by 2.5° clockwise in the azimuthal plane. This tilt prevents particles from escaping the detector, penetrating a gap between modules.

Fig. 3.11 shows one BCAL module. Each module has a length of 3.3m with 14 supertowers. Each supertower has one HAC1, one HAC2 and 4 EMC towers (except the supertower next to FCAL with only 2 EMC towers and the one next to RCAL with 3 EMC towers). Each EMC tower is projective to the interaction point and has a size of $49 \times 233mm^2$ at the front face. HAC1 and HAC 2 towers are nonprojective with the front face size of $244 \times 271mm^2$.

Each tower in a supertower is read out by 2 photomultipliers (PMT's) from both sides of the tower. By requiring a coincidence of the 2 PMT's, we can distinguish a true signal from PMT noise. The energy imbalance between the 2 PMT's is also used to reconstruct the horizontal position of electrons and hadrons. The type of PMT's is XP1911 (Phillips Co. LTD., Netherlands) for FCAL EMC towers and R580-12 (Hamamatsu Photonics K.K., Japan) for all the other towers. Approximately 12000 PMT's are used in the entire calorimeter.

Fig. 3.12 shows the path of scintillation photons. Particles hit a DU plate and produces a shower. Charged particles in the shower enter the scintillation plate next to the DU plate and scintillation photons are produced. These photons travel to each end of the scintillation plate, and are guided to a PMT by a plastic wavelength shifter plate (WLS, 2mm thick). The WLS absorbs scintillation photons and emits photons with longer wavelength suitable for the quantum efficiency spectrum of the PMT photocathode.[2]

It was found during the beam test that CAL gave higher outputs than usual when the beams were injected to a boundary of modules. This was due to the Čerenkov light produced by penetrating electrons through the two adjacent WLS plates. To avoid this effect, a 2.6mm thick lead sheet is inserted between the modules, so that shower develops there. Also UV absorber is doped in the WLS plate in order to absorb short-wavelength Čerenkov light.

3.3.2 Readout Electronics

The readout system has to process data without a significant deadtime. The system also has to have a wide dynamic range. The required dynamic range for FCAL EMC is 40000:1, the most stringent since the energy deposit can be up to 400GeV while radioactivity from

[1] The plastic scintillator plates are made of SCSN-38 (Kurarey Co., Ltd., Japan).

[2] The material of the WLS was chosen to be Y7 (Kurarey Co. LTD., Japan), together with an additional absorbent to cut off UV light below 360 nm [49].

DU plates gives about 10MeV. Thus the system was equipped with 2 different shaping amplifiers with a low and high gain to cover the whole required energy range. In addition, the intrinsic noise of the electronics should be below 1% of the DU noise, so that the DU noise can be used for gain monitoring. There is also a requirement on the radiation hardness. Since some electronics should be implemented on the detector, these should be tolerable against the radiation level of about 1 krad/year [50].

Fig. 3.13 is an overview of the calorimeter readout scheme. [50]. It consists of analog cards, digital cards and readout control system. Analog cards are used for integration, shaping, sampling and buffering of PMT signals. First of all, each PMT signal is split into the high and low gain shapers. The covered energy ranges of the high and low gains differ among the different part of CAL. Following are the covered energy ranges:

	range of high gain (GeV)	range of low gain (GeV),
FCAL	0 - 18	0 - 400,
BCAL	0 - 14	0 - 314,
RCAL	0 - 12	0 - 60.

The shaper is designed to change a δ-function impulse to a triangle-like shape. Both the rising time and falling time are longer than the sampling time. Fig. 3.14 illustrates the shaped pulse. It is sampled every 96 ns, as marked with h_0 to h_7. This scheme makes it possible to suppress high and low frequency noise while keeping required energy and time resolution. The shaped signals are then put into analog pipelines. The pipeline is a custom-made IC based on the switched capacitors [51]. Each pipeline has 58 cells in length, corresponding to 5.6μsec which is required for the global first level trigger decision as will be explained in the next chapter. When the event is triggered, up to eight samples (h_0 to h_7) are stored into the buffer-multiplexers. The pipelines then are resumed to data taking again, while the samples in the buffers are multiplexed and sent to ADC's on the digital cards every 1.7μsec.

With the samples from analog cards, digital cards are used for digitization, selection of high gain or low gain, corrections for gains and pedestals, calculation of energy, time, and energy imbalance, and preparation of 2nd level trigger data. First of all, multiplexed samples from analog cards are digitized with ADC's (Datel ADS-112). The converting rate is 1MHz. The digitized data are stored in the input dual-port memories (DPM's), each of which can hold 16 events. The size of the whole raw data is too large to be sent with a few Hz to the final storage. To reduce the data size, the raw-data are read by Digital Signal Processors (Motolora DSP56001, a 24-bit DSP with 100ns instruction cycle). DSP's read instructions in FIFO's, and read the appropriate data from the input DPM's. Then DSP's select either low-gain or high-gain data, execute the gain and pedestal corrections, and finally calculate energy and time. All the required constants for the calculation are generated in special calibration runs and are downloaded onto the 32 K RAM. The obtained energy and time are stored in the output dual-port memories which are directly

accessible via VME buses. The size of input and output DPM's (16events) is large enough to cope with the nominal 1st level trigger rate of 1kHz. [3]

The energy (E) and time (T_{sample}) are calculated with the following equations in D-SP [52]:

$$E = E_0(1 + \sum_{n=1}^{4} a_n T_0^n)$$

and

$$T_{sample} = \sum_{n=1}^{3} b_n T_0^n.$$

E_0 and T_0 are described as follows:

$$E_0 = \frac{q_c H_0}{e_c} \quad \text{and} \quad T_0 = \frac{h_2 - h_3}{H_0},$$

where q_c is the conversion factor from raw data to charge, e_c the conversion factor from charge to energy, and

$$H_0 = (h_2 - h_0) + 1.8(h_3 - h_0).$$

q_c is determined for each shaper, but e_c is a global constant (7.3pC/GeV in FCAL and 10.6pC/GeV in BCAL and RCAL). a_n and b_n are coefficients to apply the polynomial correction to E_0 and T_0 in case of $h_2 \neq h_3$.

3.3.3 Calibration system

To keep the good energy and time resolution throughout the experiment, the following calibration tools were used.

- Uranium noise monitor

  One of the unique features of the ZEUS calorimeter is that the calorimeter itself is a radioactive source due to the decay of ^{238}U. Since its constant radioactivity is about a rate of 1 decay/ns in the EMC cells and more in HAC cells, the uranium noise (UNO) current integrated over 20ms can be monitored within 1% level. The UNO current, which is proportional to the gain for an optical chain of scintillators, WLS's and PMT's, is therefore a good calibration source for the optical readout. The nominal UNO currents for FCAL EMC, RCAL EMC and HAC towers are 100nA, 200nA and 400-500nA, respectively. The readout path of the UNO currents is shown in Fig. 3.13. A PMT signal is divided into the UNO integrator in an analog card. This path was used in the special calibration runs every 8 hours. [4]

[3] It takes about 8ms for the 2nd level trigger to make a decision. Therefore a half of the buffer is filled during the decision in average.

[4] The typical variation of PMT gains of the prototype modules was found to be 1% with 8 hour intervals.

Both the beam tests and calibrations during the luminosity runs showed that UNO current was successfully used to monitor the PMT gains within 1%. At the beam tests, intercalibration of cells was performed with the comparison of the expected gain by UNO and the response to the beam. They agreed within 1.5% for RCAL EMC and 1.1% for others [53].

- Charge injection system

  It is also necessary to calibrate the analog readout chain after PMT's to ADC's. The charge injection system has been implemented to emulate PMT signals. The schematic drawing of the charge injection system is shown in Fig. 3.15. The system can provide charge corresponding to 0 to 10GeV/PMT with a precision of 0.2% level. Since the signal can be put in with desired timing relative to the sampling clock, the system was also used for time calibration.

- Light flasher system

  The light flasher system is the main tool for time calibration. As shown schematically in Fig. 3.15, a dye laser pumped by N_2 laser is the source of light beam. The light beam is attenuated with filters and then is guided by fibers into PMT's. The light beam is split by a mirror and 0.1% of the total signal is monitored with a photo-diode system.

  The light flasher system is also used for monitoring of PMT performance and for the linearity measurement up to the very high energy region which can not be reached with the available test beam nor charge injection.

In addition to these main calibration tools, some other facilities have been also used. As an alternative to the charge injection, programmable DC voltage (calibrated to 0.1%) can be provided to calibrate electronics. LED light injection is possible as an alternative light source. During the production period, $^{60}C_o$ source was used to scan the structure of the calorimeter modules.

3.3.4 Status and Performance in 1992

CAL has been fully operational since the beginning of the luminosity runs in 1992. The fraction of bad cells not used was less than 0.1%. Its performance was checked not only with beam and cosmic-ray tests in the construction period [53][54], but with luminosity data themselves and with special calibration runs [47]. The beam tests were carried out both with some of the final modules as well as with prototype modules following the same mechanical design as the final modules. Below we summarize the results.

- e/h ratio

It was confirmed in the beam test with the prototype modules that e/h ratio was close to unity for the momentum range from 2GeV/c to 100GeV/c. Below 2GeV/c, hadrons tended to behave as minimum ionizing particles and e/h ratio went down to 0.62.

- Energy resolution

  Thanks to the equal response to electrons and hadrons, the rms energy resolution of the prototype module is

$$\frac{\sigma_E}{E} = \frac{18\%}{\sqrt{E}} \oplus 2\% \quad \text{for electrons}$$

  and

$$\frac{\sigma_E}{E} = \frac{35\%}{\sqrt{E}} \oplus 2\% \quad \text{for hadrons,}$$

  where E is the energy of electrons or hadrons in GeV. Assuming that the DU noise is dominant, the noise contribution to the energy resolution (σ_n) is estimated to be 25 MeV/tower.

  The rms energy resolutions of FCAL and BCAL for electrons obtained from the beam test were consistent with the above formula. The energy deposits in FCAL and RCAL by penetrating beam halo muons during the luminosity runs agreed with those by test beam muons and by cosmic rays within 5%. Intercalibration between FCAL and RCAL with beam halo muons also showed agreement within 1%.

- Time resolution

  The intrinsic time resolution for each calorimeter cell was measured to be around 0.3 ns with the light flasher system, provided the energy in each cell is above a few GeV. This value gives a lower limit of the time resolution. An additional systematic uncertainty comes from the time offset (T_{offset}) for each PMT. T_{offset} is adjusted so that the measured time of a PMT at any location becomes 0 in average when an interaction occurs at the nominal vertex (X,Y,Z) = (0,0,0). Once T_{offset} is determined, we obtain time as ($T_{sample} - T_{offset}$). Both the light flasher system and the charge injection system were fully utilized to determine T_{offset}, which was decomposed to offsets from time of flight between the nominal vertex and each calorimeter cell, shower development time, WLS's transit time, PMT's transit time, electronics transit time and cable lengths [52].

  With taking the uncertainty of T_{offset} into account, the global time resolution was calculated for DIS candidate events. The results for FCAL, RCAL and BCAL are 1.5, 0.5 and 2 ns, respectively. The uncertainty of the actual vertex point due to the broad Z-distribution of the proton bunches is included in these values. By removing

this factor using the vertex information by CTD, the resolution for FCAL becomes 0.9ns. The time resolution for each PMT is 2ns for FCAL, 0.8ns for RCAL EMC and 1.3ns for RCAL HAC, provided the deposited energy is above 1GeV for each PMT.

- Position resolution

  The position resolution was studied for isolated electrons and hadrons in the beam test of the prototype modules. The coordinates X and Y were determined as the center of gravity of the deposited energy with the following equation:

$$X = \sum_i w_i (X^0{}_i + \frac{\lambda}{2} \ln \frac{E_{Ri}}{E_{Li}})$$

  and

$$Y = \sum_i w_i Y^0{}_i,$$

  where (X^0, Y^0) and (E_{Li}, E_{Ri}) are the central position and energies in both PMT's of each calorimeter cell (i). The factor $w_i = (E_{Li} + E_{Ri})/E$ is the energy weight and λ the attenuation length of the scintillator (= 54cm).

  The obtained position resolutions were as follows:

$$\sigma_X = \frac{5.4}{\sqrt{E}}\ cm, \quad \sigma_Y = (\frac{1.4}{\sqrt{E}} \oplus 0.7)\ cm \quad \text{for electrons}$$

  and

$$\sigma_X = \frac{6.5}{\sqrt{E}}\ cm, \quad \sigma_Y = (\frac{6.7}{\sqrt{E}} \oplus 0.7)\ cm \quad \text{for hadrons}$$

  where E is the energy of electrons or hadrons in GeV.

- Linearity

  With the tests using an electron beam, the linearity is guaranteed within 1% for FCAL EMC from 15 to 110 GeV. The deviation is up to 2% for 110 GeV electrons in FCAL HAC and RCAL towers.

- Non-uniformity

  It was confirmed by the beam test that the non-uniformity at module and tower boundaries is negligible for hadron showers. As mentioned before, a 2.6mm thick lead sheet has been inserted between the modules in order to achieve the best uniformity for EM showers. The position scan with the 15GeV/c electron beam perpendicular to the FCAL and RCAL shows that non-uniformity is about 4% for FCAL and 6% for RCAL. At luminosity runs, electrons coming from the interaction point always enter the calorimeter with some angles. Therefore the non-uniformity at the module and tower boundaries is smeared.

3.4 Central Tracking Detector (CTD)

3.4.1 Design

The central tracking detector (CTD) is a cylindrical drift chamber with the active radius of 19.0 - 78.5 cm and active length of 202.4 cm, corresponding to the polar angle range $15° < \theta < 164°$. Fig. 3.16 (a) shows a layout of the octant of CTD. There are 9 superlayers (SL1 - SL9). Each superlayer consists of cells ($8 \cdot (3+N)$ cells in the superlayer N). Each cell has 8 sense wires together with ground wires, field wires and shaper wires. Superlayers with odd numbers have wires parallel to the beam direction, while four alternate superlayers have wires with stereo angles of about $\pm 5°$. [5] Fig. 3.16 (b) shows electron drift trajectories. The 45° tilt of the drift cell makes it possible to detect a hit on at least one sense wire within 96ns before the next beam crossing occurs. This is particularly important to make trigger signals. The whole CTD is surrounded by a superconducting solenoid which generates a magnetic field of 1.8 Tesla nominally. Expected performance with a full readout system is summarized in Table 3.4 [55][56].

It is also possible to measure the longitudinal coordinate (Z) by the time difference between the two ends of the sense wires in SL1, SL3 and SL5. In total 704 sense wires can be read out in this way. Fig. 3.17 is a block diagram of the electronics for the time difference measurement. The induced pulse in a sense wire is preamplified, transmitted with a coaxial cable (45 m long), amplified again by a differential postamplifier, and finally a digital timing pulse is issued by a constant fraction discriminator into a time to amplitude converter (TAC). A start pulse for the TAC comes from the forward end of CTD, and a stop pulse from the rear end. The signal from the rear end is also used as a strobe signal for the FADC which digitizes the TAC output. Then the result is put in a pipeline, as similar to CAL.

3.4.2 Status and Performance in 1992

In 1992, CTD was operational in a magnetic field of 1.43T [57]. The full FADC readout system was not operational. Therefore only SL1, SL3, and SL5 were active with Z measured by timing as explained above. The gas was a mixture of Argon, CO_2, ethane and ethanol in the proportions 88.22 %, 9.22 %, 1.69 % and 0.88 %. The strength of the drift field was 1.2kV/cm. In these conditions the Lorentz angle was calculated to be 39.1° and the nominal drift velocity (v_0) was 48.7 μm/ns.[6]

Measured time of each wire (t) was converted to drift distance (d) with the following

[5] The values are chosen so that the angular resolution for polar and azimuthal angles are roughly equal.

[6] The condition in summer 1992 was slightly different.

equation:

$$d = (v_0 + \delta v_0)(t - t_0) + \frac{P_3}{(t - t_0)^2} + P_4(t - t_0)^6,$$

where δv_0 is a correction to v_0, t_0 the time offset, P_3 the correction coefficient for small times ($t \sim t_0$), and P_4 the correction coefficient for large times. These 4 parameters were determined on a run-by-run basis. With this procedure the Z resolution was obtained to be ~ 4.0 cm and the $r\phi$ resolution was ~ 0.9 mm [57][58].

3.5 Luminosity Monitoring System (LUMI)

3.5.1 Design

The best method to measure the luminosity at HERA is to tag bremsstrahlung events [55],

$$e + p \rightarrow e + p + \gamma,$$

because of its reliable cross section, a high rate and easy detection. Since most electrons and photons in the final state have very small scattering angle, the signal of the bremsstrahlung event is an electron and a photon in coincidence down to the beampipe with a condition $E_e' + E_\gamma = 26.7GeV$, where E_e' and E_γ are the energy of the scattered electron and the radiated photon. Fig. 3.18 is an overview of the ZEUS luminosity monitoring system (LUMI). It consists of the photon detector (GDET) and the electron detector (EDET). Table 3.5 shows sizes and the structure of GDET and EDET. A bremsstrahlung photon with the angle of $\theta_\gamma < 0.5$ mrad comes out of the beampipe at the end of the straight section, where the beampipe is bent vertically, through the copper-beryllium window into a lead-scintillator sandwich calorimeter. Finger counters (made of scintillator) are inside the calorimeter to monitor the position of photons with an accuracy of $\sim 2mm$. To reject synchrotron radiation, a filter made of carbon is placed in front of GDET. A Čerenkov counter is also equipped between the filter and GDET in order to reject secondary electrons generated in the filter.

EDET can accept scattered electrons with an angle of $\theta_e < 6$ mrad and an energy of $0.2E_e < E_e' < 0.9E_e$, where E_e' and E_e are the energy of the scattered electron and the beam electron (= 26.7 GeV). Since E_e' is less than the electron beam energy, the scattered electron is bent with a larger curvature than beam electrons and thus takes off the beampipe from a steel window. Then the electron goes into a lead-scintillator sandwich calorimeter through a collimator.

Both calorimeters were tested and calibrated with electron beams at DESY and at CERN. The obtained energy resolution is $(18 \pm 2)\%/\sqrt{E}$ [59], where E is the measured energy in GeV.

3.5.2 Luminosity measurement

The luminosity L is defined by the following formula:

$$R = L \cdot \sigma \cdot \varepsilon,$$

where R is the rate of the bremsstrahlung events, σ the theoretical cross section and ε the overall detection probability. To obtain R from the observed event rate, it is necessary to subtract the background events coming from the bremsstrahlung of the beam electrons scattered by the residual gas ($e + gas \rightarrow e + gas + \gamma$). Since the bremsstrahlung events on the electron pilot bunch contains this process only, R is obtained with the following equation:

$$R = R_{tot} - R_{pilot} \cdot \frac{I^e_{tot}}{I^e_{pilot}},$$

where R_{tot} is the total rate of bremsstrahlung events on the collision bunches, R_{pilot} the rate on the electron pilot bunch, I^e_{tot} the total electron beam current and I^e_{pilot} the electron beam current on the electron pilot bunch. The overall detection efficiency ε depends on the detection method. We used 2 different methods to tag the bremsstrahlung events [60][61].

For most of the data ($\sim$94% of the total integrated luminosity), we required the condition 'energy in GDET > 5 GeV' to tag bremsstrahlung events. The overall systematic error of the integrated luminosity is 5% [61]. At the very early stage of the data taking (for $\sim$6% of the total integrated luminosity), we required the coincident hit of EDET and GDET. The energy window for EDET is $9.6 - 17.6$ GeV, which realizes a large acceptance ($\geq 70\%$) for electrons. The corresponding energy window for GDET is $9 - 17$ GeV. The systematic error of the integrated luminosity by this method is 14%.

Fig. 3.19 shows the integrated luminosity in 1992. 32.6 nb^{-1} was taken in total. Among them, the integrated luminosity of the good ep runs we use in this analysis is 26.6 ± 1.6 nb^{-1}. The overall systematic error of the luminosity is 6%.

3.6 Interaction region and C5 veto counter

A set of absorbers (called A1 and A2) and movable collimators (called C1 to C5 made of Tungsten) are equipped to shield the ZEUS detector against synchrotron radiation. Table 3.6 summarizes the position of the collimators and absorbers. A scintillation counter (to veto beam-gas events) and a beamline calorimeter are also equipped with the C5 collimator. Fig. 3.20 is a sketch of the C5 collimator and counters [62]. The C5 veto counter consists of two layers of plastic scintillator (made of SCSN38) interleaved with lead plates. Each layer is further divided into an upper and a lower section, hence totally four signals are read out by four PMT's (R580). The entire counter has a horseshoe-shape in x-y plane.

Output signals of the C5 veto counter are used in the trigger system in order to reject a part of proton-gas interactions which can not be vetoed by VETOWALL nor RCAL. Fig. 3.21 shows the way of making the C5 veto signals. As shown in Fig. 3.21, a coincidence of two upper counters and a coincidence of two lower counters are put into TDC's. The time resolution of each signal is about 5ns with newly developed TDC's which can process signals every 96 ns [63]. The typical timing distribution on a collision bunch is shown in Fig. 3.22. The pieces of timing information are used in the trigger system with the following rejection logic:

```
If any of 4 TDC's has a hit with 'proton timing'
      and
  none of 4 TDC's has a hit with 'collision timing',
Then
  Reject the event.
```

The performance of the C5 veto counter is mentioned in Section 4.3.

The Beamline Calorimeter (BEAMLINE) is a sandwich of silicon and tungsten, and is located at the opposite side of the C5 veto counter. It was operational in 1992 for online monitoring of the beam condition and radiation.

3.7 Other Detectors

There were also many other detector components fully or partially operational in 1992. These are, however, not used in the analysis in this thesis. The following is a brief description of these detectors [55].

Rear Hadron Electron Separator

The Rear Hadron Electron Separator (RHES) consists of a silicon pads inserted into RCAL at a depth of 3 radiation lengths. The aim of RHES is to give additional information in order to separate electrons from hadrons by detecting electromagnetic clusters with the better position resolution. The size of each silicon pad is $3 \times 3cm^2$. RHES was partially operational in 1992. Electromagnetic clusters in RHES and CAL showed good agreements.

Vertex Detector

The Vertex Detector (VXD) is a time-expansion jet chamber located inside CTD. The expected position resolution is 50μm, which makes it possible to resolve the secondary vertices of short lived particles.

Backing Calorimeter

CAL is enclosed by the Backing Calorimeter (BAC), which measures the energy leakage of hadronic showers as well as tags cosmic-rays and energetic muons from the interaction point. BAC consists of aluminium proportional tubes filled with Ar/CO_2 inserted in the return yoke, which acts as an absorber. The expected energy resolution is $100\%/\sqrt{E}$ (E in GeV).

Forward Muon Detector

The Forward Muon Detector (FMUON) covers the forward direction outside FCAL up to $\theta = 45°$, where considerable fraction of muons in heavy flavor production or in exotic processes is to be found. FMUON consists of toroidally magnetized iron slabs interleaved with drift chambers, limited streamer tubes and time-of-flight counters. The expected momentum resolution is about 25% for muons up to 100GeV/c.

Barrel and Rear Muon Detector

The main purpose of the Barrel and Rear Muon Detector (BRMUON) is to tag energetic muons penetrating CAL and the return yoke from the interaction point, and to reject non-pointing muons such as cosmic-rays. Limited streamer tubes both inside and outside the return yoke are used. The expected momentum resolution is 20% for muons of 20GeV/c.

Vetowall Detector

The Vetowall Detector (VETOWALL) is located about 7.5m from the interaction point behind RCAL to shield the main detector from the halo particles, as well as to send the veto signals to reject background events. VETOWALL consists of an iron wall of the dimensions 800cm(width)×760cm(height)×87cm(thickness) with a rectangular hole of 95cm×95cm in the middle, and scintillator hodoscopes on both sides of the iron wall.

There are also some other detector components in preparation and will operate in 1993 or later. These are the forward tracking detector (FTD) with the transition radiation detector (TRD), the rear tracking detector (RTD), the small angle rear tracker (SRTD), the leading proton spectrometer (LPS) and the forward hadron electron separator (FHES).

Chapter 4

Data Acquisition and Trigger

4.1 Overview of the ZEUS data acquisition system

4.1.1 Requirements

The goal of the ZEUS data acquisition system (ZEUS-DAQ) is to take physics events with high efficiency especially for high-Q^2 DIS events, while rejecting background events effectively enough to achieve a reasonable data taking rate. Table 4.1 shows the expected event rate of various physics processes [64] under the nominal HERA condition. The total rate of the processes is beyond our design value of the data taking rate ($\sim 5\ Hz$) which reflects the possible data transfer rate to the storage medium. Thus we have to apply the online selection of physics processes.

The dominant background at HERA is the proton-gas event; i.e. the interaction of a beam proton and residual gas in the beampipe. The total event rate of the proton-gas interaction per unit length per time is given by:

$$\frac{d^2N}{dl\ dt} = I_p \sum_i \rho_i \sigma_i = \frac{I_p}{kT} \sum_i p_i \sigma_i,$$

where I_p is the proton beam intensity ($= 10^{18} sec^{-1}$ at the nominal condition), k the Boltzmann constant, T the room temperature ($= 293$ K), ρ_i the partial density of a molecule in the residual gas, p_i the partial pressure and σ_i the cross-section for the ith material. Assuming that the residual gas consists of 90 % H_2 and 10 % heavier molecules (H_2O, CO, CO_2), the expected rate is [64][65][66]

$$\frac{d^2N}{dl\ dt} = 0.49[kHz \cdot m^{-1}] \times \frac{p}{[10^{-9} torr]}.$$

The straight section of the beampipe extends from -110 m to +2 m. With an assumption of an overall pressure of $3 \times 10^{-9} torr$, the total rate would be $\sim 100 kHz$. Another big

source is the interaction between off-momentum protons and materials in or around the beampipe (the beam scraping event). This has been studied intensively [65], and it turned out that the event rate seen in the ZEUS detector could be comparable to the proton-gas events. Cosmic-rays are with $\sim$ 1kHz.

4.1.2 DAQ system

Fig. 4.1 is a schematic of ZEUS-DAQ. As shown in the figure, the trigger system consists of 3 levels of triggers; the first level trigger (FLT), the second level trigger (SLT) and the third level trigger (TLT).[1] Only FLT is the hardware trigger to make a quick decision, while SLT and TLT are software trigger systems. Another component called the event builder (EVB) is located between SLT and TLT to merge data from all the components.

The goal of the FLT system is to reduce the event rate down to 1 kHz. Since the initial background rate is $\sim$100kHz, the rejection factor of $\sim$100 is required. FLT consists of local FLT's and the global first level trigger (GFLT). Each detector component has a local FLT which quickly makes digital trigger data and sends them to GFLT. Using the local FLT data, GFLT makes a first-level decision to accept the event. In total, $\sim$ 800 bits of local FLT data are sent to GFLT. When GFLT decides to take the data, a GFLT-ACCEPT signal is issued 46 clocks (4.4μs) after the bunch crossing. FLT is a pipeline system. Each event is processed step by step in the pipelines synchronized with a 96ns clock (HERA clock). At every clock, events on different bunch crossings are on different processing stages in the pipelines. In this way FLT is able to make a trigger decision for every bunch crossing. During the FLT decision procedure, the readout data are stored in analog or digital pipelines. With the GFLT-ACCEPT signal for a particular crossing, each detector component reads out the corresponding pipeline cells.

Using the readout data, local SLT's make SLT data with the better resolution than the FLT data. The SLT data are sent to the global second level trigger (GSLT). GSLT consists of a network of microprocessors (INMOS transputer) [67]. The goal of GSLT is to reduce the event rate down to 100 Hz, i.e. the rejection factor of 10 is required assuming that GFLT output rate is 1kHz. The allowed computing latency for each local SLT and GSLT are 5ms and 3ms, respectively.

If an event is accepted, GSLT sends an accept signal through EVB to all the detector components. Each detector readout system then sends the full data to EVB. The main task of EVB is to build events and pass the data to TLT. The EVB hardware is also based upon transputers. The EVB design requires input/output throughput of more than 100 Hz to cope with all the data accepted by GSLT.

TLT makes the final decision to record data. The full data from EVB are used to make

[1] Though not available in 1992, there is also a plan to implement the Fast Clear processor [64] to reject a part of events accepted by GFLT before the SLT decision procedure starts.

elaborate selection criteria. The main goal of TLT is to reduce the SLT rate of 100 Hz to $\sim$ 5 Hz. TLT is a processor farm with a parallel input stream. The data station server 4D/35S from Silicon Graphics (SGI) is used as the processor. Totally 30 processors, which realize $\sim$ 1000 MIPS of computing power [68], are used to execute the data selection.

4.2 First level trigger system

4.2.1 Local FLT

Table 4.2 shows the full list of the local FLT data. Each set of data is transmitted to GFLT with a 16 bits cable. In total data for 56 cables are listed in Table 4.2, but not all of them were prepared in 1992. Available data in 1992 are tagged with '*' in Table 4.2. Especially the CAL-FLT data, which played the central role in the GFLT decision, were different from the full version since the different hardware was used [69]. Among the data tagged with '*' in Table 4.2, those actually used to make the GFLT-ACCEPT signals are tagged with 'o'.[2]

The CAL-FLT system in 1992 is based upon an energy deposit in a trigger tower which covers the area of $20 \times 40cm^2$ (sum of adjacent 2 supertowers). Trigger towers are chosen so that each tower covers a specific polar and azimuthal angle, and that nearly 4π sphere is covered in total. A trigger signal for each trigger tower is issued if the energy deposit in the trigger tower exceeds a threshold value. The threshold value can be set independently for each trigger tower, but we used the following setting: FCAL is divided into 3 subregions (the beampipe subregion, the inner subregion and the outer subregion) as shown in Fig. 4.6. The threshold value is unique in each subregion. Since EMC and HAC are treated separately, FCAL has 6 different threshold values in total. RCAL is divided into 2 subregions (the beampipe subregion and the outer subregion) as shown in Fig. 4.6. Each subregion for HAC has a unique threshold value, while 2 different threshold values are used for EMC. Thus there are 6 threshold values for RCAL. In BCAL, one global threshold value is set for each EMC and HAC. As a result, 14 threshold values were prepared in total. For the operation in 1992, some standard threshold sets were used as shown in Table 4.3. Since beampipe towers have much higher activity, they had the highest threshold values.

To send the trigger tower information to GFLT, signals from trigger towers in the same trigger region are ORed. The definition of the trigger region is as follows: Each FCAL and RCAL is divided into 4 trigger regions by the azimuthal angle. BCAL is divided into 8 regions with 4 azimuthal and 2 polar angle ranges. Thus the whole CAL is divided into 16 trigger regions. Since EMC and HAC are treated separately, each trigger region sends

[2] All the other data were monitored by GFLT for the test purpose.

an EMC-bit and a HAC-bit to GFLT, except RCAL-EMC regions where 2 EMC-bits are sent.

In the final design of CAL-FLT, more data are planned to be prepared. Some global quantities such as total energy, total transverse energy and missing transverse momentum are sent to GFLT. Information on an electron, a muon and a jet is also prepared by finding isolated local clusters.

LUMI-FLT sends energy deposits in EDET and GDET, and also some flags to identify event types. BMU-FLT sends 10 regional hit information.

4.2.2 Global FLT

The main task of GFLT is to make a first level decision using the local FLT data. In addition, GFLT broadcasts the 96ns clock to all the detector components for the totally synchronized operation. Thus all the detector components have to communicate with GFLT, even if it does not send local FLT data at all. Also GFLT distributes scheduling signals for the run-time test and calibration of detectors.

The required tasks mentioned above determine the connections and transmitted signals between GFLT and other components. Fig 4.2 shows the handshaking between GFLT and other components. GFLT and other components are connected with twisted pair flat cables of length $\leq 30m$. These are the fastest communication lines between the central system and local components.

Fig 4.3 is a block diagram of the GFLT hardware. As the hardware, GFLT consists of an equipment computer and the following 4 major blocks [70]:

- **Trigger Logic Block**
  All the local FLT data for trigger calculation are put into the trigger logic block. The trigger logic block processes these data, i.e. set thresholds for energy values, make correlations between different detectors, check some flags for a certain event-type and so forth. The results are put out as 64 yes/no bits. As the hardware, each of these 64 bits is called a trigger slot. To each trigger slot, a simple logic called 'subtrigger' is assigned. The results on the 64 trigger slots are sent to the final decision modules (FDM's) which are described next.

- **Final Decision Modules (FDM's)**
  The main task of the FDM's is to make the GFLT-ACCEPT signal as an OR of all the 64 subtriggers. Fig.4.4 shows the block diagram of a FDM. Before making the GFLT-ACCEPT signal, each subtrigger can be prescaled in the FDM's if necessary; e.g. if the subtrigger is prescaled with a prescale factor 1/4, only one fourth of the events accepted with this subtrigger participates in making the GFLT-ACCEPT flag. In addition to the prescaling, each trigger slot can be inhibited by an OR of

any combination of 8 VETO-slots. The data for these VETO-slots are also made of the local FLT data in the trigger logic block. As the summary, the schematic logic of the entire system with the trigger logic block and FDM's is shown in Fig. 4.5.

- **Timing controllers (TC's)**
  The timing controllers (TC's) control the communication between GFLT and other components.

- **Clock distributor**
  The clock distributor receives the HERA clock and generates the 96ns clock which is globally used in the ZEUS experiment.

Since the GFLT-ACCEPT signal is made as an OR of subtriggers, various types of events are contained in the recorded data. For offline analysis, one can strip events of interest by checking that a corresponding subtrigger bit is on. In this way, the entire GFLT logic is kept general to save various types of physics events, while we can analyze specific event types offline considering only a simple trigger logic.

4.2.3 Design of trigger logic block

GFLT should be a flexible and fast hardware trigger. For this purpose, we developed a module named the trigger logic module (TLM) which uses memory lookup-tables (MLT's) for logical operation. Fig. 4.7 shows the architecture of the TLM. The module can accept 4 local FLT cables (16bits for each cable), and also accept intermediate data from other TLM's into the entry points AA, AB, JB, JD and JE in Fig.4.7.[3] The input data are first of all sent into input-selectors which consist of programmable gate arrays. The function of the input-selectors is to select data and send them into appropriate MLT's with the correct timing. Each MLT has 16bits for input data and 4bits for output. The output data from each MLT are sent to output-selectors which consist of programmable array logics. The function of the output-selectors is to select data and feed them to appropriate local connection lines.

The trigger logic block is composed of TLM's. By using these TLM's sequentially, one can realize any trigger logic in principle. In case of GFLT, we adopt the sequential usage up to 3 TLM's. The main character of our MLT network is that the input and output of each MLT are restricted, but the connections between MLT's have large freedom thanks to the input-selectors and output-selectors. On the other hand, contents of MLT's can be changed by software but the configuration of input/output-selectors can not be modified online. Therefore the connections between MLT's (and hence the contents of the input/output-selectors) are the most important factors in the design work. Considering

[3]Data are transferred via local connection lines on the crate backplane.

the restricted I/O for MLT's, the key to a successful design is to realize only the useful combinations of the local FLT data, as well as to omit unnecessary combinations.

For this purpose, we classified MLT's conceptually into the following 4 categories:

1. Geometrical-Coincidence-MLT's
   The coincidence, logical-OR etc. of the regional information are made in these MLT's.

2. Threshold-MLT's
   Threshold values for (mainly) energy data are set in these MLT's. The threshold values are determined at the beginning of each run.

3. Trigger-Slot-MLT's
   The data for the trigger slots to the FDM's are made in these MLT's.

4. VETO-MLT's
   The data for the VETO-slots to the FDM's are made in these MLT's.

As the result, the conceptual design of the system is described in Fig.4.8. From this, the character of each MLT and corresponding input cables to each TLM were determined. One important restriction we imposed was that it was allowed to change the logic of the trigger-slot-MLT's and the threshold-MLT's on a run-by-run basis, but it was not the case for other MLT's. This restriction reduces the complexity of the design work.

The whole design was made up according to the above concept and restrictions. The entire system was a feed-forward network of about 160 MLT's on 21 TLM's.[4] Total number of bits for the input local FLT data is about 800, and the outputs are 64 subtrigger-slots and 8 VETO-slots. It was checked that all the useful trigger logics proposed by means of intensive Monte Carlo studies [65][66][71][72] could be realized. The next step was to write up all the input/output-selectors. Since the number of the programmable IC's were large, we developed a relational database system which automatically generated files necessary to write the input/output-selectors. The detail of the database system is the subject of the next section.

4.2.4 GFLT online logic database

By specifying the connections between MLT's as described in the previous section, the contents of the input-selectors and the output-selectors were also determined. This procedure was done automatically with a help of 'the GFLT online logic database'.

[4]We designed the system for the full data set so that we do not need to change anything when a currently missing data become available.

The main task of the database is the automatic routing. The database contains detailed knowledge about TLM which is hidden from a user. A user passes a sequence of instructions to the database. The main instructions are a command to define a new MLT network-unit and a command to add a hardware object (such as a MLT or an input/output-selector) to an existing network-unit. Here the network-unit is a set of hardware objects sharing the same data. By using these instructions iteratively, the whole MLT network is instructed to the database. The database compares user's inputs with its knowledge. If there is no problem, it executes the automatic routing and finally puts out all required pieces of information such as netlists for input/output-selectors. There is no need to write circuit diagrams or any intermediate file by hand to set up the input/output-selectors. This considerably reduced the time consumption and human errors on the implementation.

The GFLT online logic database is built with FORTRAN language with ADAMO (Aleph DAta MOdel [73]). ADAMO is based upon the entity-relationship model. A simple example to explain the entity-relationship model is shown in Fig. 4.9. In the figure, each of 3 boxes (named 'DATA', 'MLT' and 'TLM') is an 'entity set', which is a set of objects. Each entity set has 'attributes' such as 'Name' and 'Number_of_bit' for 'DATA'. Arrows between entity sets are 'relationships'. In the figure, the double arrow between 'MLT' and 'TLM' means that many MLT's belong to one TLM.[5] Similarly, the double arrow between 'MLT' and 'DATA' means that each trigger datum can be distributed to many MLT's. Though this example is quite simple, it includes the essence of our design work. While the relationship between 'MLT' and 'TLM' is static since it expresses just the hardware itself, the relationship between 'MLT' and 'DATA' directly holds the information on the MLT network. The MLT's having a relation to the same DATA are regarded to be connected.

Fig.4.10 is the entity-relationship diagram of the GFLT online logic database. Though it contains a lot of entity sets and relationships, the essence is similar to the simple example explained above. The entity sets in the upper half of the diagram denote hardware objects such as MLT input pins (O1MLUI in Fig.4.10) and so on. The lower half is mainly for data to be assigned to the hardware objects. The relationships inside the upper half of the diagram are static since they describe TLM's themselves, while the relationships between the upper and the lower halves contain our design of the MLT network.

4.2.5 Design of subtriggers

A subtrigger of GFLT is defined with a name, logic and trigger slot numbers in a similar manner to the struct of C language. One does not need to define details related to hardware, since such tasks are done automatically based upon the knowledge of the GFLT online logic database. The results are stored in the subtrigger database. At the beginning

[5] One to one correspondence is expressed with a single arrow.

of each run, a trigger configuration, which is a set of subtrigger names assigned to the trigger slots, is sent from the central run control to GFLT. It is then analyzed as bit patterns in MLT's with referring to the subtrigger database. In 1992, $\sim$ 250 subtriggers were prepared, including test-purpose subtriggers.

4.2.6 GFLT simulation code

For both Monte Carlo study and data validation, a GFLT simulation code was prepared and was merged into the ZEUS standard trigger Monte Carlo ZGANA [74]. Since a new subtrigger can be introduced online easily, it could happen that the subtrigger database is often updated. In this case the GFLT simulation code should be also updated quickly. As mentioned in the previous section, there were $\sim$ 250 subtriggers. Therefore it is very difficult to write and maintain the code by hand. To solve this problem, a tool called Offline Code Generator (OCG) has been developed to put out a FORTRAN source code automatically from the subtrigger database [75].

4.3 Trigger performance in 1992

Table 4.4 shows the summary of the ZEUS data taking conditions in 1992 [76]. The GFLT trigger rate was $\sim$10Hz since the beam current was lower than the nominal value. As shown in Table 4.4, there were 9 trigger modes as a result of gradual improvements of the trigger logic. The detail of each trigger mode is also summarized in Table 4.5. In the table, the names of the applied subtrigger logics are listed for each of the 9 trigger modes. If necessary, prescale factors were also attached to each subtrigger. In the following, we explain the some of the subtriggers on GFLT, GSLT and TLT used in physics runs.

Though the GFLT part in Table 4.5 looks complicated, the essence is simple, i.e. the entire logic consists of the DIS trigger, the photoproduction trigger, the muon trigger and test-purpose triggers. The logic for the DIS trigger was kept unchanged throughout the experiment[6]:

$$(\mathrm{EMC} \cup \mathrm{FCAL}) \text{ with C5 cut,}$$

where 'EMC' requires that any one of 16 regional EMC bits is on, and 'FCAL' requires any one of FCAL-HAC or FCAL-EMC bits is on. In the DIS trigger, C5 timing veto played an important role to suppress proton-gas events. As already displayed in Fig. 3.22, the proton timing and the electron timing are well separated in the C5 timing distribution, and thus the information is safe and effective to reject proton-gas events. The rejection

[6] The C5 timing veto was not applied at the very early stage, but this is not the problem since we re-applied the same C5 timing logic offline.

power of the C5 timing cut was 20-40% for events triggered by EMC, and 40-60% for events triggered by FCAL. [63]

The photoproduction trigger (named CAL*LUMI_Ee(4) in Table 4.5) was active for the most data (87% of the total luminosity). The logic was

$$\text{(any\_CAL\_bit on)} \cap \text{(Energy in LUMI EDET} > 4 \text{ GeV)}.$$

where (any_CAL_bit on) includes the RCAL-EMC 2nd threshold bits.

The muon trigger (named CAL_any*BMU in Table 4.5) was the coincidence between CAL and BMU. The logic was

$$\text{(any\_CAL\_bit on)} \cap \text{(any\_BMU\_region on)}.$$

We did not require the geometrical matching between CAL region and BMU region.

The GSLT rejection was applied for a part of data at the later stage of the luminosity running. Only for the CAL-FLT threshold Set-4 in which the BCAL-EMC had a lower threshold value than other settings, we rejected events if they satisfied all the following conditions:

- GFLT triggered only with the DIS trigger,
- BCAL total energy < 2.5 GeV,
- FCAL+RCAL total energy < 2.5 GeV.

This cut rejected a part of cosmic-rays or beam-associated muons, but the effect is completely negligible for DIS or LQ events.

Rejection of cosmic-ray events with the CTD SLT information was applied also if the muon trigger was the only fired subtrigger in GFLT. The rejection power of GSLT is summarized in Table 4.4. After the energy cut was applied, the rejection power ranged from 38% to 43%.

The main logic on TLT was 'CAL timing rejection' which killed events with bad CAL timing with relative to the beam collision. As described in Section 3.3.4, the time in each calorimeter cell is adjusted so that particles originating from the interaction point would hit the cell at 0ns. Many proton-gas events have activity upstream of the main detector, and thus particles hit RCAL directly. In such cases, the average time in RCAL is typically ~ -10.5 ns. If the proton-gas events also hit FCAL, the difference between FCAL and RCAL average time $(T_F - T_R)$ is ~ 10.5 ns. Therefore a cut on these quantities causes a considerable reduction of proton-gas events. Since the reliability of the time reconstruction depends on the amount of energy deposits in each cell, we applied the timing cut only if there were at least 2 PMT's with energy above 1 GeV in the beampipe region, which is the innermost ring of 8 towers in RCAL and inner 2 rings of 24 towers in FCAL. With taking a simple time average without energy weighting, we rejected events if they satisfied the following condition:

- $|T_F - T_R - 10.5| \leq 4.5ns$ and $|T_R + 10.5| \leq 4.5ns$

where T_F and T_R are the FCAL and RCAL average time of all PMT's above 1 GeV in the beampipe region. Fig. 4.11 shows the distribution of $T_F - T_R$ vs. T_R. We can see that proton-gas events and collision events are well separated, and hence the timing cut is a very safe and powerful trigger logic.

In order to suppress false triggers due to discharge of PMT's, an additional logic which checked the energy imbalance of the left and right PMT's in each trigger tower was introduced in TLT. This was called a 'spark rejection'. A spark cell was defined as a calorimeter cell with

$$E_L + E_R > 1.5 \text{ GeV}$$

and

$$|(E_L - E_R)/(E_L + E_R)| > 0.9,$$

where E_L and E_R are the left and right PMT energies, respectively. Then the event was rejected if it satisfied all the following conditions:[7]

- There was one and only one spark cell.
- The spark cell was in the trigger region that fired.
- (Total CAL energy) $-$ (Energy in the spark cell) ≤ 2.0 GeV.

The rejection power of TLT was summarized in Table 4.5. The rejection power generally depends on the trigger logic of GFLT and GSLT, and it ranged from 25% to 50%.

[7] At first this was applied for BCAL only, and later extended to the whole CAL.

Chapter 5

Monte Carlo Simulation

5.1 Overview of ZEUS offline software

Fig.5.1 shows a schematic overview of the ZEUS offline software. The entire system comprises the following parts:

- **ZDIS**; the Monte Carlo event generator
- **MOZART**; the detector simulator
- **ZGANA**; the trigger simulator
- **ZEPHYR**; the event reconstruction program
- **LAZE**; the event display
- **EAZE**; the user analysis package

All the parts are written in FORTRAN77 language coupled with ADAMO. ADAMO is fully used to realize the desired ZEUS event structure. ADAMO-TAP package [73] is extensively utilized everywhere to access data.

ZDIS consists of event generators and an interface to ADAMO. Four momenta of final particles are stored into ADAMO tables.

The ZDIS-output is processed with MOZART (MOnte Carlo for Zeus Analysis, Reconstruction and Trigger). MOZART makes use of the CERN GEANT program package [77] to simulate the behavior of particles through the whole detector. The program package GHEISHA [78] is used to describe the development of hadronic showers. The simulator EGS [79] is used for electromagnetic showers.

The output data of MOZART are again stored into ADAMO tables. In principle, the data have the same contents as real raw data, such as energy deposit in each CAL cell, hit

pattern in CTD etc. These are then read into ZGANA [74], the ZEUS trigger simulator, to check if the event passes the trigger logic.

The output data of ZGANA have both readout and trigger information, i.e. the equivalent information to the real data. ZEPHYR, the ZEUS PHYsics Reconstruction programme, can process both types of data. Thus the identical reconstruction of real events and Monte Carlo events is guaranteed. The detail of the reconstruction, especially on CAL, will be described in the next chapter.

The entire event shape can be looked at using the 2 dimensional event display LAZE, Look At Zeus Event. LAZE can read the MOZART output or the ZEPHYR output for both real and Monte Carlo data. In the following chapters, we will show LAZE outputs for some events taken in 1992.

ZEPHYR outputs for both real data and Monte Carlo data are the starting point of offline event selection. To minimize the effort for users to code programs, an analysis skeleton named EAZE, Effortless Analysis of Zeus Events, is widely used. In fact, any one of the programs mentioned above is based upon EAZE. EAZE is run with software switches named control cards which allow us to change conditions, parameters etc. without re-compiling/linking a program.

5.2 Event generator

5.2.1 Parton Density Functions

Parton density functions (PDF's in the following) are based upon perturbative QCD to determine Q^2 dependence. Parameters of PDF's are tuned to reproduce the results of various structure function measurements. There are many sets of PDF's nowadays. The difference among them comes from the different experimental data used for tuning, and from the different theoretical assumptions. The leading logarithmic approximation (LLA) was used in the old parameterizations, while recent ones are mostly based upon the next-to-leading logarithmic (NLL) evolutions. The functions with NLL are further categorized by the difference of the renormalization scheme, i.e. either with the $\overline{MS}$ scheme or the DIS scheme. The actual simulation was done using a library PDFLIB [80]. All PDF's in the library contain 4 flavours (u, d, c, s).

According to the narrow width approximation mentioned in Section 2.4.2, the production cross section of LQ is proportional to the parton density at a certain x ($= M_{LQ}^2/s$). Therefore choice of structure functions can influence the search result. However, as one can see from Fig. 5.2, predicted curves by various PDF's merge into a unique line above $x \sim 0.04$, which corresponds to $M_{LQ} \sim 60GeV$ at HERA. Thus the effect is expected to be small on a search for high-mass LQ. The effect of the different parameterizations for $M_{LQ} < 60$ GeV will be mentioned in Chapter 7.

For both DIS and LQ event generation, the parton density function MTB1 [81] has been used in this study. MTB1 is based upon the NLL evolution. Both $\overline{MS}$ and DIS renormalization schemes are available with MTB1. We chose the DIS scheme in this study. The function for each parton flavor is [81]:

$$xf(x,Q) = e^{A_0} x^{A_1} (1-x)^{A_2} (\ln(1+\frac{1}{x}))^{A_3},$$

where the parameters A_i with $i = 0-3$ are defined as:

$$A_i(Q) = C_0^i + C_1^i T(Q) + C_2^i T(Q)^2,$$

$$T(Q) = \ln \frac{\ln \frac{Q}{\Lambda_{QCD}}}{\ln \frac{Q_0}{\Lambda_{QCD}}}.$$

Hence the function includes 12 parameters for each flavor, C_j^i ($i = 0-3, j = 0-2$), which were tuned at ${Q_0}^2 = 4GeV^2$ with the DIS data from neutrino scattering experiments [82] and muon scattering experiments [23][83].

The QCD scale parameter, Λ_{QCD}, is 194 MeV. Since there is no way to determine the correct functional form of the PDF's in the framework of QCD, MTB1 function is also based upon some phenomenological considerations.

5.2.2 Leptoquark

The event generator LQUARK [84] was used to generate scalar and vector leptoquarks introduced in Chapter 2. In LQUARK, full integration of Born cross section including both s-channel and u-channel contributions are performed. Simulation of the interference between LQ and DIS was also available, but was ignored in our event generation and will be treated as a systematic effect. The Born cross sections agree well not only with the narrow width approximation but also with the results from other available generator PYTHIA [85]. To generate final hadrons from the decay quark and remnant quarks, we used the QCD cascade with the color dipole model[86] for the perturbative phase using ARIADNE [87]. The LUND string model in JETSET [88] [89] [90] was used for hadronization of the decay quark and the proton remnant.

The implementation of the realistic initial state bremsstrahlung of the beam electron is of vital importance since it directly affects the reconstructed x value. The leading logarithmic collinear approximation is used in LQUARK. The form of the splitting function for the hard bremsstrahlung contribution is given by

$$P(z) = \frac{\alpha}{2\pi} \log\left(\frac{\mu^2}{m_e^2}\right) \frac{1+z^2}{1-z},$$

where z is the ratio of the electron energy before and after radiation, μ^2 is equal to Q^2 for DIS or M_{LQ}^2 for resonances, α is the fine structure constant and m_e is electron mass. The splitting function has a singularity at $z = 1$, corresponding to low energy photons, which we cut off at $z = 1-\epsilon$, for $\epsilon = 0.001$. Below the cutoff, a flat distribution is used so that the total radiative contribution is kept finite.

5.2.3 Deep Inelastic Scattering

HERACLES4.1 [91] was used to generate both neutral current (NC) events with $Q^2 \geq 2GeV^2$, and charged current (CC) events with $Q^2 \geq 10GeV^2$. The generator calculates the cross section including electroweak radiative corrections to first order. Since the outputs of HERACLES are at the parton level, the perturbative QCD and the soft hadronization processes should be carried out to generate the final hadrons. The same tools as LQUARK were used; i.e. ARIADNE for the perturbative phase, and JETSET for hadronization. This combination is the best choice to reproduce the data taken by the NMC collaboration[92]. The details about the comparison of different generators are discussed by N. Magnussen et. al. [93].

Chapter 6

Event Selection

6.1 Trigger logic

The trigger logic we used was the following:

- GFLT : (any_EMC_bit ∪ any_FCAL_HAC_bit) with C5 cut,
- GSLT : no rejection, except the 'CAL energy cut' for CAL-FLT threshold Set-4,
- TLT : CAL timing rejection and spark rejection.

As described in Chapter 4, we used four different sets of the CAL-FLT threshold values and the difference can influence the trigger efficiency for DIS and LQ events. As listed in Table 4.4, the change from Set-1 to Set-2 is in the RCAL EMC non-beampipe region (2.5 GeV → 1.0 GeV). There is no change (except the RCAL 2nd thresholds) from Set-2 to Set-3. From Set-3 to Set-4, the change is in BCAL EMC (2.5 GeV → 1.0 GeV) coupled with the GSLT energy rejection. To check all the effect, we performed simulation studies on the trigger efficiencies for LQ events with various masses as well as for DIS events. The simulation took into account the CAL-FLT bad channels. Therefore the effect of hardware inefficiency is included. Table 4.6 shows the results. In the table, the effect of the GSLT energy cut for Set-4 is not listed, since it turns out to be completely negligible. From the table, it is seen that the CAL-FLT acceptance is always very high for LQ decaying into an electron and a quark; i.e. above 98.3% for scalar LQ with $50GeV \leq M_{LQ} \leq 225GeV$, and above 97.6% for vector LQ with $40GeV \leq M_{LQ} \leq 225GeV$. Most of the events not triggered had very small-angle electrons which went down to the rear beampipe or deposited energy below the threshold in the RCAL EMC cells. Thus we conclude that our trigger system was almost perfect for the mode LQ → eq.

As for NC events with $Q^2 \geq 2GeV^2$, the acceptance is 55.2% with Set-1 and 58.1% with other sets. The rejected events were populated in low Q^2 region. With a tighter cut

$Q^2 \geq 30GeV^2$ at the generator level, the acceptance is above 97.0% which is comparable to the acceptance for the mode LQ → eq.

For the most CC events, the final state hadronic particles do not hit RCAL. Therefore the change of the RCAL threshold does not influence the acceptance. As listed in Table 4.6, the efficiency goes up from 81.1% to 89.0% by lowering the BCAL EMC threshold.

For the mode LQ → νq with $M_{LQ} \geq 100GeV$, there is no significant difference in the trigger acceptance. The acceptance is above 91.5% for scalar LQ with $M_{LQ} \geq 100GeV$ and above 90.0% for vector LQ with $M_{LQ} \geq 100GeV$. For CC events and LQ → νq mode, the final state hadrons spread over many calorimeter cells, though CAL-FLT compares the energy deposited in 2 towers with a threshold value. As a result only a part of the total energy is compared with a threshold value. This is the reason why the acceptances are generally a bit lower than that for NC events and LQ → eq mode.

Below $M_{LQ} = 100GeV$, however, the effect of the different thresholds is not negligible. Especially the effect of decreasing the BCAL EMC threshold (difference between Set-2/3 and Set-4) is sizable; i.e. the increase of the acceptance is 18% for scalar LQ with $M_{LQ} = 50GeV$, and 46% for vector LQ with $M_{LQ} = 40GeV$. To take this effect into account in our analysis, we gave each Monte Carlo event a weight based on the integrated luminosity for each CAL-FLT threshold set; e.g. if the event is accepted by all of the threshold sets, the weight is 1. If the event is triggered only by Set-4, the weight is 0.34.

6.2 Fast Reconstruction and Pre-selection of Data

The data taken were processed quickly with the official reconstruction program ZEPHYR. For this purpose, 3 Silicon Graphics multiprocessor machines (SGI480 UNIX stations), each of which was equipped with 6 processors, were exclusively used. [94].

In order to reduce the number of events at the very early stage, the reconstructed data were then processed with a filter program for an initial selection of physics events. The aim of the filter program is to reject clear background events while keeping various kinds of collision events, and then to classify the collision events. During the luminosity runs in 1992, the filter consisted of four independent preselection algorithms named 'DIS' (to select deep inelastic scattering candidates), 'BGF' (to select boson gluon fusion candidates), 'photoproduction', and 'exotics'.[1] Events which passed any one of these preselections were stored in the ZEUS Data Summary Tapes (ZEUS-DST's). The DST's were distributed to ZEUS collaborators for further offline analyses. The whole procedure is schematically shown in Fig. 6.1.

In the analysis in this thesis, events selected with the exotics-preselection were chosen

[1] some other criteria were also implemented for the test purpose.

for the further analysis. Since the information from CAL was extensively used in the exotics-preselection, first we explain some details on the calorimeter reconstruction in ZEPHYR. Then we explain the exotics-preselection criteria.

6.2.1 Calorimeter reconstruction

The reconstruction of CAL starts from making energy (in MeV) and time (in ns) in each calorimeter cell. After that, a cluster finding job starts. We used 2 methods to find electron candidates; the condensate-algorithm and the cone-algorithm.

The condensate-algorithm starts from picking up all the cells with energy above a certain threshold value ($= T_1$). Among these cells, cells adjacent to each other are considered to belong to the same local cluster[2]. There is no restriction in the number of cells in a local cluster. In the extreme case, a single isolated cell with energy above T_1 is regarded as a local cluster. The values of T_1 were 60MeV for EMC and 110MeV for HAC. After finding out all the local clusters, the total energy in each of them is compared with another threshold value (T_2). If the energy exceeds T_2, the local cluster is defined as a 'condensate'. The value of T_2 was 200MeV.

To identify the condensate as an electron, we required the following 3 criteria:

- $(E_{EMC}/E \geq 0.85) \cap (E_{EMC4}/E_{EMC} \geq 0.85)$
- $(N_{HAC1} \leq 4) \cap (N_{HAC2} = 0)$
- $(E \geq 2GeV \cap N_{EMC} \leq 10) \cup$
  $(E \geq 5GeV \cap N_{EMC} \leq 12) \cup$
  $(E \geq 40GeV \cap N_{EMC} \leq 14)$

where $E, E_{EMC}, E_{HAC1}, E_{HAC2}$ are energy deposits in all cells, EMC cells, HAC1 cells and HAC2 cells in the condensate, respectively. E_{EMC4} is the energy in the 4 most energetic EMC cells in the condensate. $N_{EMC}, N_{HAC1}, N_{HAC2}$ are the numbers of cells in the condensate. The first item means that the energy in the condensate should be mainly contained in the EMC cells. The second and the third criteria mean that the number of cells belonging to the condensate should be consistent with that of a typical electron.

The condensate algorithm is quite reliable for finding well-isolated electrons. However, since the condensate has been introduced as a basic object to find pions and muons also, there is no assumption for the size of a cluster. If an electron is located close to hadrons, the electron cluster and the hadron cluster may be merged into a single large condensate. In this case the condensate can not be regarded as an electron. This can have a considerable effect for very massive LQ events, in that electrons are likely to be found in FCAL where a jet is also found.

[2]Adjacent cells share at least a part of its side.

On the other hand, the cone-algorithm is based on the fixed cluster size suitable for electrons. The algorithm starts from finding the most energetic EMC cell. Then all EMC cells located within a cone angle of θ_1 from the energetic cell and HAC cells within a cone angle of θ_2 make a energetic inner 'cone'. An outer cone is also made with θ_3 for EMC and with θ_4 for HAC. If the ratios of total energy deposits in EMC-inner, EMC-outer, HAC-inner and HAC-outer cones fit an electron, the cone is identified as an electron candidate. If not, the same procedure is applied for the next most energetic EMC cell.[3] The chosen values for the cone angles are $\theta_1 = 0.1$, $\theta_2 = 0.2$, $\theta_3 = 0.2$ and $\theta_4 = 0.4$ in radian.

The purpose of the condensate-algorithm and the cone-algorithm described above is to find an electron candidate with high efficiency without demanding very good energy and position resolution of the electron. The final electron reconstruction for better energy and position resolution is explained in Section 6.3.

6.2.2 Preselection for Exotic Physics

In the exotics-preselection, any candidate for a high transverse energy (high-E_t), a charged current (CC), or a neutral current (NC) event is selected. To start with, the total 4-momenta for the event (P_x, P_y, P_z, E) and the transverse energy E_t are calculated by summing over all calorimeter cells with energy greater than 200 MeV and with left-right energy imbalance less than 0.7. Then the event is regarded as a high-E_t event if the condition, $E_t > 40\ GeV$, is satisfied. If another criterion, $P_t > 10GeV$, is satisfied, where $P_t = \sqrt{P_x^2 + P_y^2}$, the event is regarded as a CC candidate. If an electron is found either with the condensate-algorithm[4] or with the cone-algorithm, and the cut, $\delta \equiv E - P_z > 20GeV$ which will be explained below, is satisfied, the event is regarded as a NC candidate. These definitions are not exclusive, i.e. one event can be both a NC candidate and a high-E_t event.

The variable δ has been used for the NC candidate selection because it is effective to separate collision events from backgrounds, and it is insensitive to the energy leakage in the beampipe in the forward region. For a NC event, all the final particles, except that going down to the beampipe, are caught by the main detector. As a result, δ should be the same as that in the initial state (i.e. twice as large as the electron beam energy) due to 4-momentum conservation. In reality, many remnant particles go down to the forward beampipe, and are not detected by the main detector. However, this energy leakage is almost cancelled out in the calculation of δ. Only if the initial electron emits an energetic photon (initial state radiation), the photon goes down to the rear beampipe and the

[3]This is applied up to 10th most energetic cell.

[4]To tell the detail, we also applied 2 additional electron finders based upon the condensate-algorithm. If any one of the 3 finders found an electron, the condensate was regarded as an electron. The difference among the finders was small.

energy leakage is doubly emphasized in δ. Therefore the distribution of δ for NC events is expected to have a peak around twice as large as the electron beam energy (i.e. 53.4 GeV) with a lower tail due to the initial state radiation.

Since δ is sensitive to the energy leakage to the rear beampipe, the main consequence of the δ cut for the NC candidate selection is to reduce photoproduction events in which the final state electrons go down to the beampipe in the rear side. [5] The chosen threshold (20 GeV) is yet rather loose and still a lot of photoproduction events survived the cut. A tighter cut on δ will be applied at the later stage (see Section 6.5.1).

Among the selected high-E_t, CC and NC candidates, events with bad timing with relative to the beam collision were discarded. The essence of the timing cut applied in the exotics-selection is the same as that used on TLT which was described in Section 4.3. However we applied a tighter cut utilizing all PMT's of CAL. The details of the timing cut are described in Appendix A.1.

In addition to the timing cut, events triggered due to some hardware faults were checked and thrown away. This procedure is based upon the calorimeter bad PMT list which is updated regularly using the data taken by calibration runs. An event was rejected if the highest energy cell in the calorimeter had a bad PMT and if the total energy without this cell is less than 2 GeV.

Some cosmic-ray events were also rejected by checking the pattern of CAL energy deposit. The algorithm is rather loose to reject events only if there is a clear hit pattern in CAL, i.e. cells along a straight line. The details of the algorithm are described in Appendix B.

With careful efficiency studies, all the cuts applied in the exotics-selection turned out to be very safe for DIS events and LQ events. The fraction of the events that survived these cuts ranged from 3% to 12% of the recorded events depending upon the machine luminosity and the trigger condition. The acceptance of physics events with the filter will be described in Section 6.5.2 (for NC events) and Section 6.6 (for CC events).

In this analysis, further offline selections were carried out to obtain pure NC samples from the pre-selected NC candidates, and pure CC samples from the pre-selected CC samples.[6] In the selection of the pure NC samples, the refined electron finder played an essential role. The algorithm and the performance of the electron finder are described in the next section.

[5] Some cosmic-rays and proton-gas events are also rejected with the cut on δ.

[6] High-P_t events were not used in this analysis.

6.3 Refined electron reconstruction

The refined electron finder consists of two parts; first finding electromagnetic-clusters (EM-clusters) without any bias of event types, then among them selecting the best electron candidate suitable for LQ. The EM-cluster finding is based upon the energy deposits in calorimeter cells only. No other information such as CAL timing nor tracks in CTD was used. The algorithm is similar to the cone algorithm described in the previous section. However, the refined electron finder is based upon a pattern of electron energy deposit within a smaller radius compared with the cone algorithm, and hence it does not impose stringent isolation requirement for an electron.

The algorithm starts from finding the most energetic EMC cell. An EM-cluster consists of EMC cells within the radius R_{EMC} ($= 10R_M$) and HAC cells within the radius R_{HAC} ($= 16R_M$) from the most energetic cell, where R_M ($= 2.02$ cm) is the effective Moliere radius of CAL. The radii were determined by Monte Carlo studies. The validity of these radii was also confirmed by the beam test results of prototype modules. In the calculation of the distance from the most energetic cell, the position of each cell is defined as the weighted energy center of the left and right PMT's for the cell. For the found EM-cluster, E^e_{EMC}, E^e_{HAC} and E^e_{tot} ($=E^e_{EMC}+E^e_{HAC}$) denote the total energy in the EMC cells, in the HAC cells and in all the cells belonging to the EM-cluster, respectively. Since a typical electron contains almost all the energy in the EMC cells, the quantity $L_e = E^e_{HAC}/E^e_{tot}$ should be small and can be used as a measure for the longitudinal energy spread. As for the transverse energy spread, the quantity $T_e = E^e_{EMC4}/E^e_{tot}$, where E^e_{EMC4} denotes the energy sum of the 4 most energetic EMC cells in the EM-cluster, is expected to be ~ 1 for an electron. Using the quantities L_e and T_e, the EM-cluster is regarded as an electron candidate if it satisfies the following condition:

$$(L_e \leq 0.1) \ \cap \ (T_e \geq L_e + 0.6).$$

This condition can be transformed to

$$\xi_e \equiv min(0.1, T_e - 0.6) - L_e \geq 0.$$

Fig. 6.2 (a), (b) and (c) show the examples of ξ_e-distributions for Monte Carlo data of single electrons (shaded histograms) and pions in FCAL, BCAL and RCAL, respectively. It is seen that the cut at 0 efficiently separates electrons from pions.

The procedure described above is applied for up to 10 most energetic EMC cells. Among the selected electron candidates, the most energetic one is chosen for further examination to select LQ or NC events. Since it is difficult to perform precise reconstruction of electrons hitting very close to the beampipe, the following position cuts are also applied:

$$\sqrt{X_e^2 + Y_e^2} \geq 20 \ cm \quad \text{for RCAL,}$$

and

$$\sqrt{X_e^2 + Y_e^2} \geq 36\ cm \quad \text{for FCAL,}$$

where X_e and Y_e are the position of the electron in CAL defined as the weighted mean of the energy spread. The larger cutoff value is chosen for FCAL compared with that for RCAL, since cells close to the FCAL beampipe are hit by many remnant particles and hence it is difficult to find out an electron in such a region. Assuming that a collision occurred at the nominal interaction point, these criteria correspond to $9° \leq \theta_e \leq 172°$. If the most energetic electron candidate is rejected with the position cut, the next most energetic candidate is examined, and this procedure continues until an electron is found or all the candidates are rejected.

The performance of the electron finder was checked with Monte Carlo events of single e^- and π^- with various energies. The results are summarized in Table 6.1. Energy values chosen in Table 6.1 are typical ones which are allowed kinematically in each CAL region. The detection efficiency of a single isolated electron is quite high and is above 96.7% over the energy range of 15-200 GeV, with less than 6.8% of pion contamination. The probability of pion contamination decreases to below 1.9% for energy above 80 GeV. The performance of the electron finder for LQ and NC events is also summarized in Table 6.1. The reconstructed energy and angle of electrons have good resolutions and are also consistent with the true values at the generator level. Thus we conclude that the refined electron finder works well for the reconstruction of LQ and NC events.

6.4 Reconstruction of x, y and Q^2

A precise reconstruction of kinematical variables x, y, Q^2 is quite important both for reliable event selection and for a good mass reconstruction of LQ. As discussed in Chapter 2, the event kinematics is completely determined with two independent variables. In case of the CC process, there are just two observable quantities only, but the reconstruction method is not unique depending on what observed quantities are used. Conventionally the Jacquet-Blondel method (JB method) [95] is used to obtain x, y, Q^2 for the CC process:

$$y_{JB} = \frac{\sum_h (E_h - p_{zh})}{2E_e}$$

$$Q^2_{JB} = \frac{(\sum_h p_{xh})^2 + (\sum_h p_{yh})^2}{1 - y_{JB}}$$

$$x_{JB} = \frac{Q^2_{JB}}{s \cdot y_{JB}},$$

where $(p_{xh}, p_{yh}, p_{zh}, E_h)$ is the 4-momentum of each hadronic particle, and the sum $\sum_h$ runs over all the hadronic particles in the final state. This method is widely used because

it does not need to separate a current jet from a remnant jet, and is insensitive to the energy leakage into the forward beampipe.

In case of NC, there are four observable quantities, i.e. the energy (E'_e) and angle (θ_e) of the scattered electron, the total hadronic energy ($\sum_h E_h$) and the angle (γ_h) made of the final hadronic system. Therefore any combination of two variables out of these four quantities (including the JB method) can be used. A naive reconstruction method is to use E'_e and θ_e:

$$y_e = 1 - \frac{E'_e}{2E_e}(1 - \cos\theta_e),$$

$$Q^2_e = 2E_e E'_e(1 + \cos\theta_e),$$

$$x_e = \frac{E_e}{E_p} \cdot \frac{E'_e(1 + \cos\theta_e)}{2E_e - E'_e(1 - \cos\theta_e)}.$$

With detailed studies [96], however, it turns out that the double angle method (DA method) using θ_e and γ_h is better in a very wide kinematical range:

$$y_{DA} = \frac{\sin\theta_e \cdot (1 - \cos\gamma_h)}{\sin\gamma_h + \sin\theta_e - \sin(\theta_e + \gamma_h)},$$

$$Q^2_{DA} = 4E_e^2 \cdot \frac{\sin\gamma_h \cdot (1 + \cos\theta_e)}{\sin\gamma_h + \sin\theta_e - \sin(\theta_e + \gamma_h)},$$

$$x_{DA} = \frac{E_e}{E_p} \cdot \frac{\sin\gamma_h + \sin\theta_e + \sin(\theta_e + \gamma_h)}{\sin\gamma_h + \sin\theta_e - \sin(\theta_e + \gamma_h)}.$$

Another advantage of the DA method is that it is insensitive to the absolute energy calibration of CAL. Also energy leakage of hadronic particles into the forward beampipe does not affect γ_h greatly, since γ_h is obtained from p_{xh}, p_{yh}, and $E_h - p_{zh}$ which are insensitive to the leakage. The actual equation is as follows:

$$\cos\gamma_h = \frac{(\sum_h p_{xh})^2 + (\sum_h p_{yh})^2 - (\sum_h (E_h - p_{zh}))^2}{(\sum_h p_{xh})^2 + (\sum_h p_{yh})^2 + (\sum_h (E_h - p_{zh}))^2}.$$

Therefore we decided to choose the DA method in the analysis of NC samples.

6.5 Selection for $LQ \to e^- + X$

6.5.1 Selection of NC samples

Total number of pre-selected NC candidates were 25818. Because of the loose criteria in the pre-selection, the selected samples are still dominated by cosmic-rays, beam-gas events and events with fake electrons. Fig. 6.3 is an event display of a typical cosmic-ray

events and events with fake electrons. Fig. 6.3 is an event display of a typical cosmic-ray event in which a fake electron was found at the exotics-preselection, and the event was regarded as a NC candidate. A lot of cosmic-ray events were still found in the pre-selected events. They are found mainly in BCAL and RCAL where the threshold values of the CAL-FLT are much lower than that of FCAL as described in Section 4.3. Also many proton-gas events and electron-gas events remain in the samples. Fig. 6.4 and Fig. 6.5 are a typical proton-gas and an electron-gas event, respectively. These events survived the C5 and TLT timing rejection.

Table 6.2 summarizes the offline selection criteria for $LQ \to e^- + X$ with number of survived events. There are many criteria, but the philosophy of the selection is simple: First we select NC samples with the kinematical region as wide as possible without any bias for LQ events, then we reject a region in $x - y$ plane where few LQ samples are expected to locate. Below we explain all the cuts step by step.

1. Collision bunch examination

   Bunch crossing number of each event was checked and events not associated with collision bunches were rejected. The rejected events are later used to estimate the amount of contamination from proton-gas events and electron-gas events.

2. Cut on energy in LUMI EDET (E^e_{LUMI})

   Events were rejected if LUMI EDET contained energy above 5 GeV. Fig. 6.6 (a) shows the distribution of E^e_{LUMI}. It is seen that the cut on 5 GeV is appropriate. Fig. 6.6 (b) shows the δ distribution for events with $E^e_{LUMI} > 5$ GeV (the non-shaded area), together with events with $E^e_{LUMI} < 5$ GeV (the shaded area). While the shaded area has a peak on ~ 50 GeV which is consistent with the NC process, the rejected events have much lower values of δ. This implies that a scattered electron goes down to the rear beampipe and hits LUMI EDET. If this is the case, the electron found in the main detector at the exotics-preselection is a fake electron. To confirm this, we show the distribution for $(E - P_z + 2E^e_{LUMI})$ for the rejected events in Fig. 6.6 (c). The peak on ~ 50 GeV in the figure is an evidence that the rejected events have scattered electrons in LUMI EDET, i.e. they are mainly photoproduction events.[8]

3. Final timing cut

   The more stringent timing cut than that in the pre-selection was applied at this stage. The details of the final timing cut are described in Appendix A.2. The algorithm itself is very similar to that used in the pre-selection described in Appendix A.1. The main difference is in the choice of some parameters.

[8]The rejected events are later used to estimate contamination of photoproduction events.

Fig. 6.7 shows the distribution of (FCAL time - RCAL time) before and after the timing cuts. Events in the shaded area have passed the timing cuts. From the figures we can see that the main consequence of the final timing cuts is to remove the small secondary peak around 8 ns. As mentioned in Section 3.1, this peak is due to the electron satellite bunches coming about 8ns earlier than the primary bunches.

Small number of background events with bad timing still survive the timing cuts. A part of such events can be rejected with a cut on RCAL total energy, which is described next.

4. RCAL total energy cut

   Beam-gas events or cosmic-rays can deposit energies larger than the kinematical limit in RCAL. The maximum energy deposit (ER_{max}) kinematically allowed in RCAL is

   $$ER_{max} = \frac{E_e E_p}{E_p \sin^2(\frac{\theta_{min}}{2}) + E_e \cos^2(\frac{\theta_{min}}{2})} = 33.6 GeV,$$

   where $E_e = 26.7 GeV$ and $E_p = 820 GeV$. When a particle comes from the nominal interaction point, θ_{min} is 129.1° which is the angle for the boundary of RCAL and BCAL. Assuming that the proton bunch length is 40 cm, θ_{min} is 125°. Taking fluctuation of energy measurement into account, the possible maximum energy is

   $$ER_{max} + 0.35\sqrt{ER_{max}} + 0.02 ER_{max} \simeq 36.3 GeV$$

   where we used the energy resolution for HAC as an extreme case that all particles are hadrons. Thus we chose 37 GeV as an allowed upper limit for RCAL total energy. Fig. 6.8 shows RCAL energy distribution before this cut. With this cut, events in the shaded area in the figure were saved for further study.

5. Electron energy and position cut

   Energy and position of electrons were determined using the refined electron finder described in Section 6.3. Events having an electron with energy above 10 GeV ($E_e > 10\ GeV$) were saved. This energy cut considerably reduces the contamination of fake electrons.

   As described in Section 6.3, a position cut for the found electron was also applied intrinsically in the electron finder. The cut on the RCAL position rejects many low-x and low-Q^2 events for which we can not perform a precise reconstruction. To check the fraction of such discarded events, we re-applied the electron finder without the position cut. Fig. 6.9 shows impact positions of the electrons found in RCAL with energy greater than 10 GeV, without imposing the position cut. The edge of the RCAL is clearly seen, though the position resolution is generally not so good for the electron hitting the innermost cells. Out of all events having an electron

with $E_e > 10\ GeV$, 59.3% of the events were discarded with the F/RCAL (mostly RCAL) position cut applied in the electron finder.

We did not use any track information to tag electrons. Therefore we do not know on an event-by-event basis if the electron we found is really a charged particle. Monte Carlo simulation studies show, however, that there is no event type having an energetic photon with a considerable cross section. We have also checked with Monte Carlo DIS events that the electron finder seldom fails to tag the correct electron except a small contamination from an energetic photon found in the hadron jets. To reject such fake electrons, we rejected events with very large y value, which is explained next.

6. Fake electron rejection

   At this stage, we still have events with fake electrons in FCAL. Though an electron in NC or LQ events can be found in FCAL in principle, it should have very large energy. In case of a fake electron, however, energy is not so large. The small values for θ_e and E_e make y_e close to unity. Fig. 6.10 shows the y_e-distribution. An excess at $y_e \sim 1$ is seen. Therefore we rejected these events. The selection criterion is $y_e < 0.96$.

Due to the long proton bunch length (typically $\sim$ 50 cm), the systematic effect of the position of the event vertex to the reconstruction is not negligible. In other words, resolutions of x, y and Q^2 become better with using Z of event vertices reconstructed with CTD. The reconstruction for CTD in ZEPHYR starts with finding tracks from hits in SL1, SL3 and SL5. The pattern recognition algorithm is based on the Kalman filtering method [97]. The vertex reconstruction algorithm [98] in ZEPHYR is based on the least-squares method but is faster than the standard way. The time consumption is proportional to the number of tracks.

Fig. 6.11 shows the distribution of Z for preselected samples. The peak at negative Z values is due to proton-gas interaction. On the other hand, the selected samples, shown by the shaded area, are centered on the nominal interaction point. With a gaussian fitting, the rms of the Z distribution is 27 cm, which agrees with a half of the mean proton bunch length of $\sim$ 25 cm. At this stage, 74.8 % of selected events have reliable vertices with $|Z| < 75cm$. The reconstructed Z is used to calculate x, y and Q^2. Z = 0 is used if CTD failed to find a good vertex. After doing this procedure, the following additional selection criteria were applied:

7. Cut on $\delta\ (= E - P_z)$

   Using the Z-vertex information of CTD, a tighter cut, $\delta > 30\ GeV$, was applied. Fig. 6.12 is the δ distribution. Since the contamination of the photoproduction events is already small at this stage, the effect of this cut is not so large; i.e. only 146 events out of 3272 events were rejected.

8. Cut on the sum of FCAL and BCAL total energy

   A typical feature of an electron-gas event is that there is an electron in the RCAL (mostly in the cells next to the beampipe) and almost nothing in other area. To reject them, a cut on the sum of FCAL energy (E_F) and BCAL energy (E_B) was applied. Fig. 6.13 shows the distribution of $E_F + E_B$.

9. P_t conservation cut

   The net transverse momentum should be conserved in NC events. Therefore events with a large transverse momentum P_t were rejected with the following cut:

   $$P_t \leq Max(10GeV,\ 3\sqrt{E_t}),$$

   where E_t is the net transverse energy in GeV. Fig. 6.14 is a scattered plot in P_t vs. E_t plane before this cut. Events above the solid line were rejected. The rejected events are mainly beam halo muons or cosmic rays penetrating a half of the detector and consequently showing the relation, $P_t \sim E_t$.

10. Rejection of low-y events

    Events with $y_{JB} < 0.05$ are removed since the resolution of kinematical variables becomes worse in this region and the measurements suffer from systematic biases coming from the effects of noise and the finite segmentation of the CAL [99]. The JB method was used for the cut since it gives a good resolution in the low y region and it is not influenced by events with fake electrons.

11. Tight electron position cut in RCAL

    There are complex materials around the beampipe and still some materials may be missing without being recognized in the Monte Carlo program MOZART. As a result, we can not guarantee a precise reconstruction for the electrons found in the RCAL-towers next to the beampipe. Therefore we applied the following cut:

    $$\sqrt{X_e^2 + Y_e^2} \geq 30\ cm \quad \text{in RCAL.}$$

    Electrons from LQ decays seldom hit this region. The rejected events are predominantly with low-x, low-y and low-Q^2 values. The cut also effectively rejects remaining boson-gluon fusion events having the scattered electrons in the RCAL beampipe towers.

After all these cuts, 719 events remained. In order to reconstruct x, y and Q^2 with the DA method, first we compared the reconstructed angles of the electron (θ_e) and the hadronic system (γ_h) with Monte Carlo expectation. We show the results in Fig. 6.15.

Data are shown by points with statistical errors, and Monte Carlo expectation is displayed with histograms which is normalized with the measured integrated luminosity ($= 26.6\ nb^{-1}$). The data agree well with the Monte Carlo expectation. Based upon these angles, x and Q^2 are reconstructed with the DA method. The results are shown in Fig. 6.16 and in Fig. 6.17. The agreement in these figures is an evidence that most events in the survived samples are NC events. No clear peak is observed in x distribution. A LAZE event display of a typical NC event is also shown in Fig. 6.18.

6.5.2 Further reduction in the kinematical plane

As discussed in Section 2.4.2, we can reduce NC events effectively by rejecting events with low y value, since NC events follow $\sim 1/y^2$ distribution. If we use a cut, $y_{JB} > 0.1$, the efficiencies for scalar LQ and vector LQ (with either $g_L = 0$ or $g_R = 0$) are ~ 0.9 and ~ 0.7, respectively. This holds even if we are searching for very massive LQ in high-x region. Since the DIS cross section in high-x region is very low, there is no need to apply the y-cut in this region. To save such high-x and low-y LQ events, an event having a high-Pt electron is also saved. The chosen threshold value is 20 GeV to avoid a contamination of fake electrons. Together with a cut, $x_{DA} > 0.001$, to reject events with very low x values, the final selection to obtain LQ search samples is

$$(y_{JB} > 0.1 \text{ or } P_t^{elec} > 20\ GeV) \ \ and \ \ x_{DA} > 0.001.$$

Purely analytically, the cut on the electron Pt (P_t^{elec}) can be regarded as a y-cut with the x-dependent threshold value (y_{cut}), since the threshold T is related to y_{cut} with the following equation:

$$y_{cut}^2 - y_{cut} + \frac{T^2}{sx} = 0.$$

We can see that $1/x$ is a parabolic function of y_{cut} which falls down with increasing x, or M_{LQ} as well from the relation $M_{LQ}^2 = sx$. For example with $T = 20\ GeV$, the values of y_{cut} are 0.5 for $M_{LQ} = 40$ GeV, 0.1 for 67 GeV, and 0.05 for 92 GeV, respectively. Since we already applied the cut $y_{JB} > 0.05$ for the NC events selection, almost all the LQ events with $M_{LQ} > 92$ GeV pass the final cut. It should be stressed that P_t^{elec} distribution of LQ forms a Jacobian peak. In this sense the cut on P_t^{elec} is a reasonable cut with a clear motivation, rather than applying some x-dependent function to determine y_{cut}.

Fig. 6.19 and Fig. 6.20 show the y_{JB}-distribution and the P_t^{elec} distribution for selected NC samples, respectively. In the both distributions, the data agree well with the Monte Carlo expectation of NC events. Fig. 6.21 also shows the event distribution in $y_{JB} - P_t^{elec}$ plane.

With this final cut, 346 events remained. Fig. 6.22 shows the distribution of x_{DA} for the LQ search samples (points with statistical errors) with Monte Carlo NC events

(histograms). No clear peak is observed. Among the survived events, 3 events are with x above 0.1. These 3 events have an electron in BCAL. The values of x_{DA}, Q_{DA}^2, y_{DA} and P_t^{elec} for these events are listed in Table 6.3. Fig. 6.24 is the LAZE event picture for one of them with $x_{DA} = 0.10$, $Q_{DA}^2 = 2.9 \times 10^3 GeV^2$ and $y_{DA} = 0.32$. There is no event above $x = 0.2$ which corresponds to $M_{LQ} = 130$ GeV.

To study the overall efficiencies for LQ, Monte Carlo events were generated with

- $M_{LQ} = 50, 75, 100, 125, 150, 175, 200, 225$ GeV for scalar LQ
- $M_{LQ} = 40, 75, 100, 125, 150, 175, 200, 225$ GeV for vector LQ.

The entire selection procedure was applied for all these Monte Carlo events. The results are summarized in Table 6.4. The efficiency was above 84.1% for scalar LQ and above 68.7% for vector LQ. One remark is that the filtering efficiency is kept high for very massive LQ. For $M_{LQ} = 225 GeV$, efficiency is above 85% for both scalar and vector LQ. Fig. 6.23 shows the final LQ search samples with a scalar LQ resonance (shaded histogram) on $M_{LQ} = 175 GeV$ with $g_R = 0.31$, i.e. the electroweak coupling, and with $g_L = 0$. The displayed range is $0 \leq x_{DA} \leq 0.6$ which corresponds to $0 \leq M_{LQ} \leq 230 GeV$. It is seen that a clear excess should be observed if LQ existed.

6.5.3 Background estimation

As shown in the previous section, the good agreement on the distributions of kinematical variables between the final samples and the Monte Carlo data for NC events implies that the background contamination is negligible. To confirm this, we performed background estimation in various ways. First of all, all the final LQ search samples were visually scanned with the event display LAZE. Out of 346 events, 342 events (98.8%) were regarded as NC events. Among them, 334 events (96.5%) were clear NC events. 7 events could be photoproduction events because of the bad isolation and the low energy of the reconstructed electrons. For one event with an electron in RCAL, the electron finder failed to tag this electron and found a fake electron in FCAL. Thus the reconstructed value of $x_{DA} (= 0.44 \times 10^{-2})$ was wrong. The correct value was estimated to be 1.0×10^{-2}.

It turns out that there are 4 background events. Among them 3 events could be regarded as cosmic rays. The characteristics of these events are that there is a large energy deposit only in BCAL EMC, which was misidentified as an electron, and the particle penetrates BCAL and RCAL. The reconstructed Bjorken-x of these events are less than 5.6×10^{-3}. One event with $x_{DA} = 1.2 \times 10^{-2}$ was classified as a coincidence of a proton-gas event and a cosmic ray which caused a fake electron.

Since all the background events are located in low x region where much more NC events are also found, the effect of these background events is very small. Therefore we did not exclude them from the final samples.

In addition to the visual scanning, we estimated contamination of beam-gas events and photoproduction events in the following ways:

- Proton-gas interaction
  The whole filtering process except the selection of the collision bunches was applied for all events. No event on the proton pilot bunch survived the cut sequence. This result indicates that the contamination of proton-gas interaction is less than 6.0% at 90% CL.

- Electron-gas interaction
  Similarly, no event on the electron pilot bunch survived the cut sequence. Even with the selection of NC samples, no event remained. This result indicates that the contamination of electron-gas interaction is less than 2.9% at 90% CL.

- Photoproduction with a fake electron
  In the low Q^2 photoproduction processes, the final state electron goes down to the rear beampipe. However, if a fake electron, such as γ from π^0 decays, is found in the debris of a hadron shower, the event would be misidentified as a NC event. Due to the huge production cross section of such processes, they can be a serious background. Monte Carlo studies [99] show that about one-quarter of photoproduction events will have an electron tagged by the LUMI detector.[9] Assuming that the LUMI-tagged photoproduction events show the similar activity in the main detector as the non-tagged events, we can estimate the photoproduction background by applying the whole filtering procedure for events with an electron tagged by the LUMI detector. The whole filtering procedure but with a condition $E^e_{LUMI} > 5\ GeV$ was applied for all events. We got 2 events remained with $x_{DA} \leq 0.26 \times 10^{-2}$. As a result, the contamination of photoproduction events is estimated to be less than 3.8% at 90% CL.

As a summary, 96.5% of the LQ search samples have been regarded as NC events with the visual scanning. All possible background events are populated in the low x region with $x_{DA} \leq 1.2 \times 10^{-2}$ (corresponding to $M_{LQ} \leq 32GeV$), where we also have much more NC events. Therefore we conclude that the effect of background contamination is negligible on the search for LQ.

6.6 Selection of CC events

The whole selection sequence of CC events is listed in Table 6.2 with the number of survived events. The selection of CC events is more difficult than that for NC events,

[9] This has been confirmed also with the real data in the analysis of hard photoproduction processes [100].

since the final state is similar to proton-gas events except the fact that a CC event can have a large missing transverse momentum. Total number of pre-selected CC candidates are 18777, which are dominated by proton-gas events and cosmic-ray events. The earlier stage of cut sequence is similar to that of NC selection; i.e. with the collision bunch selection, $E^e_{LUMI} < 5\ GeV$, the final timing cut, and RCAL Energy $< 37\ GeV$. Then we required that a good vertex was reconstructed with $|Z| < 75cm$. 1200 events remained after the vertex requirement.

These events are still dominated by backgrounds. Fig. 6.25 shows the Py vs. Px distribution for these events. There is a clear asymmetry in Px. Almost all events have negative Px values. To know the origin of this asymmetry, we selected one run which showed this Px asymmetry and checked the original Px distribution before applying the Pt cut. The result is shown in Fig 6.26 (a). A secondary peak at around -5 GeV is seen in addition to the primary peak centered at 0. The asymmetry in our selected sample is due to the tail of this secondary peak. With further investigation, the following facts were understood on the events in the secondary peak:

- The secondary peak is not always seen. It is seen when the beam condition is relatively bad. This indicates that this phenomenon is associated with the beam.

- The events in the secondary peak (secondary events in the following) survive RCAL timing cuts; i.e. no or less energy is seen in RCAL. In addition, they do not have a track in most cases. Activity is seen mainly in FCAL.

- Fig 6.26 (b) shows the FCAL energy vs. Px distribution. We see that the secondary events populate in the region around FCAL energy $\sim$ 200 GeV, while the events contained in the primary peak do not have such distribution.

- By looking at the energy deposit pattern in FCAL, it turns out that one FCAL supertower next to the beampipe in $-X$ direction is the most energetic in more than 90% of the secondary events. The secondary peak almost disappears if we mask the energy deposit in this tower. The energy in this tower has a peak at $\sim$ 70 GeV (this is the threshold value of CAL-FLT) which corresponds to Px $=\sim -5$ GeV.

- Fig 6.26 (c)-(e) show the energy imbalance between the left and right PMT's in the most energetic EMC, HAC1 and HAC2 towers for secondary events. The energy imbalance is small in HAC1 and HAC2, but large in EMC. A consistent hypothesis is that particles mainly enter the FCAL HAC towers from the beampipe side as schematically shown in Fig 6.27. In this case, energy is seen only by the inner PMT of EMC because the wavelength shifter next to the beampipe is hit by the particles which produce a large signal. The time distributions of the most energetic EMC, HAC1 and HAC2 towers for secondary events are shown in Fig 6.26 (f)-(h). HAC1

and HAC2 have the proton beam timing. This indicates that particles come from the proton side. EMC shows the early timing which can be caused by the direct hit to the wavelength shifter. Therefore the time distributions are also consistent with the hypothesis.

All the above facts indicated that there was some activity by proton beam halo particles at the very near location to FCAL. The most probable candidate of this activity is the synchrotron radiation collimator C4 which is located at the position of FCAL EMC in the beampipe. As schematically shown in Fig 6.27, C4 in $-X$ side is not protected by C5, but $+X$ side is protected.[10] Thus more proton halo particles attack C4 in $-X$ side without making activity in RCAL. A test with different collimator positions indicated that the magnitude of the secondary peak in Px depended on the collimator position.

Our solution to reject the secondary events is to re-make Pt without FCAL towers near the beampipe. By ignoring FCAL towers within the cone angle of $\theta < 13.8°$, only 38 events survived against the cut (re-made-Pt $> 10GeV$). Finally a cut ($x_{JB} > 0.01$) was applied and 16 events remained. These were scanned visually and 14 events were clearly not CC candidates. They consist of cosmic rays (7 events), NC (3 events), coincidence of proton-gas and a halo muon (3 events), and coincidence of a cosmic ray and a proton-gas event (1 event). The remaining 2 events did not have any clear reason to be rejected. Thus we regard them as final CC candidates to be used to set the mass and coupling constraint for LQ.

The same selection sequence was applied for Monte Carlo CC events (HERACLES) with $Q^2 > 10GeV^2$. The estimated number of events is 0.96, which is consistent with the result for the real data.

Table 6.5 shows the kinematical variables of the 2 CC candidates. One candidate has a considerably large Q^2 value (above $10^4 GeV^2$). The expected number of such high-Q^2 CC events is 0.09. Fig. 6.28 is the picture of this event.

To study the overall efficiencies for LQ, Monte Carlo events were generated at the same masses as that for the $LQ \to eq$ mode. The entire selection procedure was applied for all these Monte Carlo events. The results are summarized in Table 6.6. The efficiency was above 67.5% for scalar LQ and above 45.2% for vector LQ.

[10] Since the synchrotron radiation itself has horizontal asymmetry, C4 and C5 also have horizontal asymmetry.

Chapter 7

Results

7.1 Constraint for Mass and Coupling of LQ

In the previous chapter, we checked that there was no significant excess on the x distribution of the LQ search samples (both for NC and CC). Therefore in this chapter we derive a constraint on the existence of scalar and vector LQ. Since there are 2 free parameters, i.e. mass (M_{LQ}) and coupling (g_L or g_R), we obtain the constraint as a boundary line in the coupling vs. mass plane. For simplicity, we assume either $g_L = 0$ or $g_R = 0$.

We used a standard method to estimate a limit on the signal in background according to the Poisson statistics [101]. Let μ_B be the mean for the sum of all backgrounds. Assuming that μ_B is known with a negligible error, when we observe n_0 events, an upper limit on signals in the n_0 events (N) is given with the following equation:

$$1 - \frac{e^{-(\mu_B+N)} \sum_{n=0}^{n_0} \frac{(\mu_B+N)^n}{n!}}{e^{-\mu_B} \sum_{n=0}^{n_0} \frac{\mu_B^n}{n!}} = CL$$

where CL is a confidence level, for which we chose 0.95 in this analysis to obtain the 95% confidence limit. Then an upper limit of LQ cross section (σ_{lim}) is obtained from

$$N = \sigma_{lim} \cdot \varepsilon_{LQ} \cdot L,$$

where ε_{LQ} is the overall selection efficiency for LQ and L is the integrated luminosity. From σ_{lim}, we finally get an upper limit on the coupling at each LQ mass.

To obtain n_0 for each mass for the case $LQ \to e^- + X$, we first of all fit the final x_{DA} distribution of LQ at each mass with a Gaussian function to obtain the mean (μ_x) and the standard deviation (σ_x) of the reconstructed resonance. For example, Fig. 7.1 is the case of scalar LQ with $M_{LQ} = 175GeV$. We can see the clear peak and hence the fitting

procedure is carried out successfully. Then we define n_0 as the number of observed events within

$$|x_{DA} - \mu_x| < 3\sigma_x.$$

The same range is used to obtain μ_B from Monte Carlo NC events.

Fig. 7.2 (a) and (b) show plots of μ_x as a function of M_{LQ} for scalar LQ and vector LQ, respectively. The solid curves in the figures are for the exact solution $\mu_x = M_{LQ}^2/s$. The reconstructed peak agrees with the exact solution. Fig. 7.2 (c) and (d) are σ_x for each generated mass point. From the figures it is seen that the resolution of the resonance for vector LQ is a little worse than that for scalar LQ. This originates from the y dependence of the resolution of x_{DA}; i.e. the resolution of x_{DA} is worse in low-y region [96] where massive vector LQ events with the chiral coupling are more populated (following $\sim (1-y)^2$ distribution as mentioned in Section 2.4.2) than scalar LQ events which follow the flat y distribution.

To obtain n_0 for each M_{LQ} for the case $LQ \to \nu_e + X$, we simply count up all entries in the final samples; i.e. the range $0.01 < x_{JB} < 1$ is regarded as one big bin. As mentioned in Section 2.4.2, the branching ratio to the decay $LQ \to e^- + X$ depends on the coupling. In case both decays can exist, we set a combined limit.

Fig. 7.3 shows σ_{lim} for (a) scalar LQ and (b) vector LQ. The result is a measure for not only LQ but also other possible resonant states decaying into $e^- + X$ or $\nu_e + X$. The difference between scalar and vector LQ comes from the reconstructed peak width (σ_x) and the selection efficiency (ε_{LQ}).

Table 6.7 shows the upper limits of coupling constants for various masses and types of LQ. By interpolating these values with a spline method, we obtain the coupling limit for arbitrary value of M_{LQ}. For example, Fig. 7.4 (a) and (b) show the upper limits on the coupling of S_0 and $V_{1/2}$, respectively. Assuming the electroweak coupling ($g = 0.31$), the mass constraint for S_0 is

$$M_{LQ} > \begin{cases} 180\ GeV & \text{with } g_L{=}0.31,\ g_R{=}0, \\ 196\ GeV & \text{with } g_L{=}0,\ g_R{=}0.31, \end{cases}$$

and the mass constraint for $V_{1/2}$ is

$$M_{LQ} > \begin{cases} 176\ GeV & \text{with } g_L{=}0.31,\ g_R{=}0, \\ 216\ GeV & \text{with } g_L{=}0,\ g_R{=}0.31, \end{cases}$$

These results exceed the present experimental bounds obtained with e^+e^- and $p\bar{p}$ colliders. The results for all other types are listed in Table 6.8. Due to the difference of the cross section for each type of LQ, the mass limits range from $105GeV$ to $196GeV$ for scalar LQ, and range from $111GeV$ to $216GeV$ for vector LQ. The difference of the cross section (and consequently the mass limits) comes from the fact that the parton densities of valence quarks are larger than that of sea quarks in high-x region. LQ with the fermion number

(F) = 2 (S_0, $\tilde{S}_0$, S_1, $V_{1/2}$ and $\tilde{V}_{1/2}$) can make a resonance with valence quarks. Hence the cross section is sizable up to large mass region. On the contrary, LQ with F = 0 ($S_{1/2}$, $\tilde{S}_{1/2}$, V_0, $\tilde{V}_0$ and V_1) make a resonance only with sea quarks. Therefore the cross section falls steeply in the large mass region.[1] The mass limits for vector LQ are a bit higher than that for scalar LQ, since the production cross section of vector LQ is twice as large as that of scalar LQ thanks to the freedom of spin as mentioned in Section 2.4.2.

7.2 Systematic uncertainty

We checked the systematic uncertainty of the coupling limits. The coupling limits are influenced by the systematic error of the integrated luminosity (6%), LQ cross section ($1-10\%$ with the mass dependence and including the effect of initial state radiation and LQ-DIS interference), and the overall selection efficiency for LQ ($1-7\%$ for $LQ \to eq$ and $1-6\%$ for $LQ \to \nu q$ with the mass dependence). In the mass region with events observed, we also have to consider the uncertainty of the Monte Carlo DIS background expectation (4% for CC and small for NC except in the region $M_{LQ} < 50GeV$ where the uncertainty is 20%), which mainly comes from the ambiguity of the parton density functions obtained by comparing MTB1 with MTB2, since most of parton density functions lie between these 2 parameterizations. As a result, the coupling limits would shift upward by $4-6\%$ for examined mass points above 150 GeV, and by $3-6\%$ for examined mass points below 125 GeV. The detail of the possible increase of the limit for each mass of LQ is listed in Table 6.7. The mass limits at the electroweak coupling are influenced also by the above systematic effects. The mass limits would shift downward by $2-3$GeV.

[1] The situation becomes opposite if the e^+p collision experiment is performed at HERA in the future.

Chapter 8

Conclusions

We searched for leptoquarks as s-channel resonances decaying into $e^- + jet$ or $\nu + jet$ in electron-proton collisions at $\sqrt{s} = 300GeV$. With integrated luminosity of $26.6 \pm 1.6\ nb^{-1}$ collected with the ZEUS detector at HERA, first we extracted neutral current (NC) and charged current (CC) events mainly using the uranium-scintillator calorimeter. We obtained 719 NC events and 2 CC events. For the NC events, the Bjorken variables x, y and Q^2 were reconstructed with the double-angle method. These distributions showed good agreements with the expectation of the Standard Model. Further cuts in the kinematical plane were applied to enhance the possible signals of leptoquarks. Finally 346 NC events survived, and there was no evidence for leptoquarks. The number of CC events was also consistent with the expectation of the Standard Model.

Limits on the coupling strength of scalar (vector) leptoquarks to electron and quark have been determined for masses from 50 (40) GeV to 225 GeV. The limit changes by changing a choice of quantum numbers of leptoquarks since the cross section, the decay branching ratio, and the selection efficiency depend on the quantum numbers. We classified leptoquarks into 10 types with the model independent effective lagrangian with dimensionless, SU(3)×SU(2)×U(1) invariant couplings to quark-lepton pairs. We ruled out a completely new search region beyond the present experimental bounds from e^+e^- and $p\bar{p}$ colliders.

A limit on the leptoquark mass has been also obtained at the 95% confidence level assuming that either left-handed or right-handed coupling exists to the electron-quark pair with electroweak strength. Leptoquarks are ruled out for masses below 216 GeV with the largest cross section and below 105 GeV with the smallest cross section.

Appendix A

Calorimeter timing cuts

A.1 Calorimeter timing cuts in exotics-preselection

There are various checking items in the timing algorithms of the exotics-preselection. But the essence of the timing cuts is simple; i.e. the reconstructed time should be consistent with the beam crossing timing in any region of the CAL. If we can reconstruct time reliably and it is inconsistent with the collision timing, we discard the event. Below we summarize the whole selection.

First of all, the TLT timing cut is applied with different cut values. To reject proton-gas events which are already shown in Fig. 4.11, events satisfying the following condition are rejected:

$$|T_{Fbp} - T_{Rbp} + 14ns| < 6ns \ \cap \ |T_{Rbp} + 12ns| < 6ns.$$

Then the following cuts are also applied;

1. FCAL timing cuts

   To start with, we find PMT's with energy above 200 MeV in the beampipe region of FCAL. Here the definition of the beampipe region is the same as that used in the TLT algorithm (see Section 4.3). Number of PMT's found is denoted as N. E is total energy with these PMT's. Then we calculate the energy-weighted average time (T_W) with these PMT's;

   $$T_W = (\sum_{PMT's} w_{PMT} \cdot T_{PMT})/(\sum_{PMT's} w_{PMT}),$$

   where T_{PMT} and w_{PMT} are the time and weight of each PMT. The weight w_{PMT} is defined as $1/(\delta T_{PMT})^2$, where δT_{PMT} is the error on the measured time of each

PMT calculated as a function of the PMT energy (E_{PMT});

$$\delta T_{PMT} = 1.157 + \frac{1.695}{\sqrt{E_{PMT}(GeV)}}\ (ns).$$

(This formula was obtained by special runs utilizing the light flasher system described in Section 3.3.3).

In order to check if we could reconstruct the average time reliably, we also introduce the average error on the measured time,σ_T, and χ^2_T;

$$\sigma_T = (\sum_{PMT's} \frac{1}{(\delta T_{PMT})^2})^{-\frac{1}{2}},$$

$$\chi^2_T = \sum_{PMT's} (\frac{T_{PMT} - T_W}{\delta T_{PMT}})^2.$$

With above values, we reject an event which satisfies both of the following conditions;

$$|T_W| > Max(6, 3\sigma_T) \text{ ns}$$

$$N \geq 4 \ \cap \ \chi^2_T/(N-1) \leq 3 \ \cap \ E > 1GeV.$$

The first condition is the main cut to check if the event is out of time. The second condition is used to ascertain that the average time is reconstructed reliably.

The same procedure is also applied using all the FCAL PMT's with energy above 80 MeV. In this case, the required number of PMT's to reject an event is 6, instead of 4. All the other logic is identical.

2. RCAL timing cuts

   Exactly the same procedure for the entire FCAL is applied for the entire RCAL. Also the same procedure for the FCAL beampipe region is applied for the RCAL beampipe region. The definition of the RCAL beampipe region is the same as that used in the TLT algorithm (see Section 4.3).

3. Global timing cut

   Last of all, we make a cut using PMT's with energy above 80 MeV in the entire CAL. For these PMT's, the following rejection cut is applied;

$$|T_W| > Max(8, 4\sigma_T) \text{ ns} \ \cap \ N \geq 16.$$

A.2 Calorimeter final timing cut in the offline selection

The final timing cut used offline is very similar to that in the exotics-preselection. The difference is in the choice of parameters. The final timing cut consists of following 4 criteria;

- FCAL timing cut
  To start with, using all the FCAL PMT's with energy above 80 MeV ($E_{PMT} > 80$ MeV), an event is rejected if it satisfies both of the following conditions;

$$|T_W| > Max(6, 3\sigma_T) \text{ ns}$$

$$N \geq 4 \ \cap \ \chi^2_T/(N-1) \leq 3 \ \cap \ E > 1GeV,$$

  where the notations are the same as those defined in the exotics-preselection. This is the same procedure as the FCAL timing cut in the exotics-preselection, except that $N \geq 4$ is required instead of $N \geq 6$. Thus more events become objects of the timing cut.

  The same procedure is applied for $E_{PMT} > 200$ MeV with $N \geq 2$, and also for $E_{PMT} > 1$ GeV with $N \geq 2$.

- RCAL timing cut
  Using all the RCAL PMT's with energy above 80 MeV, an event is rejected if it satisfies both of the following conditions;

$$T_W < Min(-4.5, -3\sigma_T) \text{ ns} \ \cup \ T_W > Max(6, 3\sigma_T) \text{ ns}$$

$$N \geq 4 \ \cap \ \chi^2_T/(N-1) \leq 3 \ \cap \ E > 1GeV.$$

  Compared with the RCAL timing cut in the pre-selection, the more stringent lower cutoff (= -4.5 ns) for T_W is used. In addition, $N \geq 4$ is required instead of $N \geq 6$.

  The same procedure is applied for $E_{PMT} > 200$ MeV and $N \geq 2$, and also for $E_{PMT} > 1$ GeV and $N \geq 2$.

- Global timing cut
  Using PMT's with energy above 80 MeV in the entire CAL, an event is rejected if it satisfies the following condition;

$$|T_W| > Max(6, 4\sigma_T) \text{ ns} \ \cap \ N \geq 8.$$

  The logic is the same as that in the pre-selection, except that the more stringent cutoff for T_W is used with the more loose requirement for the value of N.

- FCAL - RCAL timing cut
  If both FCAL and RCAL average times are reconstructed reliably, i.e. if they satisfy the requirements on N, $\chi^2_T/(N-1)$ and E described above, the event is rejected if it satisfies the following condition on the difference of the FCAL and RCAL average time;

$$|T_{WF} - T_{WR}| > Max(6, 3\sqrt{\sigma^2_{TF} + \sigma^2_{TR}}) \text{ ns.}$$

  This procedure is done for PMT's with $E_{PMT} > 80$ MeV, $E_{PMT} > 200$ MeV, and $E_{PMT} > 1$ GeV.

Appendix B

Cosmic muon rejection in the preselection

The cosmic muon rejection is based upon the calorimeter information. No information from tracking devices is used. Its purpose is to reject an event only if there is a clear hit pattern in CAL, i.e. cells along a straight line. In other words, an event survives the rejection criteria unless there is a concrete evidence for a cosmic muon.

Throughout the whole algorithm, only calorimeter cells with energy above 100 MeV are used. N_F, N_B and N_R are defined as the number of cells with energy above 100 MeV in FCAL, BCAL and RCAL, respectively. N_{tot} is the total number of cells found; i.e. $N_{tot} = N_F + N_B + N_R$. N_1 is number of cells in the most active calorimeter region, i.e. $N_1 = Max(N_F, N_B, N_R)$. Out of N_1 hit cells in this region, N_{eff} is the number of cells which have at least one adjacent hit cell. In other words, this region has $N_1 - N_{eff}$ isolated cells. Out of these N_{eff} cells, N_{emc} and E_{emc} are number of cells and energy sum of EMC cells.

First of all, an event satisfying any of the following conditions is NOT a cosmic muon candidate;

- $N_{tot} \geq 100$.
- $N_1 \leq 2$.
- With too much activity around the beampipe.
- $N_{eff} < 3$.
- $N_{emc} \geq (N_{eff} - 1)$ and $E_{emc} > N_{emc}(\text{GeV})$.

After that only the most active calorimeter region is further investigated. First of all, N_{eff} non-isolated cells are projected onto x-z plane for BCAL and onto x-y plane for

FCAL and RCAL. Then the correlation coefficient (R_{12}) and the circularity (C_{12}) on this plane are calculated (C_{12} is defined as the smallest eigenvalue of the sphericity tensor). The same calculation is done also on x-y plane for BCAL and on x-z plane on FCAL and RCAL, in order to obtain R_{13} and C_{13}. D_{mu} denotes the length of the straight hit pattern (in meter).

Then an event is defined as a cosmic muon (and is rejected) when it satisfies all the following criteria;

- $N_{eff} \geq 4$ and $|R_{12}| \geq 0.7$.
- $C_{12} < 0.1$ or $D_{mu} > 3$ or ($C_{12} < 0.15$ and $|R_{12}| \geq 0.8$ and $|R_{13}| \geq 0.7$).
- A cut on the continuity of hit cells.

In addition, an event in BCAL is also regarded as a cosmic muon with satisfying all the following criteria;

- The most active region is BCAL.
- $|R_{12}| \geq 0.9$ and $|R_{13}| \geq 0.9$ and $C_{12} < 0.1$ and $C_{13} < 0.1$.

Last of all, there is an additional cut. Though a clear cosmic muon is found, there may be other activities in other parts of CAL. In this case the event is NOT regarded as a cosmic muon. The cut is;

- NOT a cosmic muon if $E_{tot} - E_1 \geq 10GeV$ or $N_1 - N_{eff} > 4$,

where E_{tot} and E_1 are the energy in the whole calorimeter and in the most active region.

Above is a minimum explanation necessary for the analysis in this thesis. The entire cosmic muon finder has some additional options and is more complicated. The complete detail is found elsewhere [102].

Acknowledgements

I would like to express my special thanks to Prof. S. Yamada for suggesting me this theme and giving me a lot of appropriate advice throughout my study.

I express my cordial thanks to Dr. K. Tokushuku for teaching me various experimental techniques, and for many useful discussions. I am also grateful to Mr. M. Nakao and Mr. Y. Yamazaki for working together on GFLT.

A part of the offline analysis in this thesis has been carried out in the ZEUS exotic physics group during my stay at DESY. I wish to thank Prof. F. Sciulli, the leader of the group, for his various suggestions. I also acknowledge Prof. E. Lohrmann, Dr. U. Schneekloth and Dr. M. Nakahata for their kind help on the study of CC background events. Discussions and cooperation of all the other members in the exotic physics group were inevitable and are greatly appreciated. I am also grateful to Dr. M. Kuze and Dr. S. Nagayama for stimulus discussions during my stay at DESY.

Various discussions on data analysis with Dr. T. Hasegawa and Dr. T. Nagira are cordially appreciated. I also express my thanks to the collaborators at Tokyo Metropolitan University for allowing me to use workstations to generate a part of huge Monte Carlo events. I am also grateful to Dr. T. Ishii, Dr. S. Kasai, Mr. Y. Nagasawa, and Dr. T. Watanabe for fruitful discussions on the ZEUS experiment.

The HERA machine group is acknowledged for the great effort on the operation of the collider.

Last of all I thank my family for the continuous support.

Bibliography

[1] J.-E. Augustin et al., Phys. Rev. Lett. **33** (1974) 1406.

[2] J. J. Aubert et al., Phys. Rev. Lett. **33** (1974) 1404.

[3] C. Bacci et al., Phys. Rev. Lett. **33** (1974) 1408.

[4] DASP Collaboration, W. Braunschweig et al., Phys. Lett. **B53** (1974) 393.

[5] G. S. Abrams et al., Phys. Rev. Lett. **33** (1974) 1453.

[6] DASP Collaboration, W. Braunschweig et al., Phys. Lett. **B63** (1976) 471.
DASP Collaboration, R. Brandelik et al., Phys. Lett. **B70** (1977) 125.

[7] G. Goldhaber et al., Phys. Rev. Lett. **37** (1976) 255.
I. Peruzzi et al., Phys. Rev. Lett. **37** (1976) 569.

[8] For review, M. L. Perl, Proceedings of international symposium on lepton and photon interactions at high energies P.145, Hamburg (August 1977).

[9] DASP Collaboration, W. Brandelik et al., Phys. Lett. **B73** (1978) 109.

[10] Tasso Collaboration, R. Brandelik et al., Phys. Lett. **B86** (1979) 243.
MARK J Collaboration, D. P. Barber et al., Phys. Rev. Lett. **43** (1979) 830.
PLUTO Collaboration, Ch. Berger et al., Phys. Lett. **B86** (1979) 418.
JADE Collaboration, W. Bartel et al., Phys. Lett. **B91** (1980) 142.

[11] UA1 Collaboration, G. Arnison et al., Phys. Lett. **B122** (1983) 103.
UA2 Collaboration, M. Banner et al., Phys. Lett. **B122** (1983) 476.
UA1 Collaboration, G. Arnison et al., Phys. Lett. **B126** (1983) 398.
UA2 Collaboration, P. Bagnaia et al., Phys. Lett. **B129** (1983) 130.

[12] S. Weinberg, Phys. Rev. Lett. **19** (1967) 1264.
A. Salam, in: Elementary Particle Theory, ed. N. Svartholm (Almquist and Wiksells, Stockholm, 1969) p.367.

[13] E. D. Bloom et al., Phys. Rev. Lett. **23** (1969) 930.

[14] T. Eichten et al., Phys. Lett. **B46** (1973) 274.

[15] F. J. Hasert et al., Phys. Lett. **B46** (1973) 138.

[16] R. P. Feynman, Phys. Rev. Lett. **23** (1969) 1415.

[17] D. J. Gross and F. Wilczek, Phys. Rev. Lett. **30** (1973) 1343.
H. D. Politzer, Phys. Rev. Lett. **30** (1973) 1346.

[18] K. Charchula, M. Krawczyk and H. Abramowicz, DESY **90-019** (1990) .

[19] See for example, V. D. Barger and R. J. N. Phillips.
Collider Physics.
Addison-Wesley Publishing Company, 1987.

[20] G. Ingelman et al., HERA Workshop 1987, Vol.1, p.3.

[21] C. G. Callan and D. Gross, Phys. Rev. Lett. **22** (1969) 156.

[22] A. Bodek et al., Phys. Rev. **D20** (1979) 1471.

[23] J. J. Aubert et al., Nucl. Phys. **B293** (1987) 740.

[24] ZEUS Collaboration, M. Derrick et al., Phys. Lett. **B293** (1992) 465.

[25] Articles on Physics Beyond the Standard Model,
HERA Workshop 1991, Vol.2, p.1029.

[26] See for example, P. Langacker, Phys. Reports **72** (1981) 185.

[27] W. Buchmüller and D. Wyler, Phys. Lett. **B177** (1986) 377.

[28] See for example, J. L. Hewett and T. G. Rizzo, Physics Reports **183** (1989) 193.

[29] P. Candelas, G. Horowitz, A. Strominger and E. Witten, Nucl. Phys. **B258** (1985) 46.

[30] H. Murayama and T. Yanagida, Tohoku Univ. Preprint **TU-370** (1991) .

[31] H. Murayama, private communication.

[32] See for example, E. Farhi and L. Susskind, Phys. Reports **74** (1981) 277.

[33] J. Wudka, Phys. Lett. **B167** (1986) 337.

[34] L. F. Abbott and E. Farhi, Phys. Lett. **B101** (1981) 69;
Nucl. Phys. **B189** (1981) 547.

[35] W. Buchmüller, R. Rückl and D. Wyler, Phys. Lett. **B191** (1987) 442.

[36] T. Köhler, Diplomarbeit at the RWTH Aachen (1989).

[37] J. L. Hewett and T. G. Rizzo, Phys. Rev. **D36** (1987) 3367.

[38] OPAL Collaboration, G. Alexander et al., Phys. Lett. **B263** (1991) 123.

[39] L3 Collaboration, B. Adeva et al., Phys. Lett. **B261** (1991) 169.

[40] ALEPH Collaboration, D. Decamp et al., Phys. Rep. **216** (1992) 253.

[41] DELPHI Collaboration, P. Abreu et al., Phys. Lett. **B275** (1991) 222.

[42] UA2 Collaboration, J. Alitti et al., Phys. Lett. **B274** (1992) 507.

[43] CDF Collaboration, S. Moulding et al., presentation at the Seventh Meeting of the American Physical Society (DPF) Fermilab (November 1992).

[44] O. Shanker, Nucl. Phys. **B204** (1982) 375.

[45] B. Schrempp, HERA Workshop 1991, Vol.3, p.1034.

[46] T. Åkesson et. al., Nucl. Instr. and Meth. **A241** (1985) 17.

[47] R. Yoshida, DESY **92-159** (1991)
A. Caldwell et. al., ZEUS-Note **93-021** (1993).

[48] J. Krüger, DESY **F35-92-02** (1992) .

[49] J. Hartmann et. al., Nucl. Instr. and Meth. **A305** (1991) 366.

[50] L. Hervás, Doctoral dissertation, DESY **F35D-91-01** (1991)
A. Caldwell et. al., Nucl. Instr. and Meth. **A321** (1992) 356.

[51] W. Buttler et. al., Nucl. Instr. and Meth. **A277** (1989) 217.
W. Sippach et. al., IEEE Trans. Nucl. Sci. **NS-36** (1989) 465.

[52] A. Caldwell et. al., ZEUS-Note **93-021** (1993) .

[53] A. Andresen et. al., Nucl. Instr. and Meth. **A309** (1991) 101.

[54] ZEUS Calorimeter Group, U. Behrens et. al., Nucl. Instr. and Meth. **A289** (1990) 115.
ZEUS Calorimeter Group, A. Andresen et. al., Nucl. Instr. and Meth. **A290** (1990) 95.

[55] ZEUS, a Detector for HERA, Letter of Intent, DESY (June 1985)
The ZEUS Detector, Technical Proposal, DESY (March 1986)
The ZEUS Detector, Status Report 1987, DESY (September 1987)
The ZEUS Detector, Status Report 1989, DESY (March 1989).

[56] C. B. Brooks et. al., Nucl. Instr. and Meth. **A283** (1989) 477.

[57] G. Blair et. al., ZEUS-Note **92-122** (1992) .

[58] P. E. Luffman and K. R. Long, ZEUS-Note **92-97** (1992) .

[59] J. Andruszków et. al., ZEUS-Note, **90-108** (1990)
J. Andruszków et. al., ZEUS-Note, **90-125** (1990).

[60] J. Andruszków et. al., DESY, **92-066** (1992)
ZEUS LUMI group, Talk given at a ZEUS internal meeting, 15 Sep. 1992.

[61] K. Piotrzkowski, private communication.

[62] W. Schott et al., ZEUS-Note **93-002** (1993) .

[63] S. Mine, Master thesis, Univ. of Tokyo, (1993).

[64] W. Smith et. al., ZEUS-Note **89-084** (1989) .

[65] J. Biltzinger et. al., ZEUS-Note **91-051** (1991)
R. Schattevoy and J. Biltzinger, ZEUS-Note **91-101** (1991).

[66] H. Uijterwaal, Academisch proefschrift, NIKHEF (1992).

[67] INMOS. The Transputer Databook Second Edition, INMOS (1989).
T. Woeniger, DESY **90-024** (1990).

[68] ZEUS Data Acquisition Group, DESY **92-150** (1992) .

[69] W. H. Smith et. al., ZEUS-Note **92-103** (1992) .

[70] K. Tokushuku, GFLT Design Document I, Feb.7 (1990).

[71] T. Hasegawa, K. Tokushuku and S. Yamada, ZEUS-Note **89-100** (1989) .

[72] T. Kinnel, S. Silverstein, C. Foudas and W. Smith, ZEUS-Note **90-056** (1990) .

[73] ALEPH Collaboration, The ADAMO programmer's manual. Ver3.2.

[74] ZGANA Manual, Ver3.04 and corrections.

[75] Y. Yamazaki, Master thesis, Univ. of Tokyo, (1993).

[76] B. Foster, R. Nania, R. Talaga and R. Walczak, ZEUS-Note **93-030** (1993) .

[77] GEANT 3, R. Brun et al., report DD/EE/83-1, CERN (1989).

[78] H. Fesefeldt, PITHA **85/02** (1985) .

[79] W. Nelson, H. Hirayama and D. Rogers, SLAC-Report **265** (1985) .

[80] H. Plothow-Besch, CERN-PPE **92-123** (1992) .

[81] J. G. Morfin and W. K. Tung, Z.Phys. **C52** (1991) 13.

[82] J. P. Berge et al., CERN-EP **89-103** (1989) .

[83] A. C. Benvenuti et al., Phys. Lett. **B223** (1989) 485.

[84] D. Gingrich, Monte Carlo Generator for Leptoquark Production in Lepton-Proton Collisions. LQUARK version 3.01/02.

[85] T. Sjöstrand, CERN-TH **92-6488** (1992) .

[86] B. Andersson et al., Z. Phys. **C43** (1989) 625.

[87] L. Lönnblad, HERA Workshop 1991, Vol.3, p.1440.

[88] T. Sjöstrand, Comp. Phys. Comm. **39** (1986) 347.

[89] T. Sjöstrand and M. Bengtsson, Comp. Phys. Comm. **43** (1987) 367.

[90] T. Sjöstrand, Int. J. Mod. Phys. **A3** (1988) 751.

[91] A. Kwiatkowski, H. Spiesberger and H. -J. Möhring, HERA Workshop 1991, Vol.3, p.1294.

[92] NMC Collaboration, P. Amaudruz et al., Phys. Lett. **B295** (1992) 159.

[93] N. Magnussen et al., HERA Workshop 1991, Vol.3, p.1167.

[94] The ZEUS Detector, Status Report 1993, Chapter 17, DESY (February 1993).

[95] F. Jacquet and A. Blondel in Proceedings of the study of an ep facility for Europe 79/48 (1979), p.391-394, U. Amaldi ed.

[96] S. Bentvelsen, J. Engelen and P. Kooijman, HERA Workshop 1991, Vol.1, p.23.

[97] P. Billoir and S. Qian, Nucl. Instr. and Meth. **A294** (1992) 219.

[98] P. Billoir and S. Qian, Nucl. Instr. and Meth. **A311** (1992) 139.

[99] ZEUS Collaboration, M. Derrick et al., DESY **92-180** (1992) .

[100] ZEUS Collaboration, M. Derrick et al., Phys. Lett. **B297** (1992) 404.

[101] Particle Data Group, Phys. Rev. **D45** (1992) III.40.

[102] H. Abramowicz, Subroutine IsitaMU in the ZEUS offline analysis library PHANTOM.

Particle name	Typical cross section (pb)	Number of events expected in 1992 ZEUS data ($\sim 30nb^{-1}$)
Leptoquark	~ 1000	~ 30
Excited electron	~ 100	~ 3
Excited neutrino	~ 10	~ 0.3
Mirror electron	~ 0.1	~ 0.003
Mirror neutrino	~ 0.3	~ 0.01
Majorana neutrino	~ 0.1	~ 0.003

Table 2.1: Detection possibility of exotic particles at HERA.

Name	T_3	Q	*S-Channel*	*Coupling*
Fermion number = 2				
S_0	0	$-1/3$	$e_L^- u_L \to e_L^- u_L$	g_L
	0	$-1/3$	$e_R^- u_R \to e_R^- u_R$	g_R
	0	$-1/3$	$e_L^- u_L \to \nu_e d_L$	$-g_L$
$\tilde{S}_0$	0	$-4/3$	$e_R^- \bar{d}_R \to e_R^- \bar{d}_R$	g_R
S_1	$+1$	$+2/3$	$\nu_e u_L \to \nu_e u_L$	$\sqrt{2}g_L$
	0	$-1/3$	$e_L^- u_L \to e_L^- u_L,\ \nu_e d_L$	$-g_L$
	-1	$-4/3$	$e_L^- \bar{d}_L \to e_L^- \bar{d}_L$	$-\sqrt{2}g_L$
$V_{1/2}$	$+1/2$	$-1/3$	$e_R^- u_L \to e_R^- u_L$	g_R
	$-1/2$	$-4/3$	$e_L^- \bar{d}_R \to e_L^- \bar{d}_R$	g_L
	$-1/2$	$-4/3$	$e_R^- \bar{d}_L \to e_R^- \bar{d}_L$	g_R
$\tilde{V}_{1/2}$	$+1/2$	$+2/3$	$\nu_e u_R \to \nu_e u_R$	g_L
	$-1/2$	$-1/3$	$e_L^- u_R \to e_L^- u_R$	g_L
Fermion number = 0				
V_0	0	$-2/3$	$e_L^- \bar{d}_R \to e_L^- \bar{d}_R,\ \nu_e \bar{u}_R$	g_L
	0	$-2/3$	$e_R^- \bar{d}_L \to e_R^- \bar{d}_L$	g_R
$\tilde{V}_0$	0	$-5/3$	$e_R^- \bar{u}_L \to e_R^- \bar{u}_L$	g_R
V_1	$+1$	$+1/3$	$\nu_e \bar{d}_R \to \nu_e \bar{d}_R$	$\sqrt{2}g_L$
	0	$-2/3$	$e_L^- \bar{d}_R \to e_L^- \bar{d}_R$	$-g_L$
	0	$-2/3$	$e_L^- \bar{d}_R \to \nu_e \bar{u}_R$	g_L
	-1	$-5/3$	$e_L^- \bar{u}_R \to e_L^- \bar{u}_R$	$\sqrt{2}g_L$
$S_{1/2}$	$+1/2$	$-2/3$	$e_R^- \bar{d}_R \to e_R^- \bar{d}_R$	$-g_R$
	$-1/2$	$-5/3$	$e_L^- \bar{u}_L \to e_L^- \bar{u}_L$	g_L
	$-1/2$	$-5/3$	$e_R^- \bar{u}_R \to e_R^- \bar{u}_R$	g_R
$\tilde{S}_{1/2}$	$+1/2$	$+1/3$	$\nu_e \bar{d}_L \to \nu_e \bar{d}_L$	g_L
	$-1/2$	$-2/3$	$e_L^- \bar{d}_L \to e_L^- \bar{d}_L$	g_L

Table 2.2: Classification of LQ. S and V denote scalar and vector LQ, respectively. The subscript shows weak isospin and T_3 is its third component. Q is electric charge. Production and decay channels are also listed with coupling constants (g_L and g_R denote left-handed and right-handed couplings, respectively).

LQ type	*g_L only*	*g_R only*	*Both couplings*
S_0	67 [UA2], 44.2 [OPAL] ($1.7 g_L \times 10^3$ [$\beta - decay$])	67 [UA2], 44.2 [OPAL]	67 [UA2], 44.2 [OPAL] ($8.8\sqrt{g_L g_R} \times 10^3$ [$\pi^+ \to e^+ \nu$])
$\tilde{S}_0$	–	74 [UA2], 45.5 [OPAL]	–
S_1	67 [UA2], 44.2 [OPAL] ($1.7 g_L \times 10^3$)	–	–
$V_{1/2}$	No limit	No limit	(125×10^3 [$\pi^+ \to e^+ \nu$])
$\tilde{V}_{1/2}$	No limit	–	–
$S_{1/2}$	67 [UA2], 45.1 [OPAL]	67 [UA2], 45.1 [OPAL]	67 [UA2], 45.1 [OPAL] ($8.8\sqrt{g_L g_R} \times 10^3$)
$\tilde{S}_{1/2}$	67[UA2], 45.7[OPAL]	–	–
V_0	($1.7 g_L \times 10^3$)	No limit	(125×10^3)
V_1	($1.7 g_L \times 10^3$)	–	–

Table 2.3: Present mass limits (in GeV) of LQ. The mark '–' means that the combination of the LQ type and the coupling is not allowed by spin and charge conservation. Here results from LEP are represented by the OPAL group, but other groups also have given similar results. Results from CDF are still preliminary and are not included above.

Parameter	Proton ring	Electron ring	units
Nominal energy	820	30	GeV
Polarization time	-	28	min.
Bending radius	588	608	m
Magnetic field	4.65	0.165	T
Energy range	300-820	10-33	GeV
Injection energy	40	14	GeV
Circulating current	160	58	mA
Number of particles	1.0×10^{11}	0.38×10^{11}	/bunch
Beam size at crossing σ_x	0.27	0.26	mm
Beam size at crossing σ_y	0.08	0.07	mm
Beam size at crossing σ_z	110	8	mm
RF frequency	52.033/208.13	499.667	MHz
Filling time	20	15	min.
$\sqrt{s}$	314		GeV
Q^2_{max}	98400		GeV^2
Luminosity	1.5×10^{31}		$cm^{-2}s^{-1}$
No. of interaction points	4		-
Circumference	6336		m
Length of straight section	360		m
Number of bunches	210		-
Number of buckets	220		-
Time between crossings	96		ns

Table 3.1: Nominal parameters of HERA.

Parameter	Proton ring	Electron ring	units
Beam energy	820	26.7	GeV
Circulating current	1-2	1-2	mA
Beam size at crossing σ_z	120-500	8	mm
$\sqrt{s}$	296		GeV
Luminosity	$O(10^{28})$		$cm^{-2}s^{-1}$
Number of bunches	10		-

Table 3.2: Conditions of HERA in 1992

material	EMC			HAC		
	thickness (mm)	thickness (X_0)	thickness (λ)	thickness (mm)	thickness (X_0)	thickness (λ)
steel	0.2	0.011	0.0012	0.4	0.023	0.0024
DU	3.3	1.000	0.0305	3.3	1.000	0.0305
steel	0.2	0.011	0.0012	0.4	0.023	0.0024
paper	0.2			0.2		
SCI	2.6	0.006	0.0033	2.6	0.006	0.0033
paper	0.2			0.2		
contingency	0.9			0.9		
sum	7.6	1.028	0.0362	8.0	1.052	0.0386
effective X_0	0.74 cm			0.76 cm		
effective λ	21.0 cm			20.7 cm		
effect. Moliere radius	2.02 cm			2.00 cm		
effect. critical energy	10.6 MeV			12.3 MeV		
effective density	8.7 g/cm^3			8.7 g/cm^3		

Table 3.3: Sizes and structure of EMC and HAC towers.

Parameter	Nominal value	In 1992
Position resolution	100 - 120 μm (θ dependent)	-
Z-resolution (stereo)	1.2 mm	-
Z-resolution (timing)	3 cm	$\sim$ 4 cm
rϕ-resolution	-	$\sim$ 0.9 mm
Two-track resolution	1.6 mm	-
dE/dx resolution	$\sim$ 5 % for e^-	-
Max. drift time	$\sim$ 500 ns	$\sim$ 500 ns
Lorentz angle	45°	39.1°
Momentum resolution at 90°	$\sigma_p/p = (0.2p \oplus 0.3)\%$	-

Table 3.4: Performance of CTD.

Component	Distance of entry face from I.P (m)	Material	Shape/Size
Photon Detector			
Window	92.5	Copper-Beryllium	Circle 50 mm radius 1.5mm thick ($\simeq 0.1X_0$)
Filter	103.15	Carbon	Square ($175 \times 175mm^2$) $2.0X_0$ thick
Čerenkov Counter	104.95	Air at n.t.p Al windows	Circle 100 mm radius active length 1080 mm 2 windows 3 mm thick each ($\simeq 0.067X_0$)
Calorimeter	106.94	Absorber Pb Scintillator (SCSN38)	Square plates ($180 \times 180)mm^2$ Pb 5.7 mm thick SCSN38 2.8 mm thick total depth $22X_0$
Position Detector	$7X_0$ inside calorimeter	Scintillator (NE102)	2 crossed planes of fingers 14 horizontally ($10 \times 10 \times 163)mm^3$ 16 vertically ($10 \times 10 \times 143)mm^3$
Electron Detector			
Window	27.29	Steel	69 mm radius 1.5 thick ($\simeq 0.085X_0$)
Collimator	33.87	Lead	Rectangular window ($200 \times 50 \times 200mm^3$)
Calorimeter	34.68	Absorber Pb Scintillator (SCSN38)	Square plates ($250 \times 250)mm^2$ Pb 5.7 mm thick SCSN38 2.8 mm thick total depth $24X_0$

Table 3.5: Sizes and structure of luminosity monitor detectors.

	z - position along beam (m)	max/min distance of coll. jaw from beam (mm)		thickness (cm)	
		horizontal (H)	vertical (V)	H	V
Collimator					
C1	~ 11.8	10/36 -	- -	~ 12	
C2	~ 8.0	15/36 -	- -	~ 12	
C3	5.35	10/36 10/30	10/30 10/30	15 6	6 6
C4	2.3	27/40 10/28	30 fixed 30 fixed	3.5 3.5	3.5 3.5
C5	-2.8	50/70 10/30	30 fixed 30 fixed	3 3	3 3
Absorber					
A1 A2	-23.5 -23.5	- -	- -	~ 12	

Table 3.6: Collimeters and absorbers against synchrotron radiation. 2 raws for a horizontal collimator correspond to 2 jaws inside and outside the beampipe located asymmetrically, and a vertical collimator consists of an up and a down jaws.

Event type	Rate	Unit
NC ($Q^2 > 100GeV^2$)	0.11	Hz
CC ($Q^2 > 100GeV^2$)	1.3	mHz
Photon-gluon fusion ($u\bar{u}$)	26.0	Hz
Photon-gluon fusion ($c\bar{c}$)	8.58	Hz
Photon-gluon fusion ($b\bar{b}$)	86	mHz
QCD-Compton (u)	1.86	Hz
QCD-Compton (d)	0.34	Hz
QCD-Compton (s)	0.23	Hz
Photoproduction	264.0	Hz

Table 4.1: Expected event rates for various types of interactions under the HERA nominal condition. Photoproduction is based on the vector-meson-dominance model.

Cable number	Component	Cable contents	In 1992	
			Available	Used for decision
(1)	CAL('92)	EMC TIB bits	*	o
(2)	CAL('92)	HAC TIB bits	*	o
(3)	CAL('92)	EMC 2nd TIB bits	*	o
1 - 16	CAL	16 regional info.		
17	CAL	Electronics overflow		
18	CAL	Corrected overflow		
19	CAL	Proton-gas event info.		
20	CAL	Isolated particle		
21	CAL	EMC energy		
22	CAL	BCAL energy, EMC Emiss		
23	CAL	Total Energy, Et		
24	CAL	Energy away from beampipe		
25	CAL	Total Ex, Ey		
26	CAL	Total Emiss		
27	CAL	Cluster info.		
28	CAL	Quiet region		
29	CAL	Jet likelihood		
30	CAL	FCAL energy		
31	CAL	RCAL EMC energy		
32	CAL	RCAL HAC energy		
33	TRK	Quality, Multiplicity		
34 - 37	TRK	Bitmap		
38 - 39	FMU	Bitmap	*	
40	FMU	Readout type		
41	BMU	Bitmap	*	o
42	BAC	Energy	*	
43	BAC	Et	*	
44	BAC	Most energetic cluster		
45	BAC	2nd energetic cluster		
46	BAC	Muon information		
47	VETO	Vetowall hit	*	o
48	LUMI	Energy	*	o
49	LUMI	Event flag	*	o
50	LPS	Hit pattern		
51	BEAMLINE	Energy		
52	C5	Down detector info.	*	o
53	C5	Up detector info.	*	o

Table 4.2: The full list of FLT data sent from local FLT's to GFLT. Available data in 1992 are tagged with *. The data which participated in making the GFLT ACCEPT flag are tagged with o.

CALFLT Setup	Set-1	Set-2	Set-3	Set-4
EMC				
FCAL beampipe	50.0	50.0	50.0	50.0
FCAL inner	20.0	20.0	20.0	20.0
FCAL outer	10.0	10.0	10.0	10.0
RCAL beampipe	10.0	10.0	10.0	10.0
RCAL other	2.5	**1.0**	1.0	1.0
BCAL	2.5	2.5	2.5	**1.0**
2nd EMC				
RCAL beampipe	-	-	**2.5**	2.5
RCAL other	-	-	**0.4**	0.4
HAC				
FCAL beampipe	70.0	70.0	70.0	70.0
FCAL inner	25.0	25.0	25.0	25.0
FCAL outer	10.0	10.0	10.0	10.0
RCAL beampipe	5.0	**2.5**	2.5	2.5
RCAL other	30.0	**1.0**	1.0	1.0
BCAL	1.0	1.0	1.0	1.0

Table 4.3: Threshold settings of CAL FLT in 1992. Threshold values are in GeV. The values with the bold line are modified thresholds from the previous setting.

Trigger mode	Luminosity (nb^{-1})		CAL	GFLT rate	GSLT rej.	TLT rej.	Recorded
	Total	Analyzed	FLT	(Hz)	(%)	(%)	data (Hz)
Day1	0.08	0.05	Set-1	5 - 6	-	-	4 - 5
Day1_with_C5cut	0.4	0.35	Set-1	4 - 7	-	25 - 30	3 - 4
Day1_with_C5_TLTcut	0.7	0.5	Set-1	4 - 7	-	40 - 50	2 - 4
Standard_Jul16	1.0	0.8	Set-1	4 - 7	10 - 14	40 - 50	2 - 3
Standard_Sep19	1.7	1.6	Set-2	8 - 15	8 - 15	30 - 40	5 - 6
Standard_Sep22	0.3	0.0	Set-3	8 - 15	25 - 30	35 - 45	2 - 3
Standard_Sep25	16.2	14.2	Set-3	10 - 15	25 - 30	35 - 45	3 - 5
Standard_Oct09	9.5	7.2	Set-4	14 - 20	38 - 43	26 - 34	4 - 8
Standard_Oct29	2.6	1.9	Set-4	14 - 20	38 - 43	26 - 34	5 - 8

Table 4.4: Summary of ZEUS data taking conditions in 1992. 'GSLT rej.' and 'TLT rej.' are the fraction of the rejected events by GSLT and TLT, respectively. 'Analyzed' luminosity is for the data used in this analysis.

Trigger mode		Day1_with_		Standard_					
	Day1	C5	C5_TLT	Jul16	Sep19	Sep22	Sep25	Oct09	Oct29
CALFLT									
Set-1	o	o	o	o	-	-	-	-	-
Set-2	-	-	-	-	o	-	-	-	-
Set-3	-	-	-	-	-	o	o	-	-
Set-4	-	-	-	-	-	-	-	o	o
GFLT									
DIS trigger									
EMC with C5 cut	-	1	1	1	1	1	1	1	1
FCAL with C5 cut	-	1	1	1	1	1	1	1	1
Photoproduction trigger									
CAL*LUMI_Ee(4)	-	-	-	-	-	-	1	1	1
Miscellaneous									
EMC	1	1/4	1/4	1/4	1/16	1/16	1/16	1/16	1/16
FCAL	1	1/4	1/4	1/4	1/16	1/16	1/16	1/16	1/16
CAL_any*BMU	1/4	1/8	1/8	1/2	1/2	1/2	1/2	1/2	1/2
LUMI_Ee(4)	-	-	-	-	2^{-12}	2^{-13}	2^{-14}	2^{-14}	-
LUMI_Eg(5)	-	-	-	-	2^{-12}	2^{-13}	2^{-14}	2^{-14}	-
LUMI_Eg(5)*Ee(4)	-	-	-	-	-	-	-	-	2^{-12}
BCAL*VETOWALL	-	-	-	0 - 1; depends on beam condition.					
GSLT									
Cosmic rejection	-	-	-	-	o	o	o	o	o
CAL energy cut	-	-	-	-	-	-	-	o	o
TLT									
Spark rejection	-	o	o	o	o	o	o	o	o
Timing rejection	-	-	o	o	o	o	o	o	o

Table 4.5: Trigger modes in 1992. Numbers for GFLT subtriggers are prescale factors. LUMI_Ee(4) means that the energy in LUMI EDET is greater than 4 GeV. Similar definition is valid on LUMI_Eg (for LUMI GDET).

Process	Mass (GeV/c^2)	CAL FLT acceptance (%)		
		Set-1	Set-2 and Set-3	Set-4
Scalar LQ $\rightarrow eq$	50	98.6	98.3	99.6
	75	99.5	98.9	99.7
	100	99.7	99.7	99.9
	125	99.9	99.9	100.0
	150	100.0	100.0	100.0
	175	100.0	100.0	100.0
	200	99.9	100.0	100.0
	225	99.8	99.9	99.9
Vector LQ $\rightarrow eq$	40	97.6	97.7	99.4
	75	98.2	97.8	98.5
	100	99.4	99.0	99.4
	125	99.4	99.7	99.7
	150	99.9	99.9	99.9
	175	99.3	99.4	99.7
	200	99.5	99.9	99.9
	225	100.0	100.0	100.0
Scalar LQ $\rightarrow \nu q$	50	75.9	79.0	93.4
	75	83.1	84.1	91.7
	100	91.5	91.7	95.6
	125	96.2	97.2	98.7
	150	96.9	97.2	98.9
	175	98.4	98.6	99.6
	200	98.9	98.9	99.5
	225	98.8	98.2	99.4
Vector LQ $\rightarrow \nu q$	40	55.6	56.0	81.6
	75	70.2	68.6	75.0
	100	90.4	90.0	92.4
	125	95.4	99.7	99.7
	150	97.4	99.9	99.9
	175	98.2	99.4	99.7
	200	99.2	99.9	99.9
	225	98.6	100.0	100.0
NC ($Q^2 > 2GeV^2$)	—	55.2	58.1	58.1
NC ($Q^2 > 30GeV^2$)	—	97.0	98.7	99.4
CC ($Q^2 > 10GeV^2$)	—	78.2	81.1	89.0
Integrated Luminosity (nb^{-1})	—	1.7	15.8	9.1

Table 4.6: The Monte Carlo study on trigger efficiencies of the CAL FLT trigger for LQ and DIS events.

Event type	Efficiency (%)	Contamination (Single π^-) (%)	Reconstructed - Generated		
			Energy (GeV)	θ (deg.)	ϕ (deg.)
Single e					
30GeV in FCAL	98.8	3.4	-0.6 ± 2.0	0.3 ± 0.2	0.7 ± 0.4
80GeV in FCAL	99.2	1.8	-0.9 ± 3.5	0.3 ± 0.2	0.2 ± 0.5
200GeV in FCAL	99.4	1.0	-1.1 ± 5.2	0.3 ± 0.2	0.1 ± 0.4
30GeV in BCAL	97.3	3.1	-1.3 ± 2.1	0.1 ± 0.2	0.6 ± 0.3
80GeV in BCAL	97.8	1.9	-2.3 ± 4.5	0.0 ± 0.2	0.3 ± 0.3
150GeV in BCAL	96.7	1.8	-2.3 ± 6.4	0.0 ± 0.2	0.2 ± 0.3
15GeV in RCAL	98.9	6.8	-0.2 ± 0.9	0.1 ± 0.4	1.2 ± 0.8
30GeV in RCAL	99.5	6.6	-0.3 ± 1.6	0.1 ± 0.4	0.6 ± 0.7
NC ($Q^2 > 2GeV^2$)	36.3	-	0.1 ± 2.2	-0.1 ± 1.8	0.8 ± 1.3
LQ (S_0 ; $M_{LQ} = 200$GeV)	90.0	-	-3.7 ± 5.8	0.1 ± 3.4	0.1 ± 0.5

Table 6.1: Performance of the electron finder. The errors are root mean squares.

Selection	NC ($LQ \to e + X$)	CC ($LQ \to \nu + X$)
Preselection	25818	18777
Collision bunch selection	24928	16918
$E^e_{LUMI} < 5\ GeV$	21511	16800
Final timing cut	17548	7028
RCAL energy $< 37\ GeV$	17398	6890
Electron energy and position cut	3302	—
$y_e < 0.96$	3272	—
CTD vertex: $\|Z\| < 75cm$	—	1200
Hereafter all variables are with Z-vertex correction.		
$E - P_z > 30\ GeV$	3126	—
$E_{FCAL} + E_{BCAL} > 5\ GeV$	2843	—
P_t conservation	2770	—
cone cut: $P_t > 10\ GeV$	—	38
$y_{JB} > 0.05$	1566	—
Tight electron position cut	719	—
NC samples	719	—
$y_{JB} > 0.1$ or $P_t^{elec} > 20\ GeV$	515	—
$x_{DA} > 0.001$	346	—
$x_{JB} > 0.01$	—	16
CC events with eye scan	—	2
LQ search samples	346	2

Table 6.2: Selection criteria for NC and CC samples, and the final LQ search samples.

Variable	Event 1	Event 2	Event 3
x_{DA}	0.19	0.16	0.10
y_{DA}	0.21	0.065	0.32
Q^2_{DA} (GeV^2)	3.5×10^3	9.0×10^2	2.9×10^3
Electron Pt (GeV)	47	26	39

Table 6.3: Kinematical variables of neutral current events with $x_{DA} \geq 0.1$.

Event type	$M_{LQ}(GeV)$	Selection for	
		NC sample (%)	LQ search sample (%)
Scalar LQ with $g_L = 0$ or $g_R = 0$	50	89.9	84.1
	75	88.7	85.1
	100	88.5	87.8
	125	90.2	89.4
	150	90.4	90.3
	175	88.8	88.7
	200	87.9	87.9
	225	85.1	85.0
Vector LQ with $g_L = 0$ or $g_R = 0$	40	81.6	68.7
	75	86.1	75.7
	100	88.3	85.2
	125	86.9	85.8
	150	90.4	89.9
	175	87.7	86.6
	200	88.2	88.0
	225	89.0	89.0
NC $(Q^2 > 2GeV^2)$	—	5.15	2.50
NC $(Q^2 > 50GeV^2)$	—	45.6	30.5

Table 6.4: Selection efficiency for NC samples, and the final LQ search samples.

Variable	Event A	Event B
$p_T(\ GeV)$	20	82
x_{JB}	0.035	0.32
y_{JB}	0.15	0.41
Q^2_{JB} (GeV^2)	4.7×10^2	1.1×10^4

Table 6.5: Kinematical variables of charged current event candidates.

Event type	$M_{LQ}(GeV)$	CC sample (%)
Scalar LQ with $g_L = 0$ or $g_R = 0$	50	67.5
	75	79.0
	100	85.6
	125	87.0
	150	85.9
	175	81.3
	200	74.8
	225	73.0
Vector LQ with $g_L = 0$ or $g_R = 0$	40	45.2
	75	66.0
	100	81.0
	125	76.2
	150	65.2
	175	51.4
	200	54.7
	225	48.5
CC $(Q^2 > 10GeV^2)$	—	55.5

Table 6.6: Selection efficiency for CC samples.

Scalar Leptoquark									
M_{LQ} (GeV)		50	75	100	125	150	175	200	225
S_0	L	0.084	0.085	0.110	0.168	0.197	0.284	0.455	0.843
	R	0.074	0.073	0.096	0.147	0.155	0.222	0.341	0.619
$\tilde{S}_0$	L	—	—	—	—	—	—	—	—
	R	0.086	0.090	0.128	0.212	0.245	0.397	0.765	
S_1	L	0.051	0.056	0.076	0.121	0.147	0.223	0.374	0.736
	R	—	—	—	—	—	—	—	—
$S_{1/2}$	L	0.114	0.148	0.267	0.573				
	R	0.057	0.074	0.133	0.286	0.436			
$\tilde{S}_{1/2}$	L	0.114	0.148	0.267	0.573				
	R	—	—	—	—	—	—	—	—
Possible increase from systematic error (%)		5	3	4	4	4	4	5	6
Vector Leptoquark									
M_{LQ} (GeV)		40	75	100	125	150	175	200	225
V_0	L	0.066	0.156	0.217	0.484	0.919			
	R	0.057	0.137	0.190	0.418	0.741			
$\tilde{V}_0$	L	—	—	—	—	—	—	—	—
	R	0.057	0.137	0.190	0.419	0.744			
V_1	L	0.045	0.109	0.154	0.341	0.634	1.239		
	R	—	—	—	—	—	—	—	—
$V_{1/2}$	L	0.046	0.084	0.092	0.157	0.213	0.303	0.509	1.033
	R	0.031	0.053	0.055	0.089	0.114	0.148	0.221	0.380
$\tilde{V}_{1/2}$	L	0.041	0.068	0.069	0.109	0.134	0.169	0.245	0.408
	R	—	—	—	—	—	—	—	—
Possible increase from systematic error (%)		6	4	3	4	4	5	5	6

Table 6.7: Limits for left-handed or right-handed couplings for various masses and types of LQ at 95% CL.

LQ Type	Q	F	T	Left-handed			Right-handed		
				Quark	$b(e^-q)$	Limit	Quark	$b(e^-q)$	Limit
S_0	$-\frac{1}{3}$	2	0	u	$\frac{1}{2}$	180	u	1	196
$\tilde{S}_0$	$-\frac{4}{3}$	2	0	—	—	—	d	1	163
S_1	$-\frac{1}{3}, -\frac{4}{3}$	2	1	u, d	$\frac{1}{2}$,1	192	—	—	—
$S_{1/2}$	$-\frac{2}{3}, -\frac{5}{3}$	0	$\frac{1}{2}$	$\bar{u}$	1	105	$\bar{u}, \bar{d}$	1	129
$\tilde{S}_{1/2}$	$-\frac{2}{3}$	0	$\frac{1}{2}$	$\bar{d}$	1	105	—	—	—
V_0	$-\frac{2}{3}$	0	0	$\bar{d}$	$\frac{1}{2}$	111	$\bar{d}$	1	115
$\tilde{V}_0$	$-\frac{5}{3}$	0	0	—	—	—	$\bar{u}$	1	115
V_1	$-\frac{2}{3}, -\frac{5}{3}$	0	1	$\bar{d}, \bar{u}$	$\frac{1}{2}$,1	122	—	—	—
$V_{1/2}$	$-\frac{1}{3}, -\frac{4}{3}$	2	$\frac{1}{2}$	d	1	176	d, u	1	216
$\tilde{V}_{1/2}$	$-\frac{1}{3}$	2	$\frac{1}{2}$	u	1	206	—	—	—

Table 6.8: Mass Limits (in GeV) on scalar and vector LQ for $g = 0.31$ (electroweak coupling) at 95% CL. Q, F, T, $b(e^-q)$ are electric charge, fermion number, weak isospin, and branching ratio to an electron-quark pair, respectively.

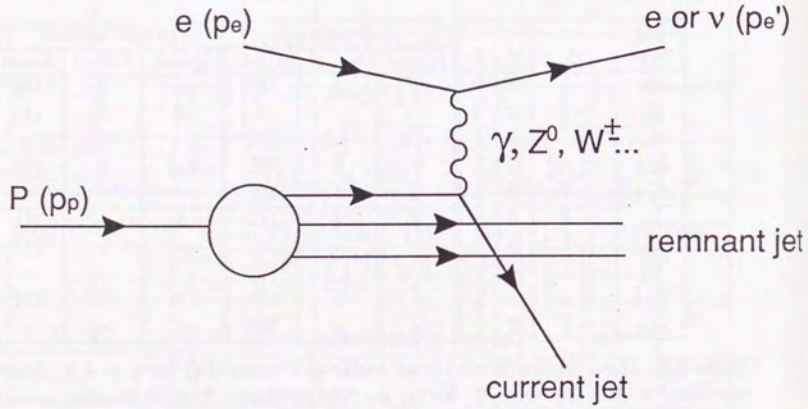

Figure 2.1: The deep inelastic process $e + p \rightarrow l + X$.

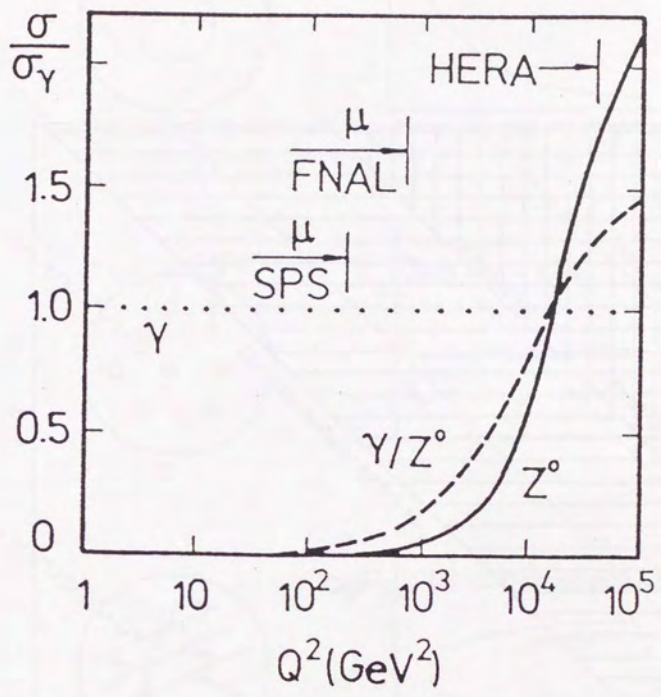

Figure 2.2: Relative size of the NC cross sections from γ, Z^0 and their interference as a function of the momentum transfer. The values are normalized to the pure γ cross section.

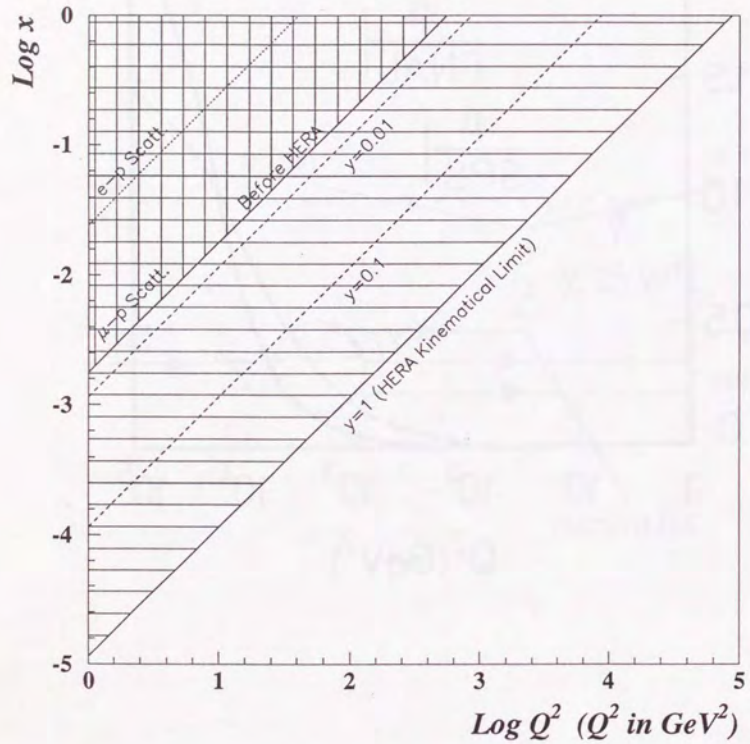

Figure 2.3: Accessible kinematical region at HERA.

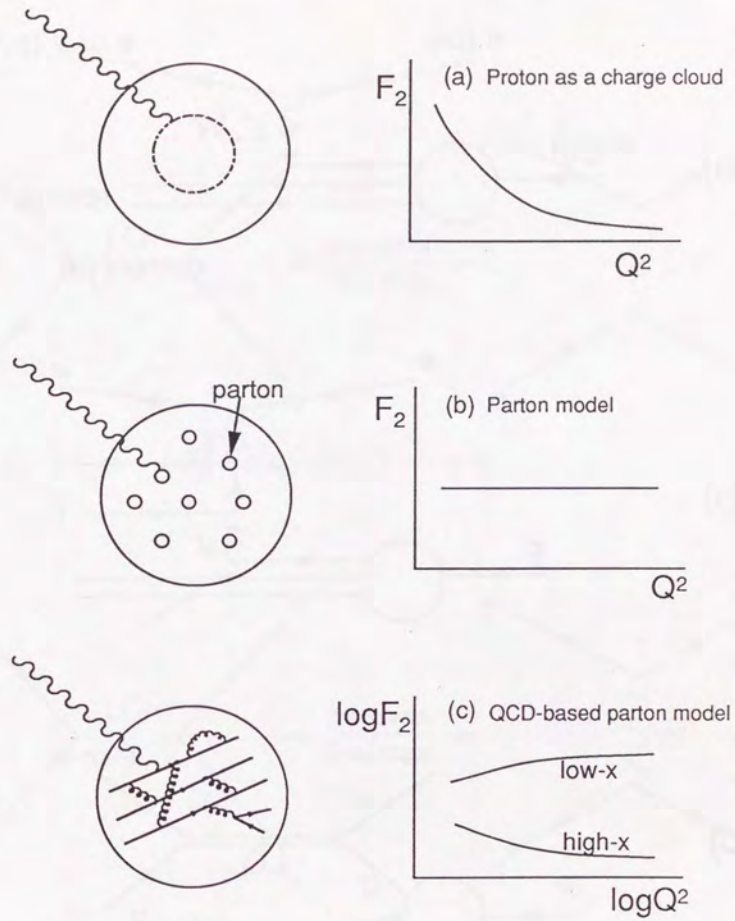

Figure 2.4: The models of the internal structure of a proton and resulting Q^2-dependence of the structure function (F_2). (a) If a proton is regarded as a charge cloud, F_2 falls off as Q^2 increases. (b) F_2 does not depend on Q^2 according to a naive parton model. (c) A small Q^2 dependence is seen according to the QCD-based parton model.

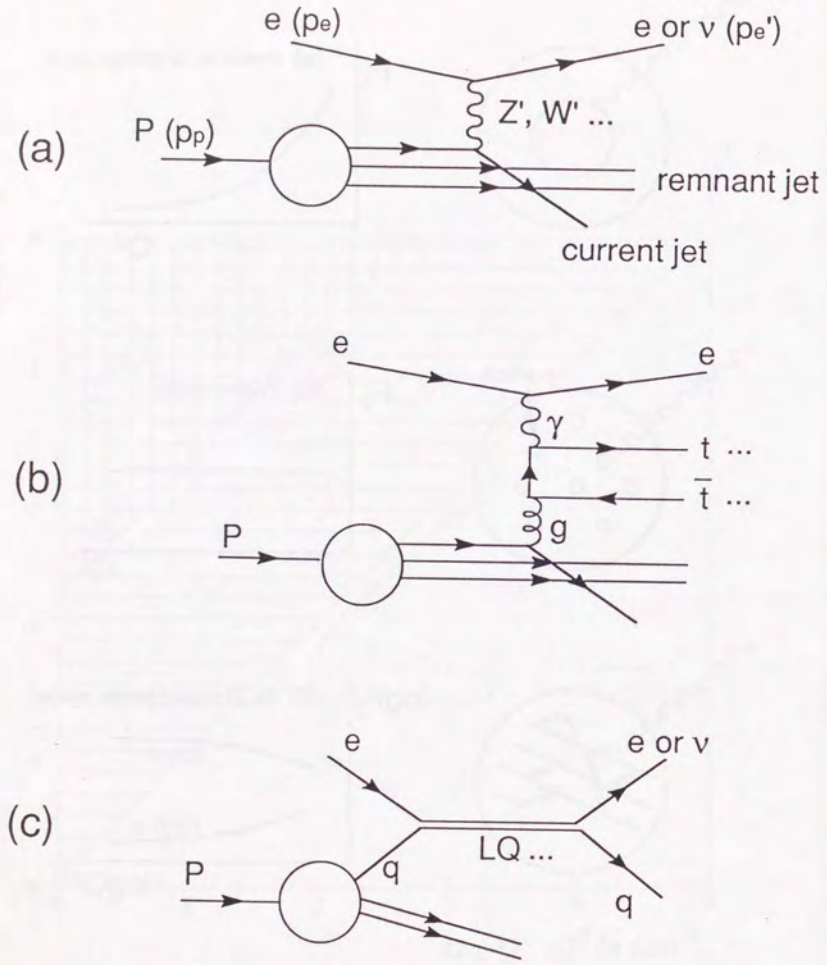

Figure 2.5: Types of exotic physics at HERA. (a) Virtual exchange of a new particle. (b) Pair production of new particles via boson-gluon fusion. (c) Direct production of a new particle associated with the initial electron.

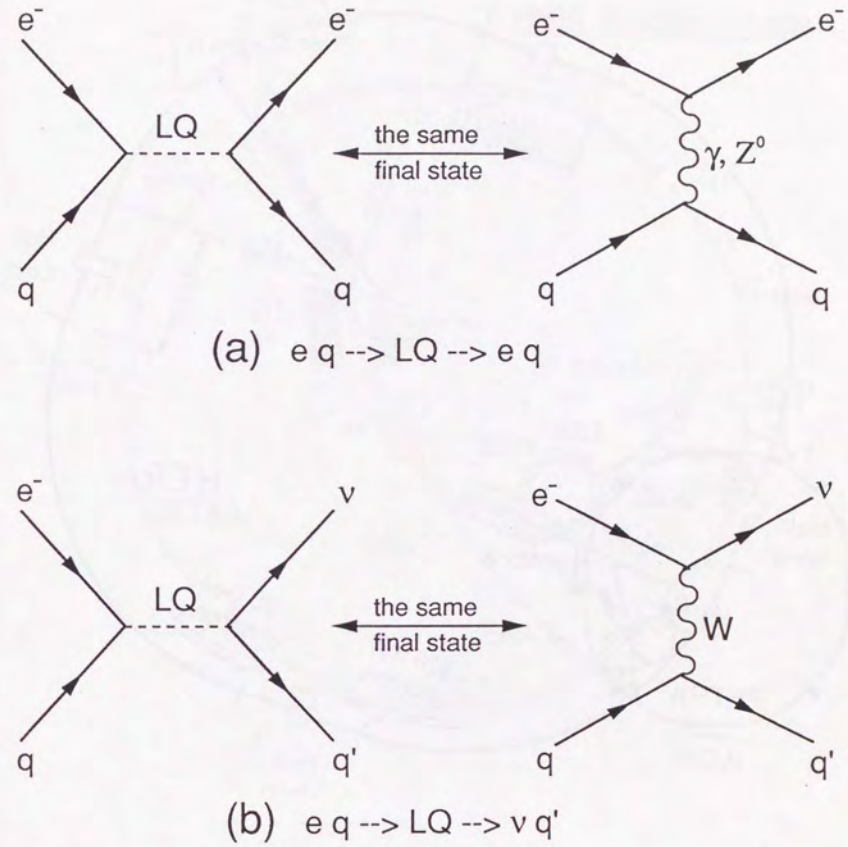

Figure 2.6: Feynman diagrams for LQ production in e-p collision.

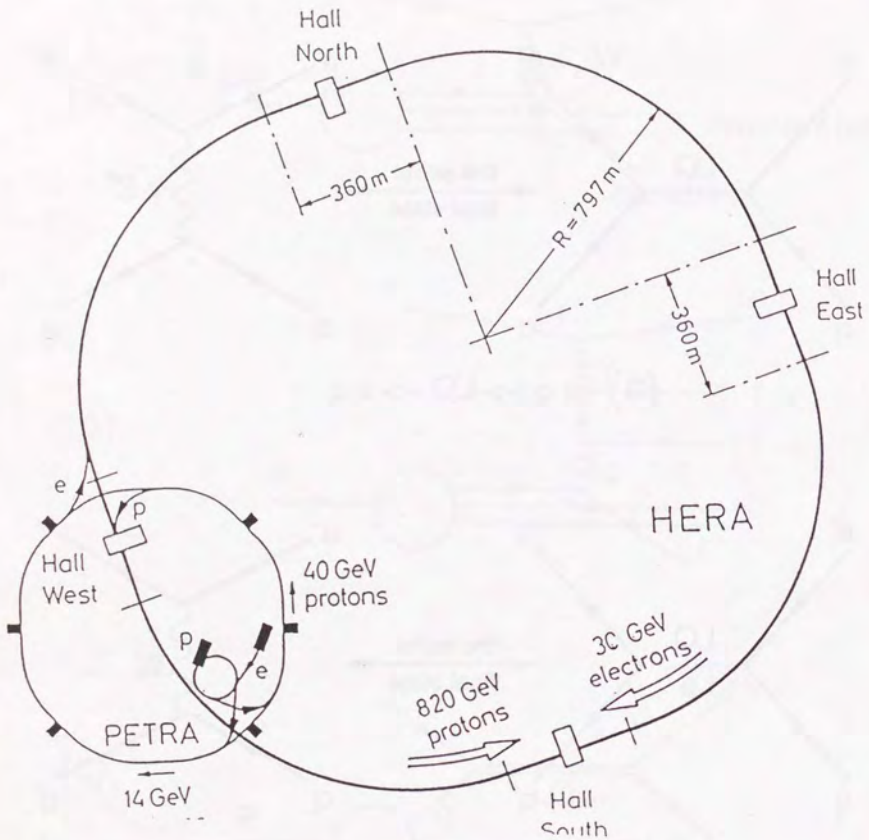

Figure 3.1: A schematic overview of HERA.

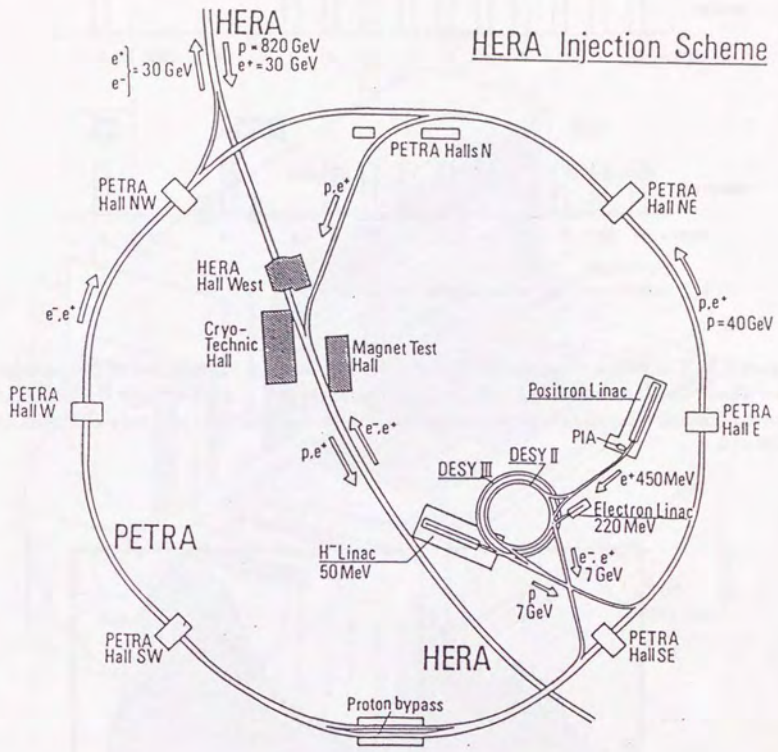

Figure 3.2: Accelerators used for HERA injection.

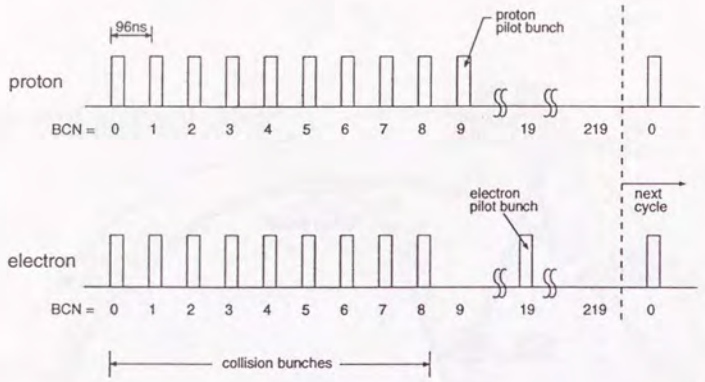

Figure 3.3: The bunch structure of HERA in 1992. Only 10 bunches out of 220 bunches were filled. The bunch crossing number (BCN) from 0 to 8 contained both electrons and protons (collision bunches). Only protons were filled on BCN=9, and only electrons on BCN=19.

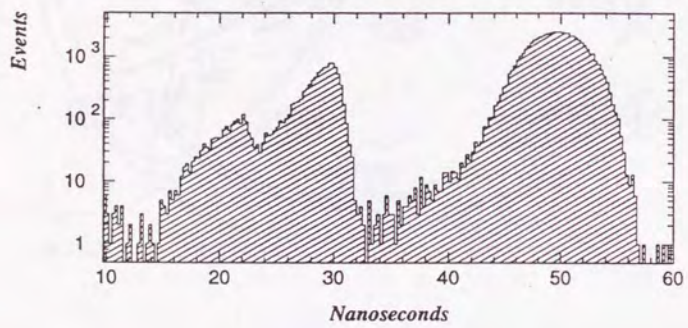

Figure 3.4: Time distribution of proton and electron bunches measured with the C5 veto counter. The right peak at $\sim$ 50ns is due to the proton beam, and the left peak at $\sim$ 30ns is due to the electron beam. A small secondary dip is seen in the electron distribution.

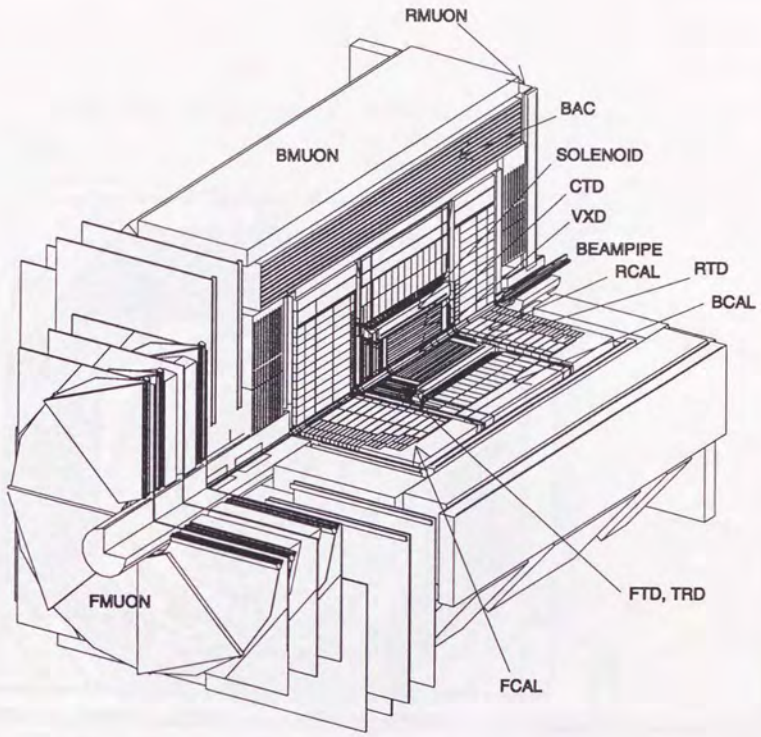

Figure 3.5: ZEUS detector

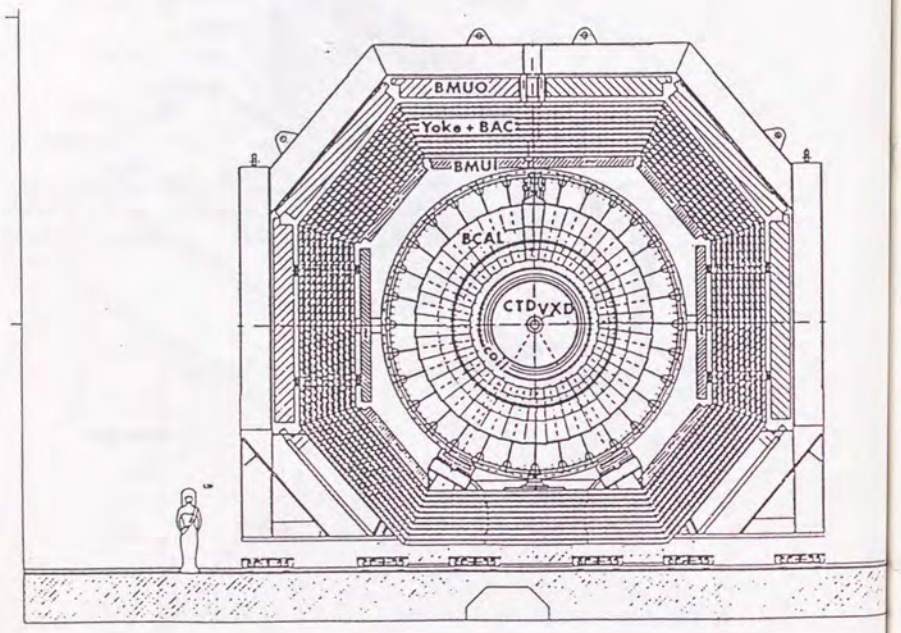

Figure 3.6: Cross section of the ZEUS detector in the azimuthal plane.

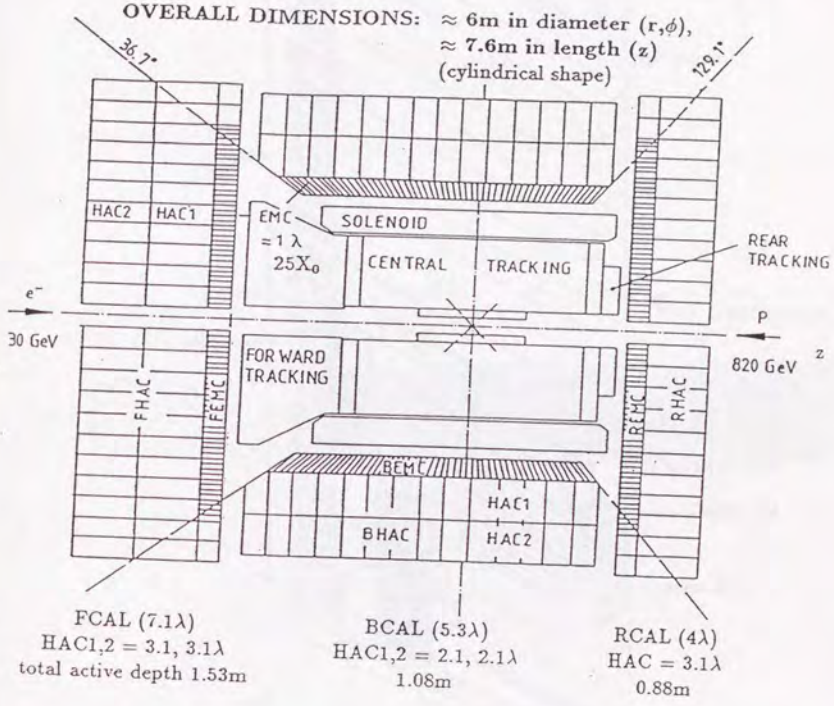

Figure 3.7: Layout of the ZEUS Uranium Scintillator Calorimeter; F/B/RCAL = Forward/Barrel/Rear CALorimeters, EMC and HAC = ElectroMagnetic and HAdronic Calorimeters.

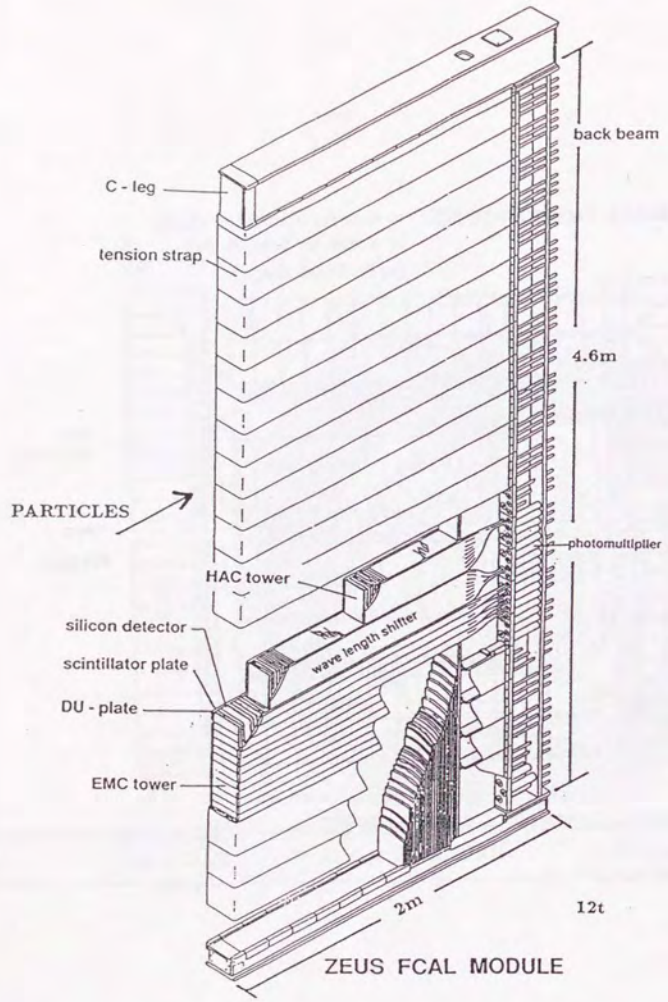

Figure 3.8: Internal structure of an FCAL module.

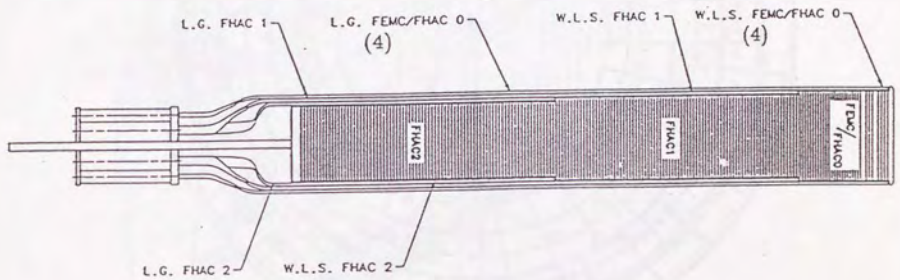

Figure 3.9: A supertower of the ZEUS calorimeter.

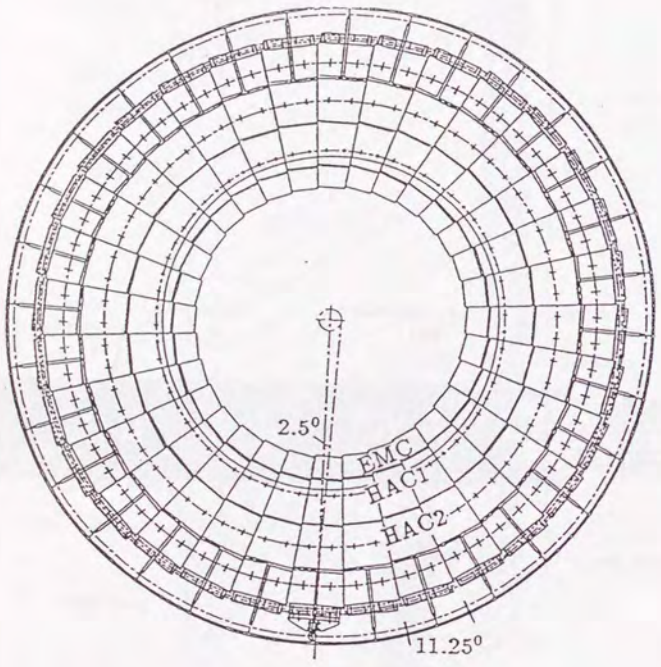

Figure 3.10: The cross section of BCAL in the azimuthal plane.

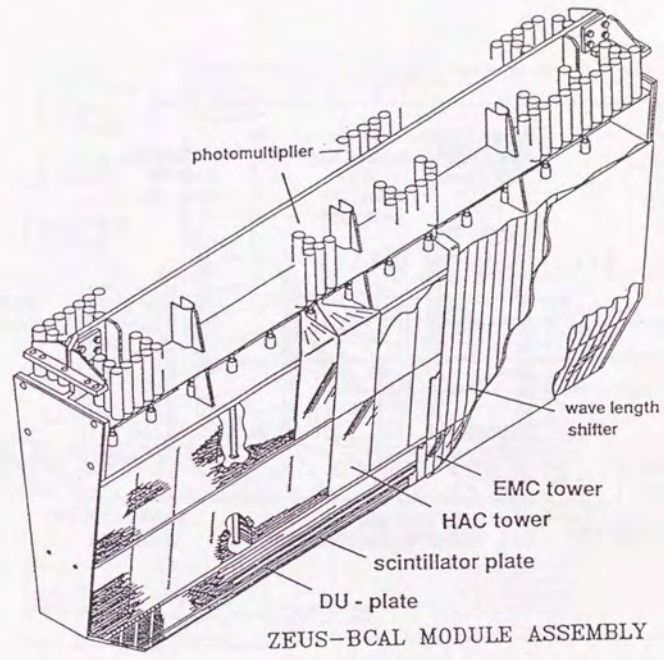

Figure 3.11: Internal structure of a BCAL module.

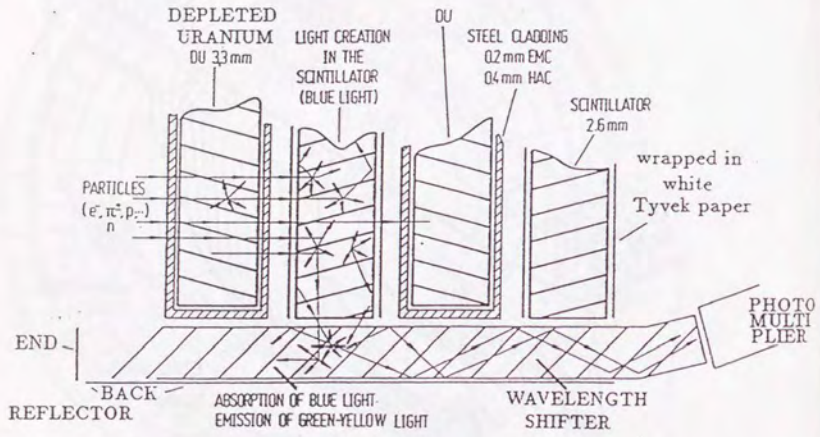

Figure 3.12: Optical readout scheme of the scintillator light with wavelength shifters.

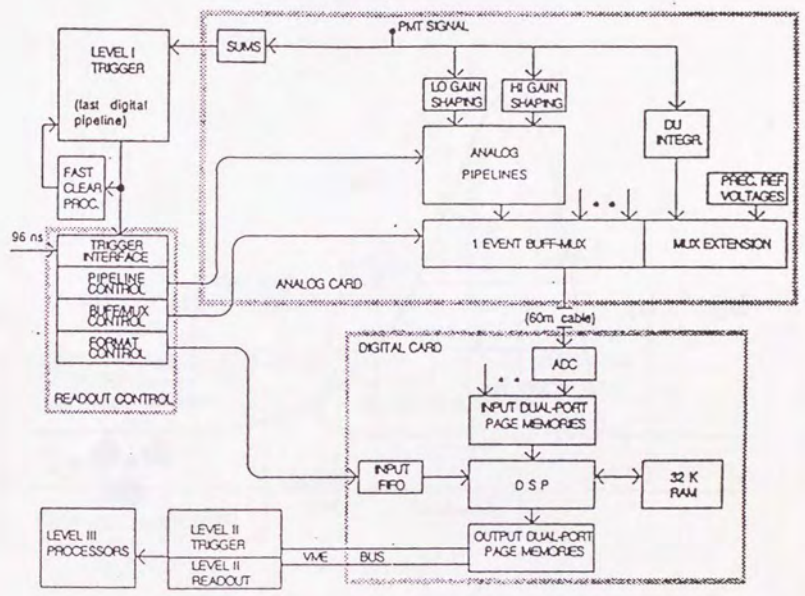

Figure 3.13: Block diagram of the CAL readout electronics.

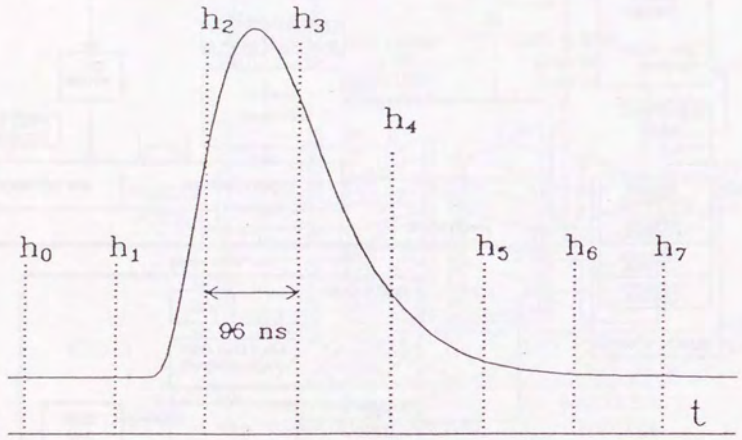

Figure 3.14: A typical signal of CAL at the shaper output. The pulse hight is sampled every 96 ns as shown with h_0 to h_7.

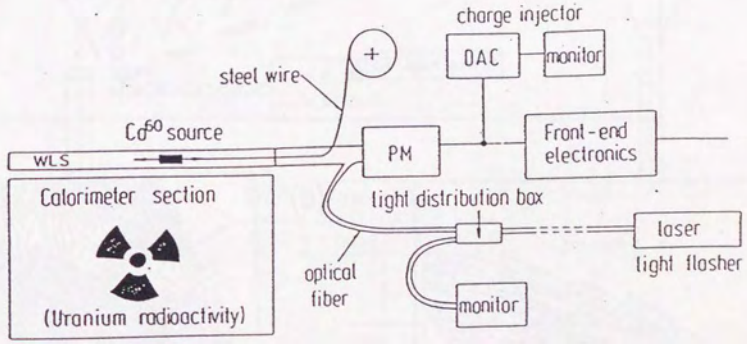

Figure 3.15: Schematic drawing of the light flasher system of CAL.

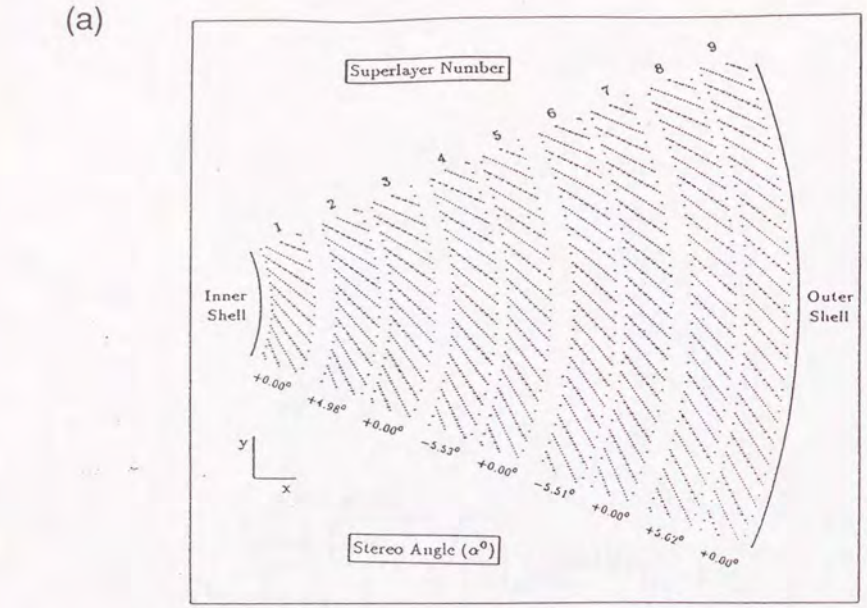

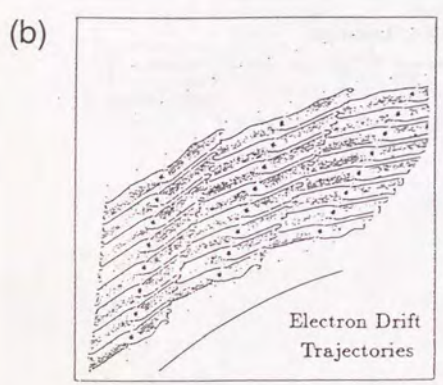

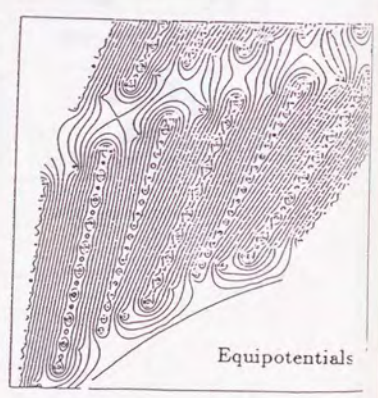

Figure 3.16: (a) Layout of an octant of the CTD at the chamber end-plate. (b) Electron drift trajectories in a CTD cell. (c) Equipotentials in a CTD cell.

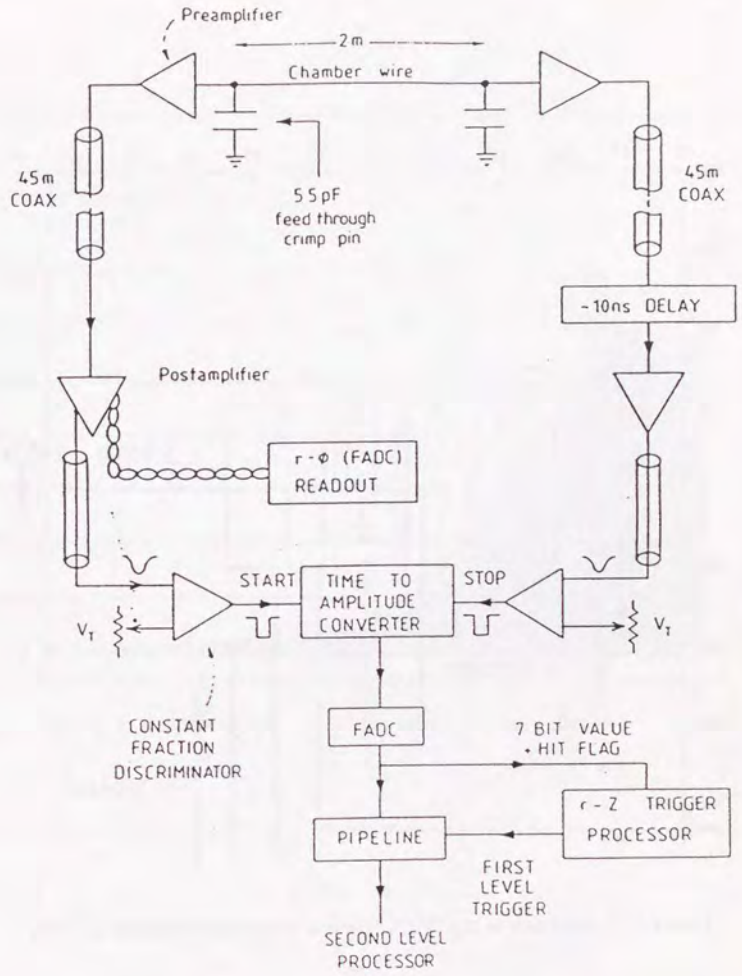

Figure 3.17: Block diagram of the CTD electronics for the time difference measurement.

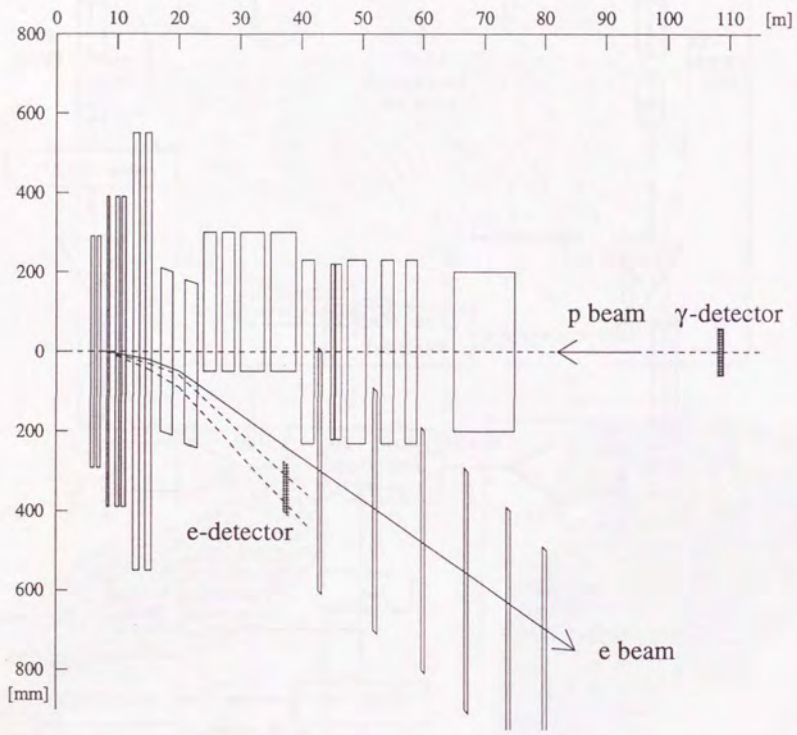

Figure 3.18: Overview of the ZEUS luminosity monitoring system (LUMI).

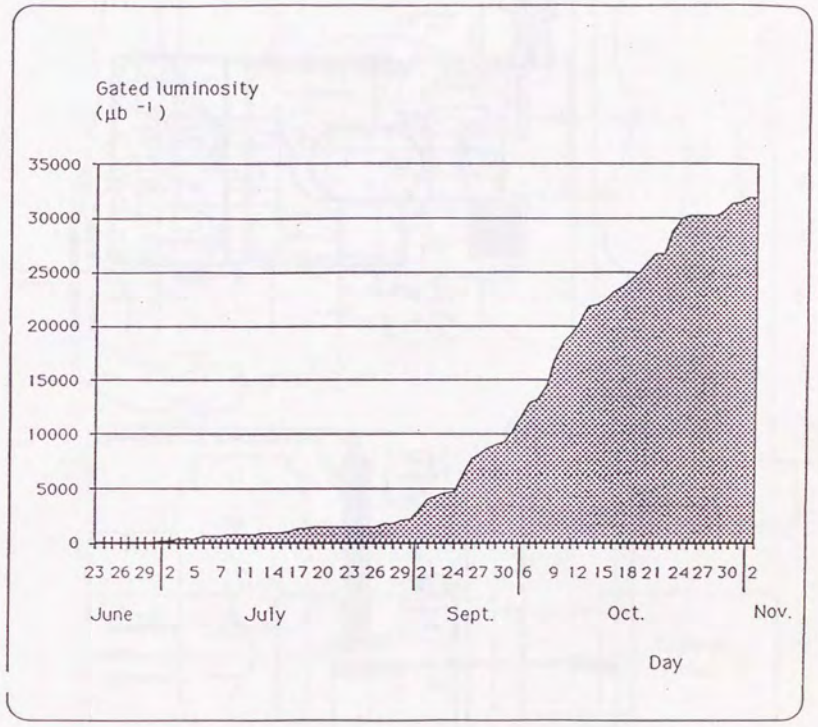

Figure 3.19: ZEUS integrated luminosity in 1992. $32.6nb^{-1}$ was recorded in total. $26.6nb^{-1}$ out of the total luminosity is used in this thesis.

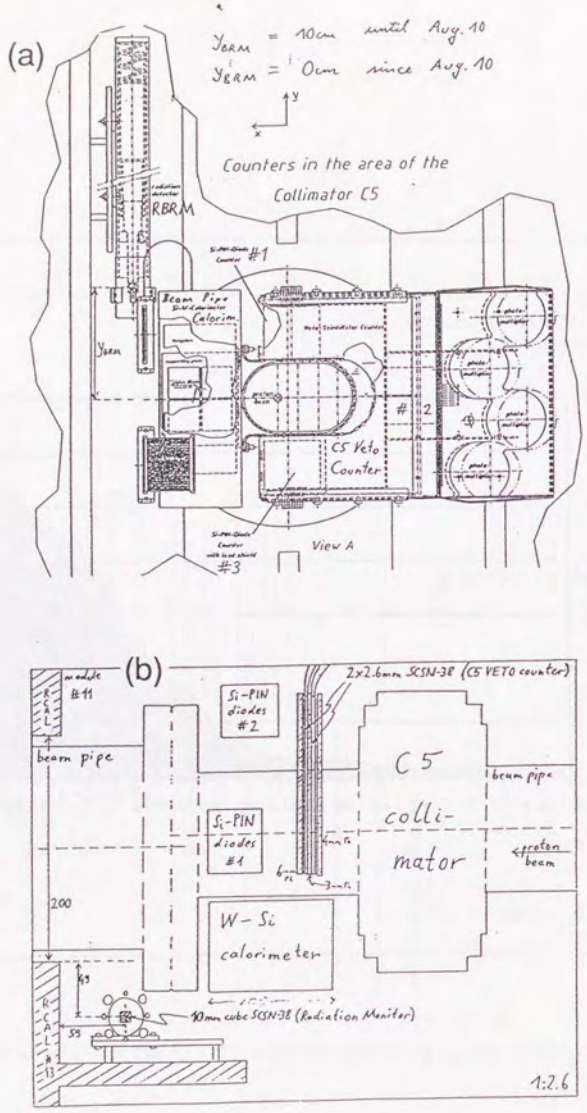

Figure 3.20: C5 collimator, veto counter and beampipe calorimeter. (a) in x-y plane. (b) top view.

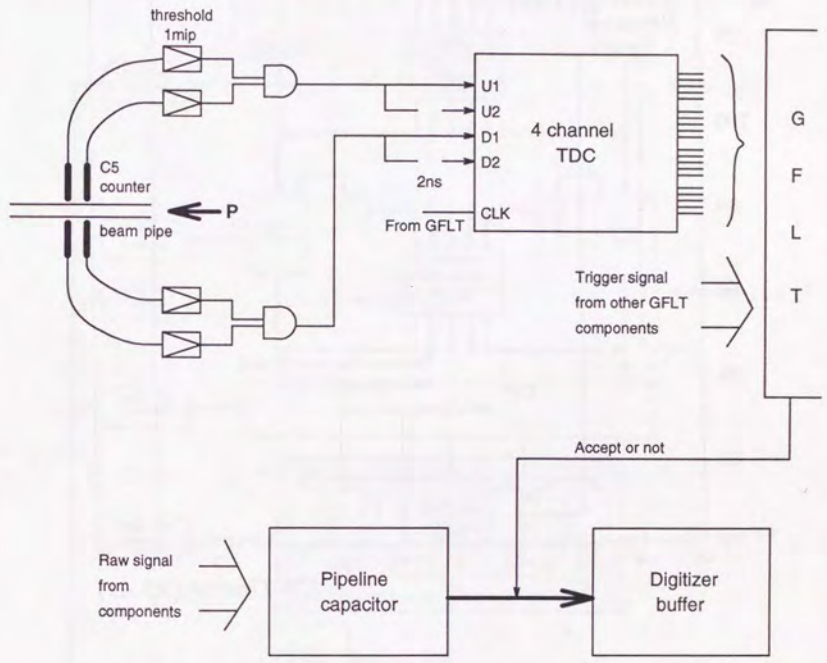

Figure 3.21: Trigger signals from C5 veto counter to GFLT.

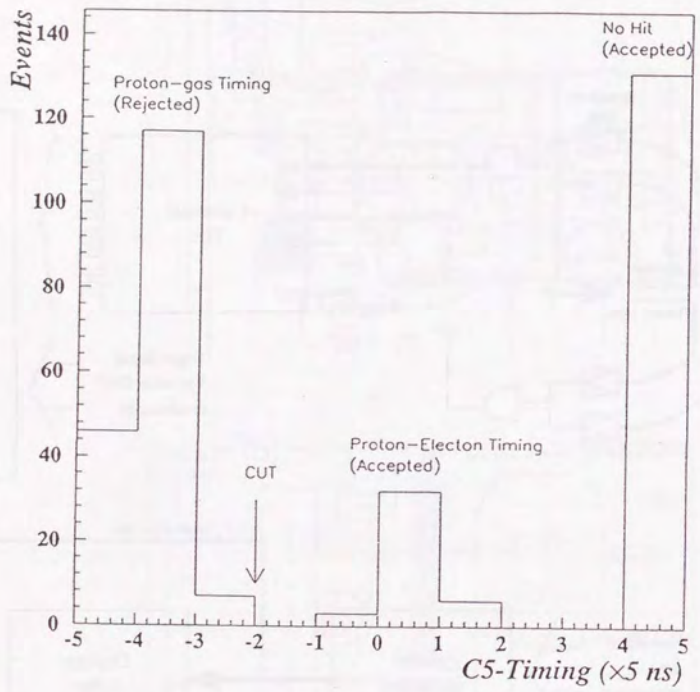

Figure 3.22: Typical timing distribution of the C5 veto counter on a collision bunch.

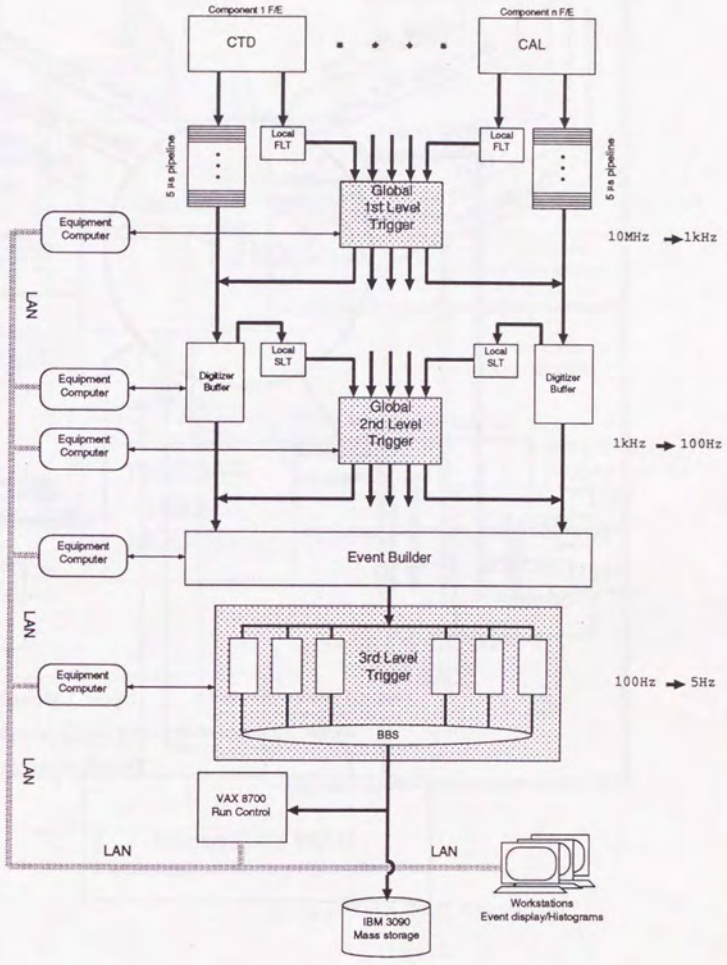

Figure 4.1: A schematic of the ZEUS data acquisition system.

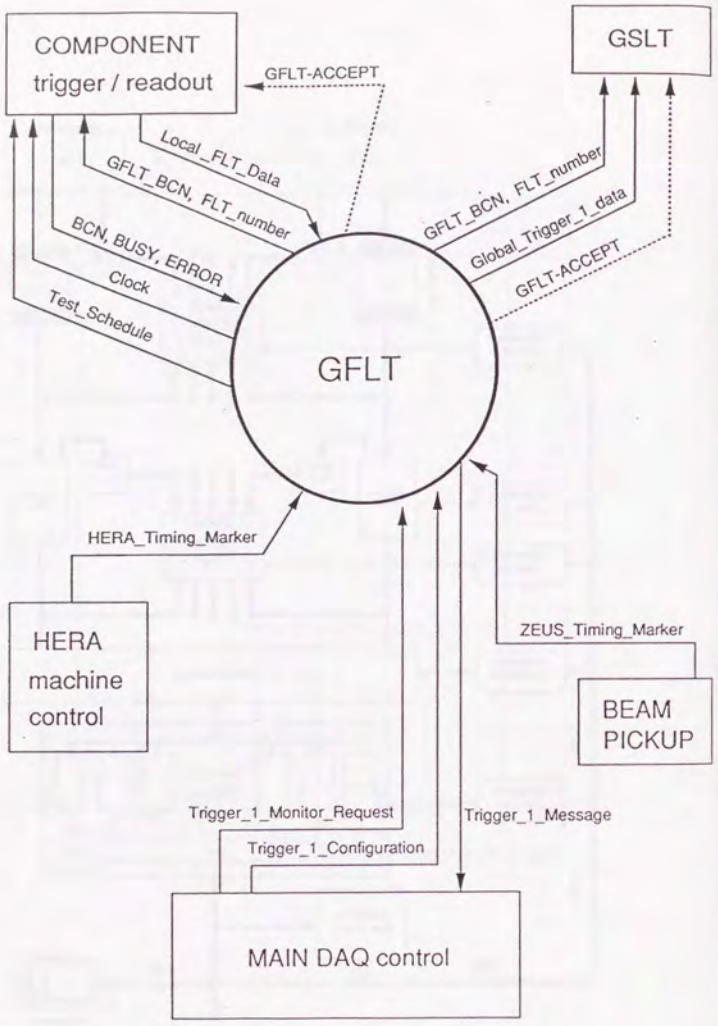

Figure 4.2: Transmitted data between GFLT and other components.

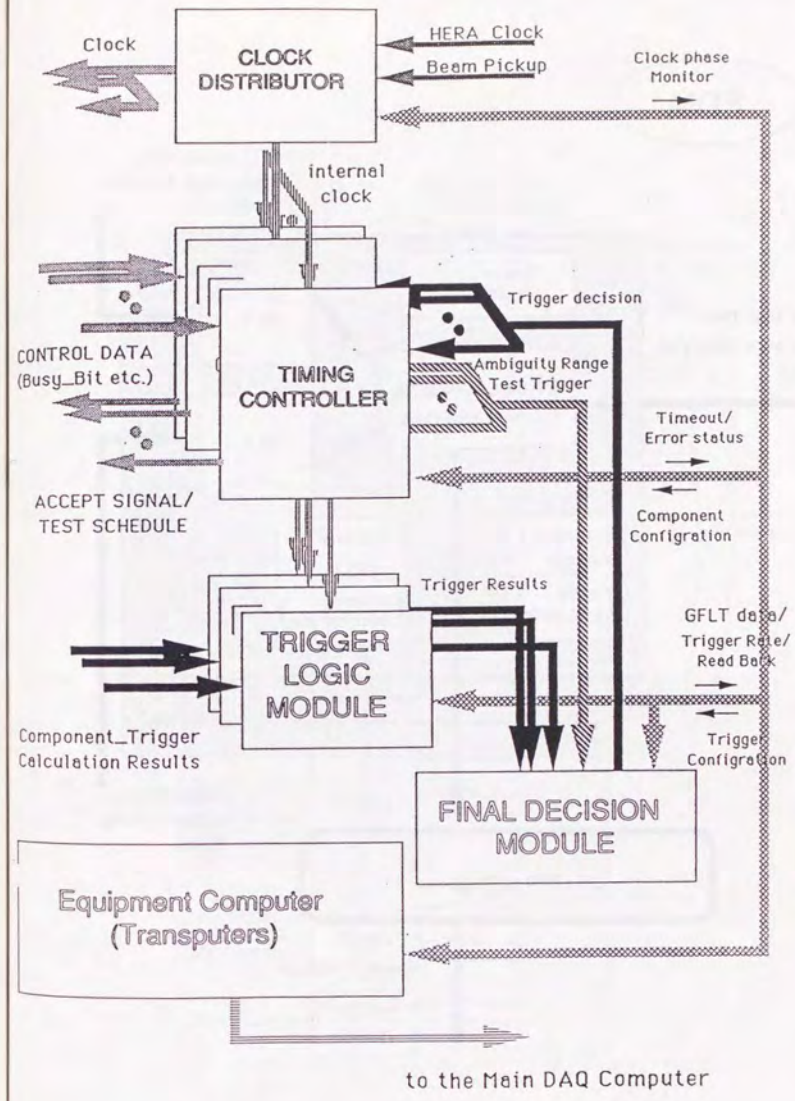

Figure 4.3: A block diagram of the GFLT hardware.

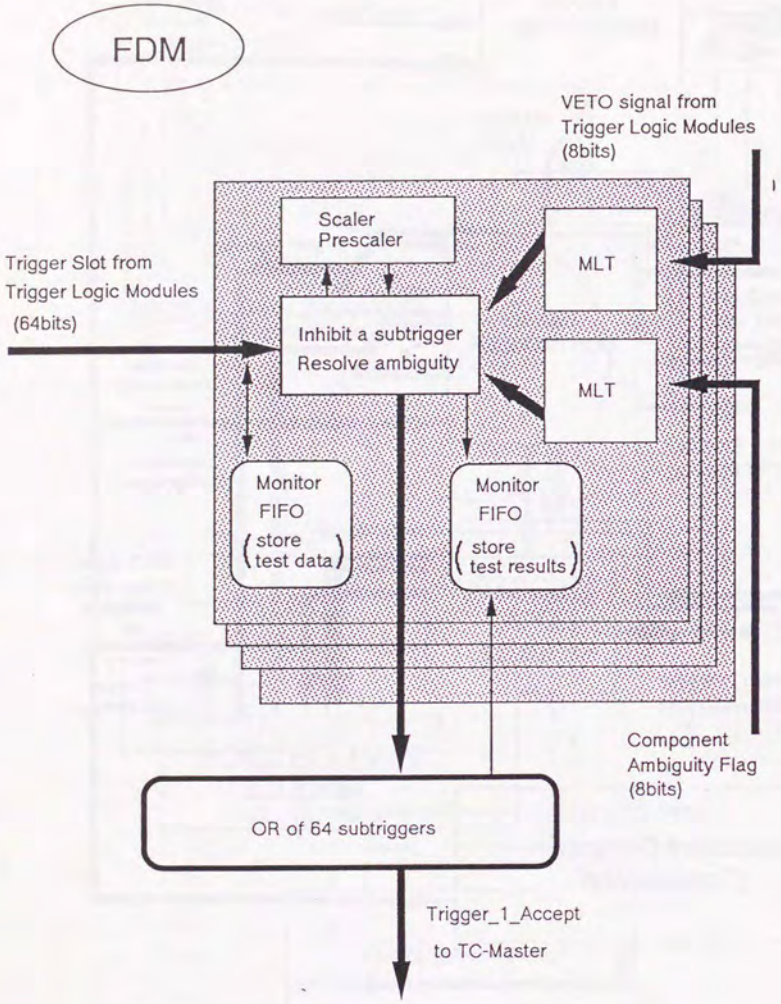

Figure 4.4: Block diagram of Final Decision Module (FDM).

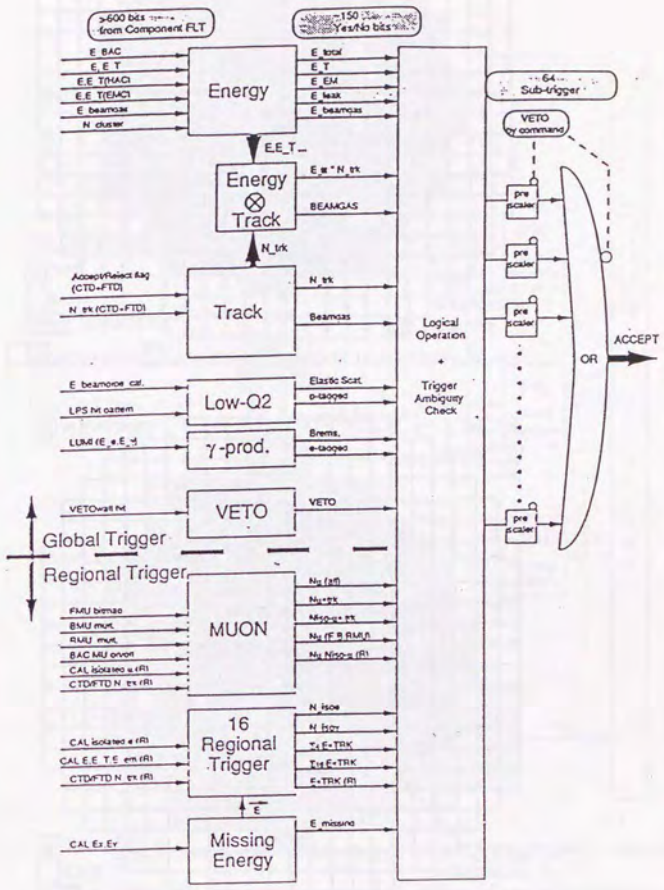

Figure 4.5: Schematic logic of the GFLT.

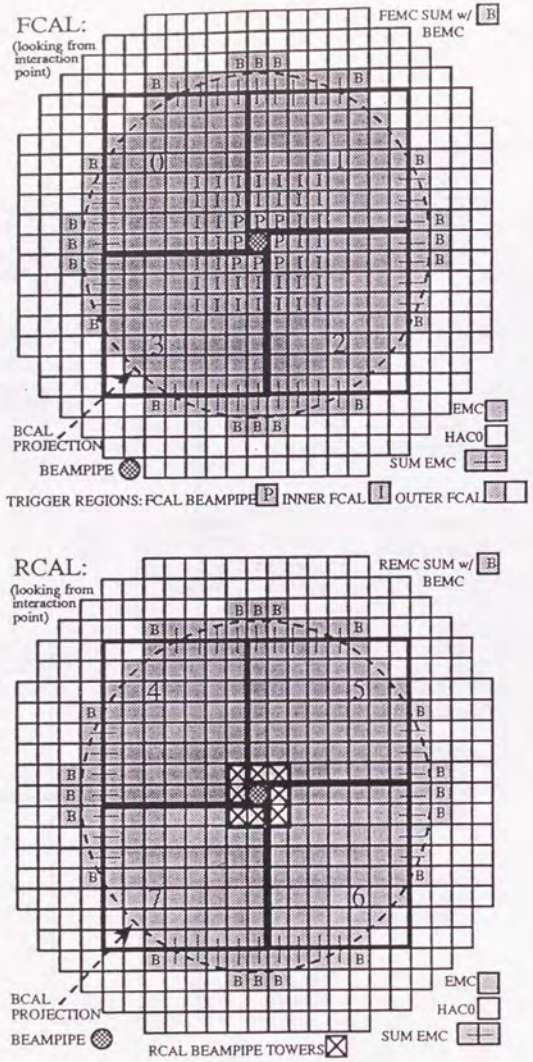

Figure 4.6: FCAL and RCAL trigger regions.

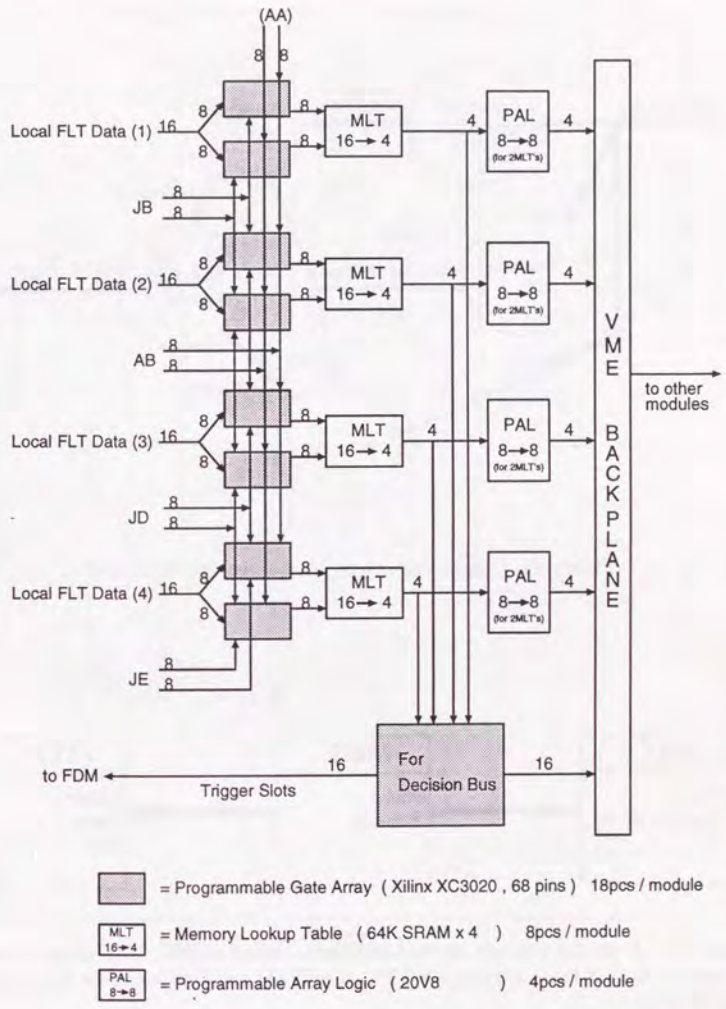

Figure 4.7: Architecture of Trigger Logic Module (TLM). The numbers in the figure indicate the number of I/O bits.

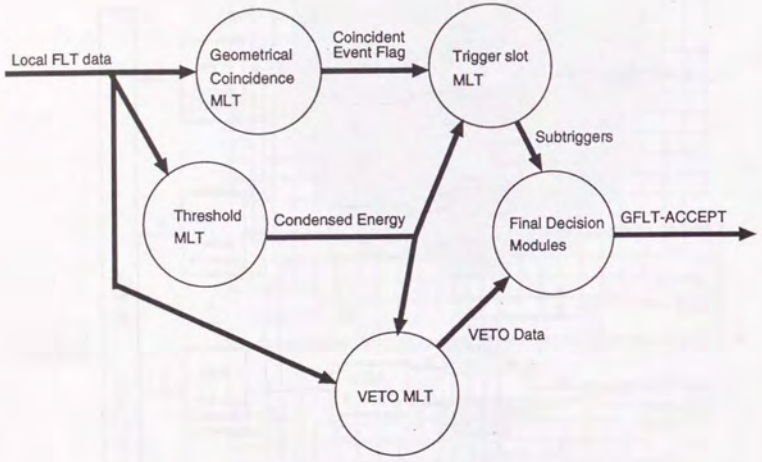

Figure 4.8: Conceptual design for the network of MLT's.

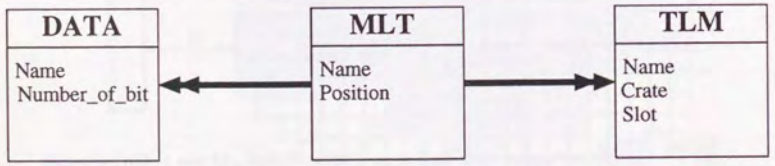

Figure 4.9: A simple example of the entity-relationship model. The diagram can be interpreted as that there are many MLT's on a TLM, and DATA can be distributed to many MLT's.

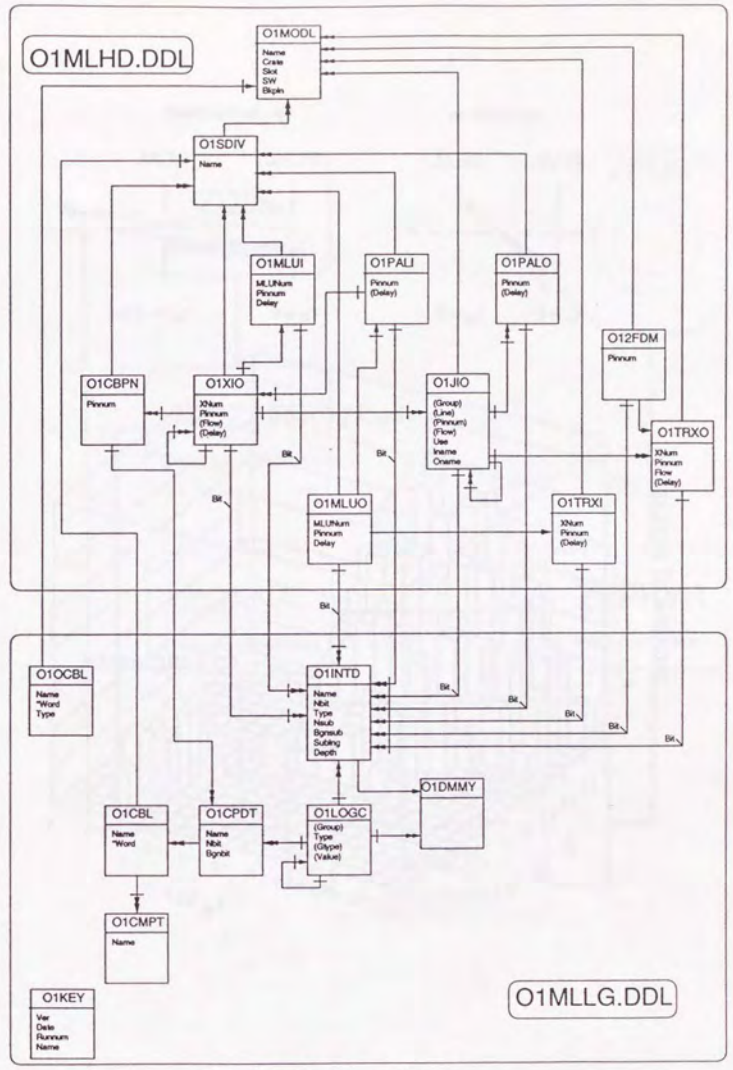

GFLT-MLT-ERD

Figure 4.10: Entity Relationship Diagram for the GFLT online logic database.

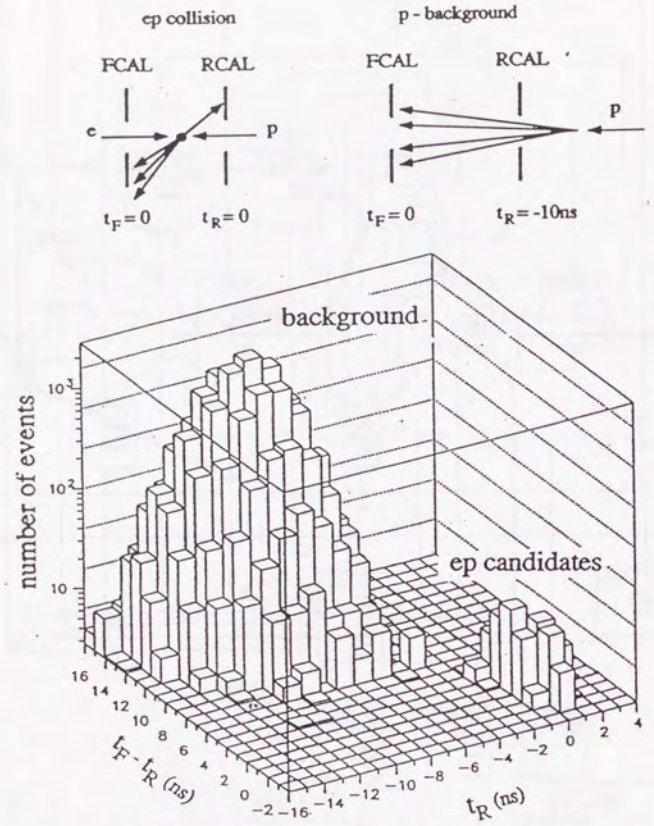

Figure 4.11: A plot of the difference of FCAL and RCAL time versus RCAL time.

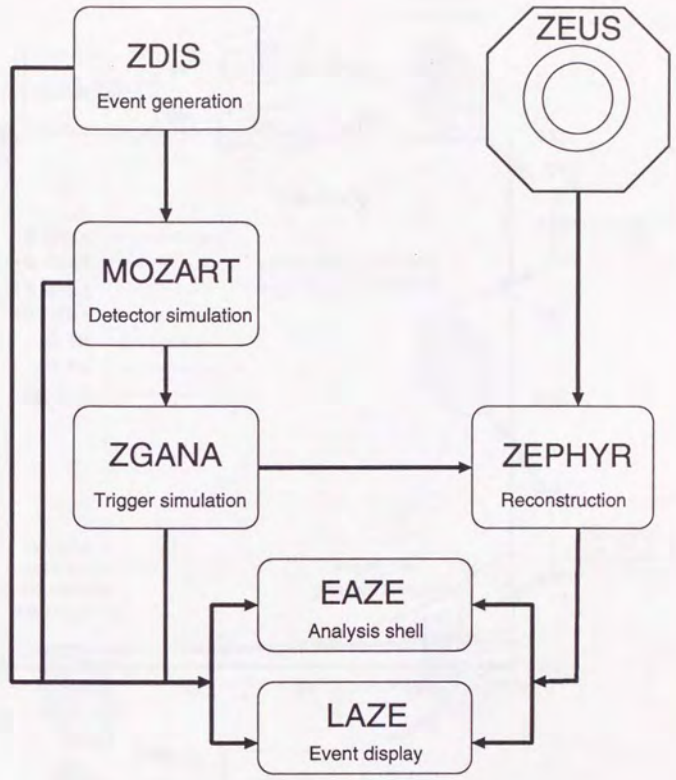

Figure 5.1: Data flow diagram of the Monte Carlo simulation of the ZEUS experiment.

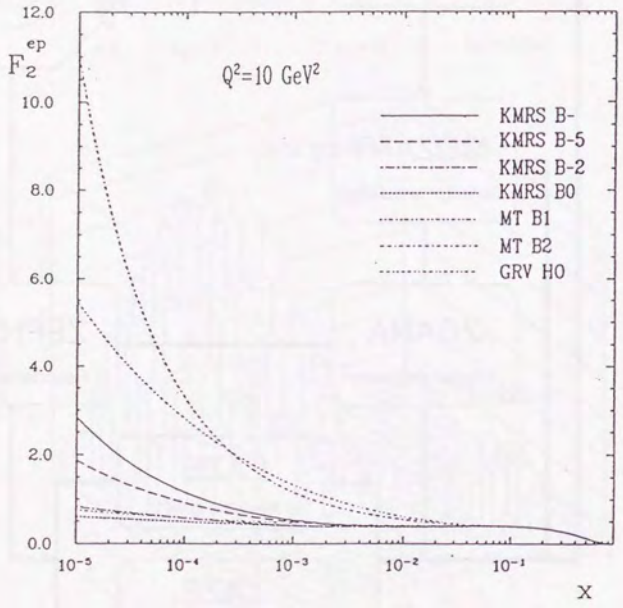

Figure 5.2: Various predictions of the structure function F_2 as a function of x at $Q^2 = 10GeV^2$.

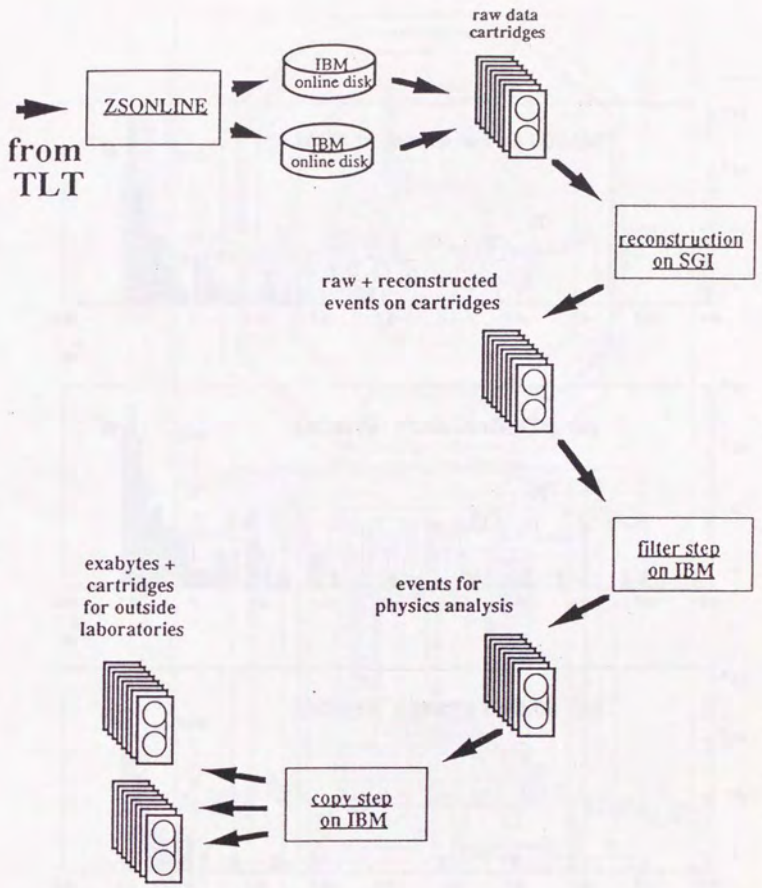

Figure 6.1: The data processing procedure for reconstruction and pre-selection to make data summary tapes (DST's).

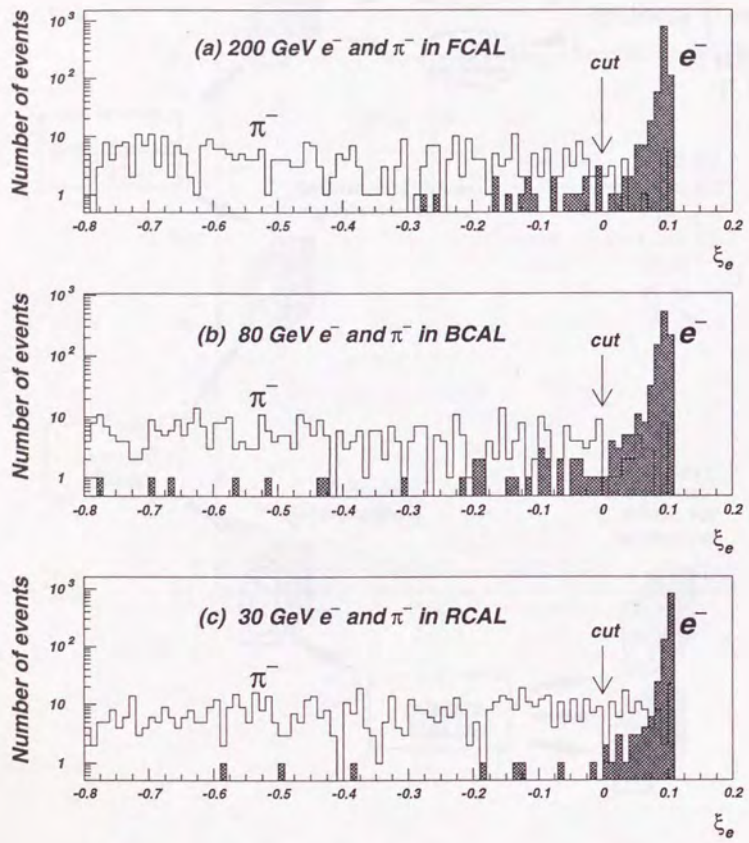

Figure 6.2: e/π separation in the refined electron finder. The definition of the variable, ξ_e, is $\xi_e \equiv min(0.1, T_e - 0.6) - L_e$, where T_e and L_e are measures for transverse and longitudinal energy spread of the electromagnetic cluster found in CAL. The selection criterion, $\xi_e \geq 0$, efficiently separates electrons from pions.

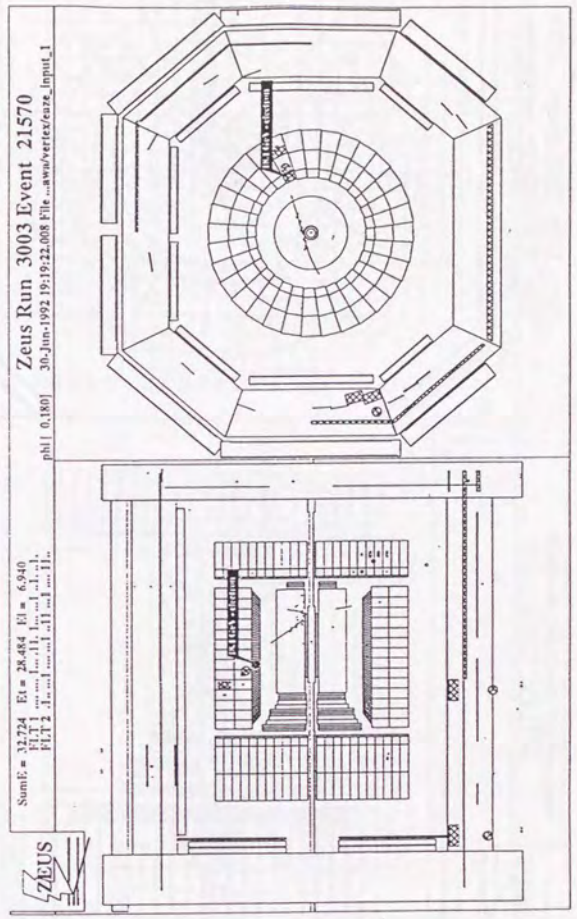

Figure 6.3: A picture of a typical cosmic-ray event which survived the exotics-preselection.

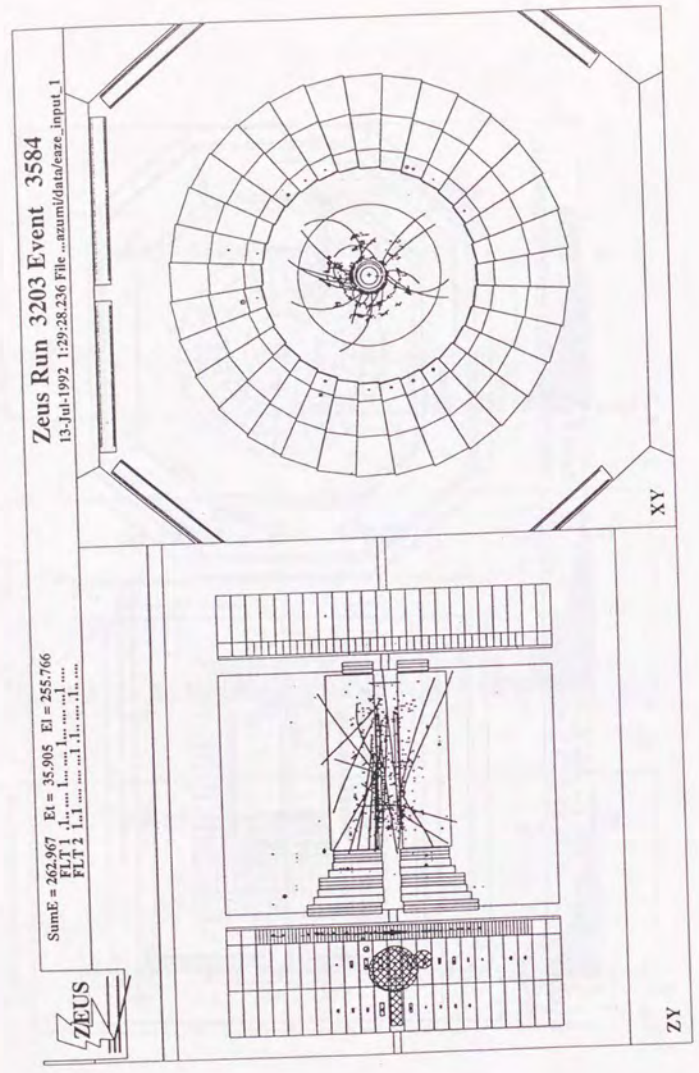

Figure 6.4: A picture of a typical proton-gas event which survived the exotics-preselection.

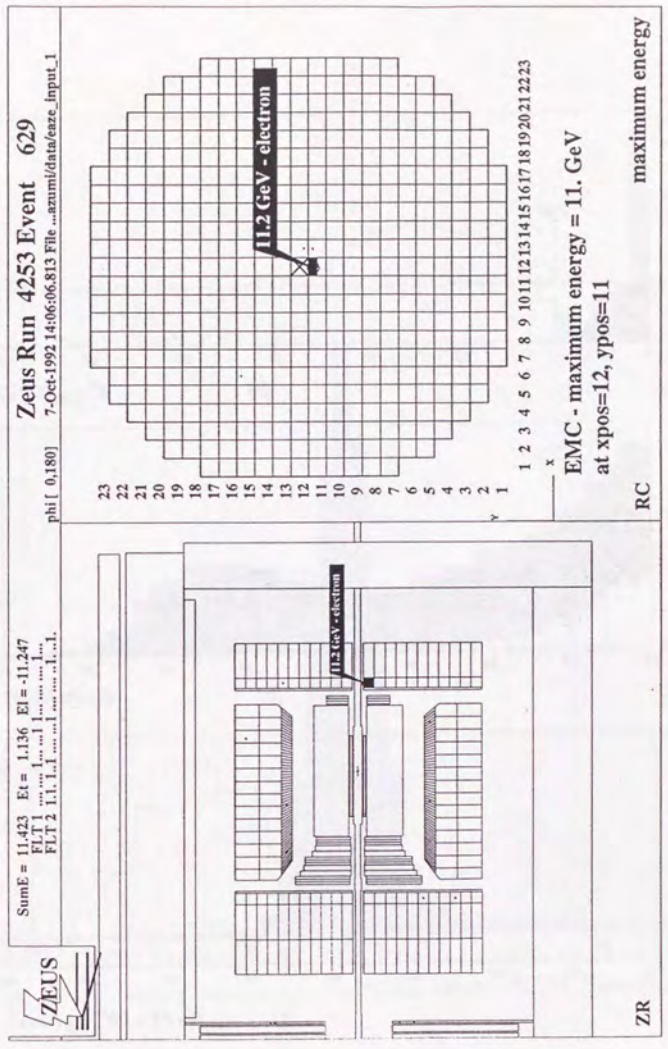

Figure 6.5: A picture of a typical electron-gas event which survived the exotic-s-preselection.

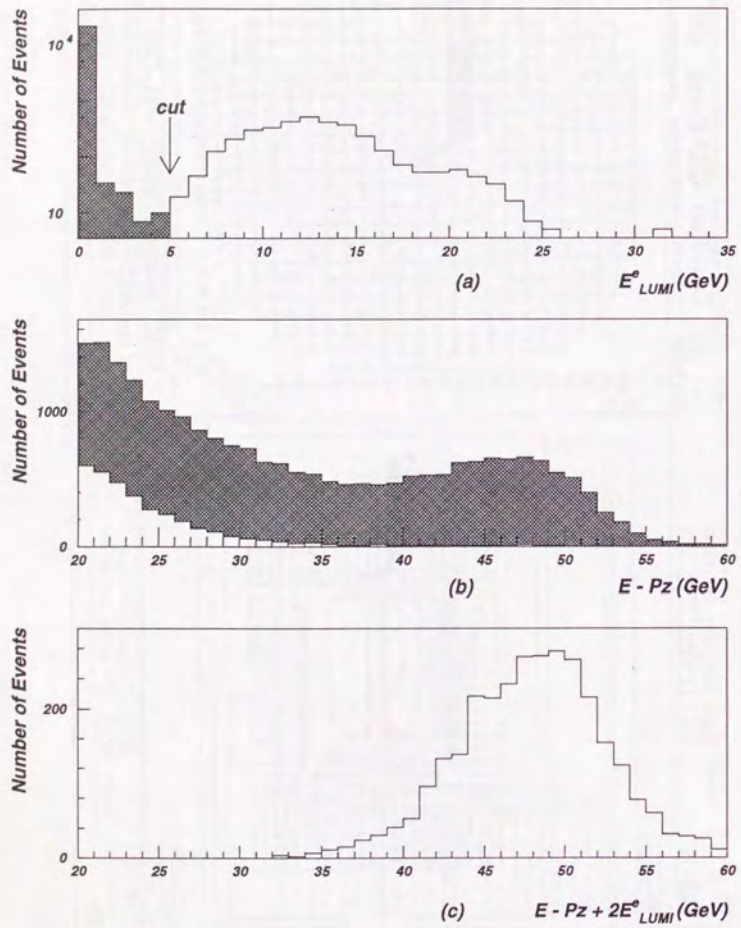

Figure 6.6: (a) Energy distribution in LUMI EDET for pre-selected NC samples on the collision bunches. Events in the shaded area (with $E^e_{LUMI} < 5$GeV) were saved. (b) δ $(= E - P_z)$ distribution for the rejected events (the non-shaded area) and the saved events (the shaded area). (c) Distribution of $E - P_z + 2E^e_{LUMI}$ for the rejected events.

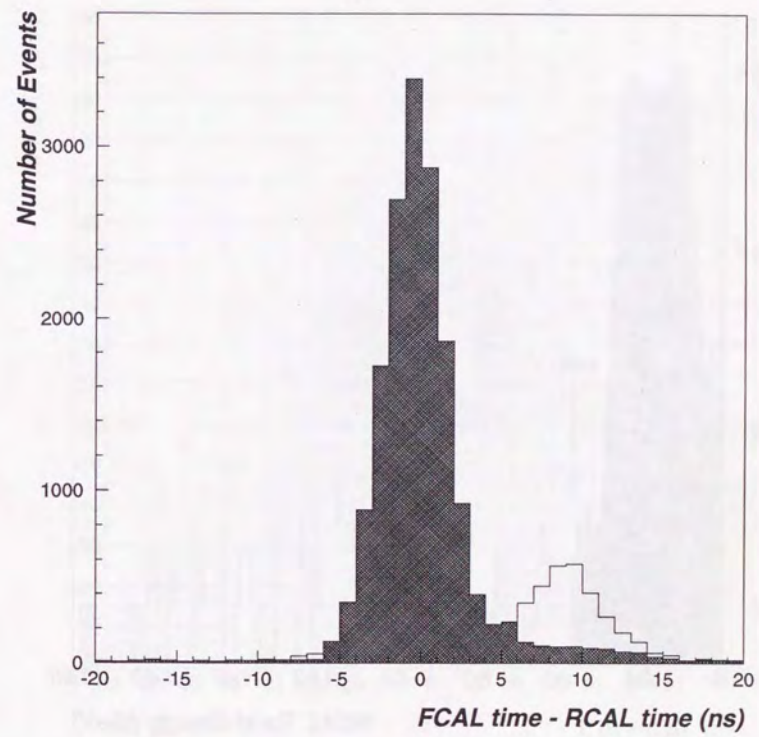

Figure 6.7: FCAL time - RCAL time (with energy in each PMT > 80 MeV) before and after the final timing cuts. Events in the shaded area are saved.

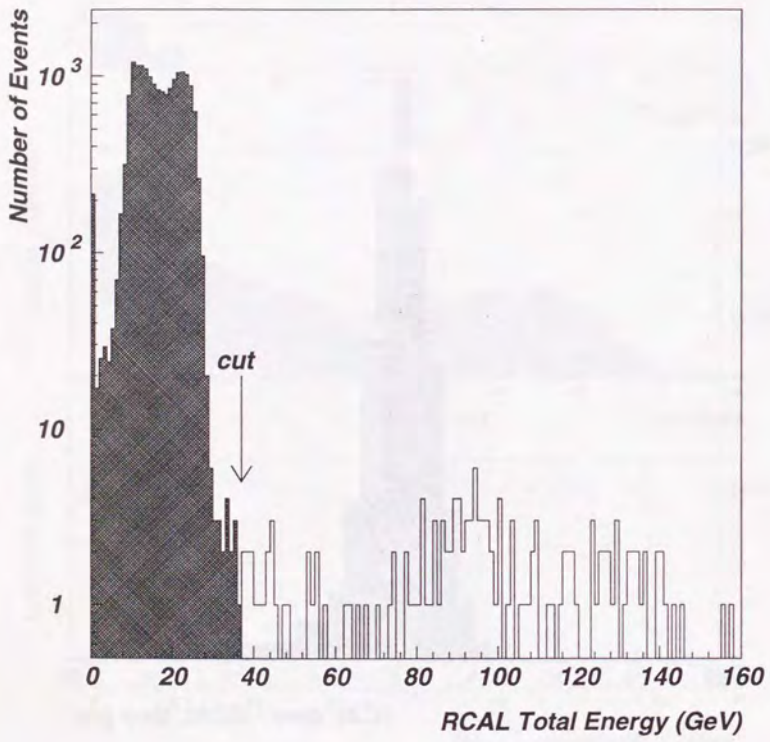

Figure 6.8: RCAL total energy distribution after final timing cuts. Events having RCAL total energy greater than the kinematical limit (=37GeV) are rejected.

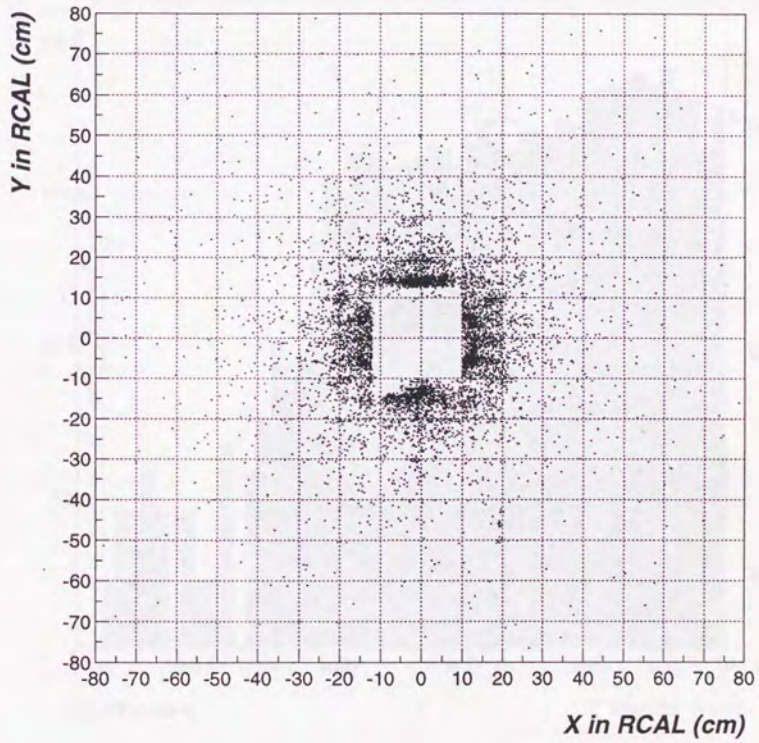

Figure 6.9: Impact position of electrons in RCAL before the electron position cut.

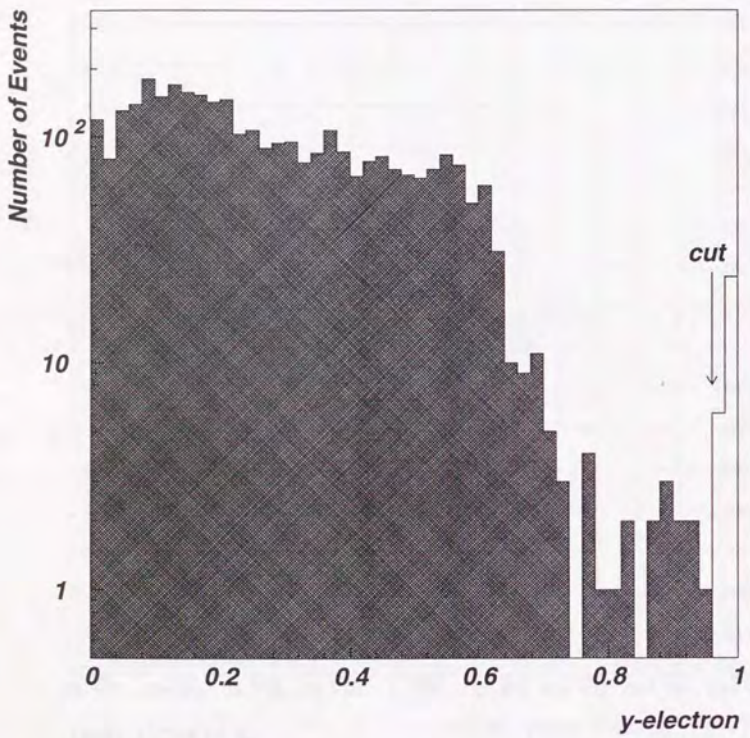

Figure 6.10: Distribution of y_e. A peak at $y_e \sim 1$ is due to fake electrons. Events in the shaded area ($y_e < 0.96$) were saved.

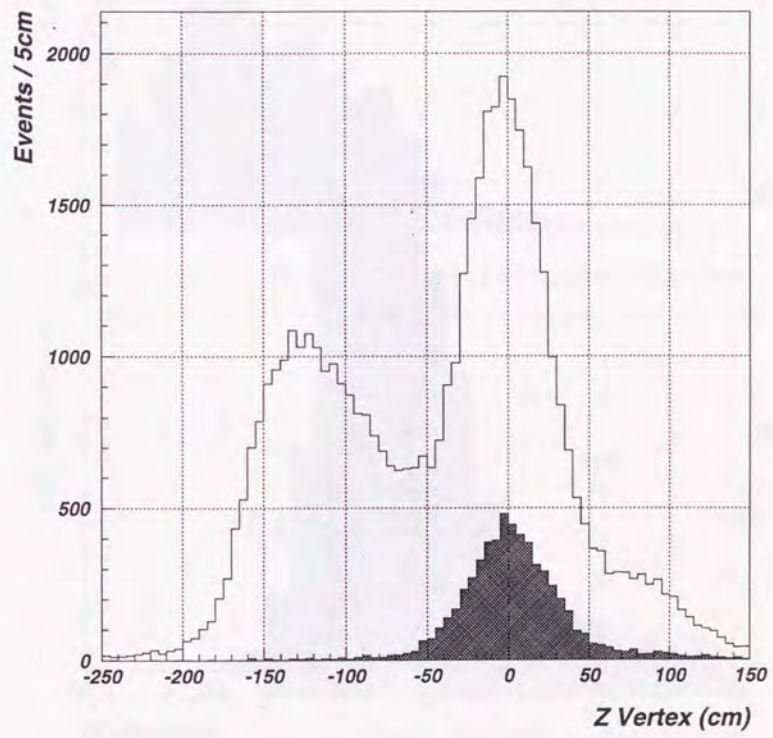

Figure 6.11: Z distribution of event vertices for preselected NC samples. The shaded area shows NC candidates after electron energy and position cuts.

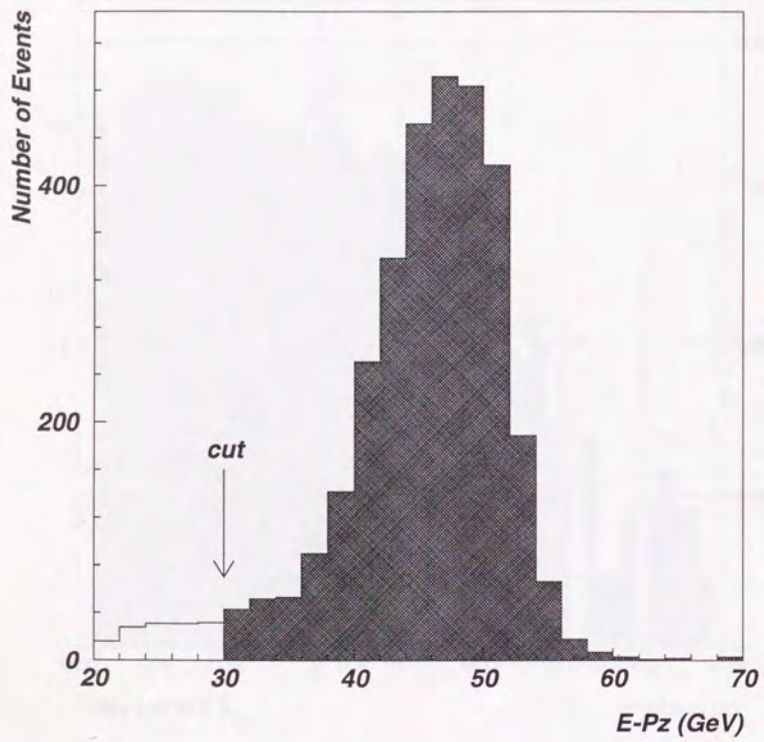

Figure 6.12: Distribution of $\delta\ (E - P_z)$. Events in the shaded area were saved.

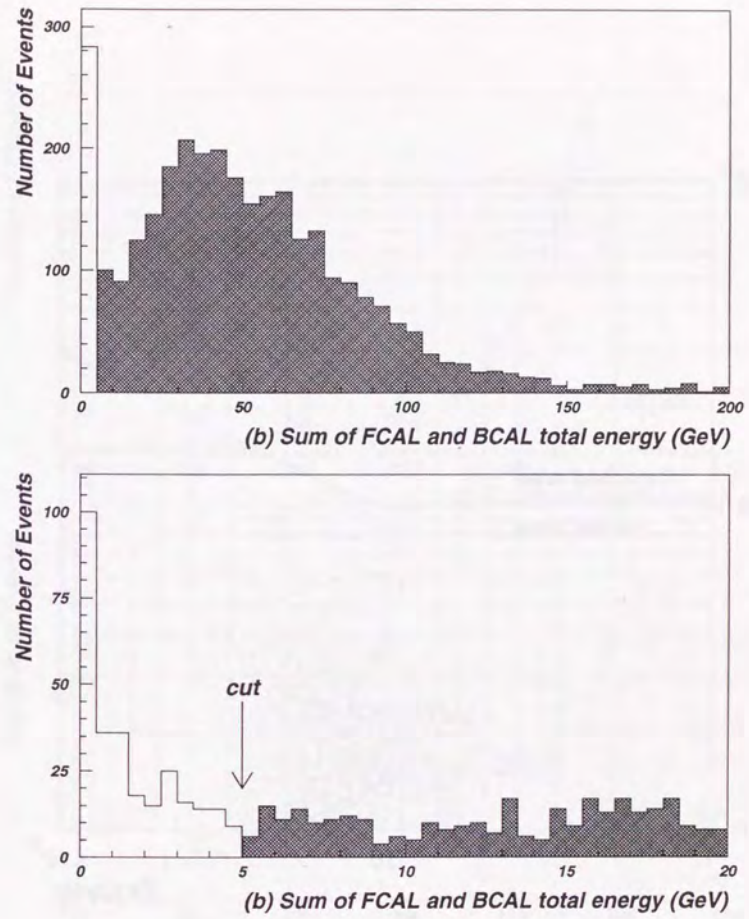

Figure 6.13: Distribution of the sum of FCAL and BCAL total energy. The upper graph (a) shows the distribution from 0 GeV to 200 GeV. The lower graph (b) is a closer look between 0 GeV to 20 GeV. A cut on 5 GeV was applied and events in the shaded area were saved.

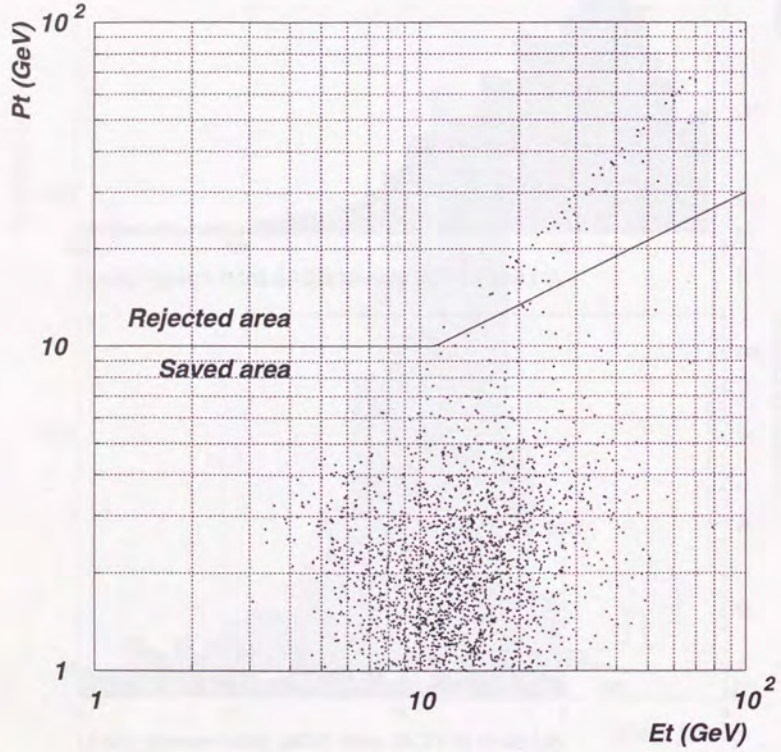

Figure 6.14: P_t vs. E_t. Events below the solid line were saved.

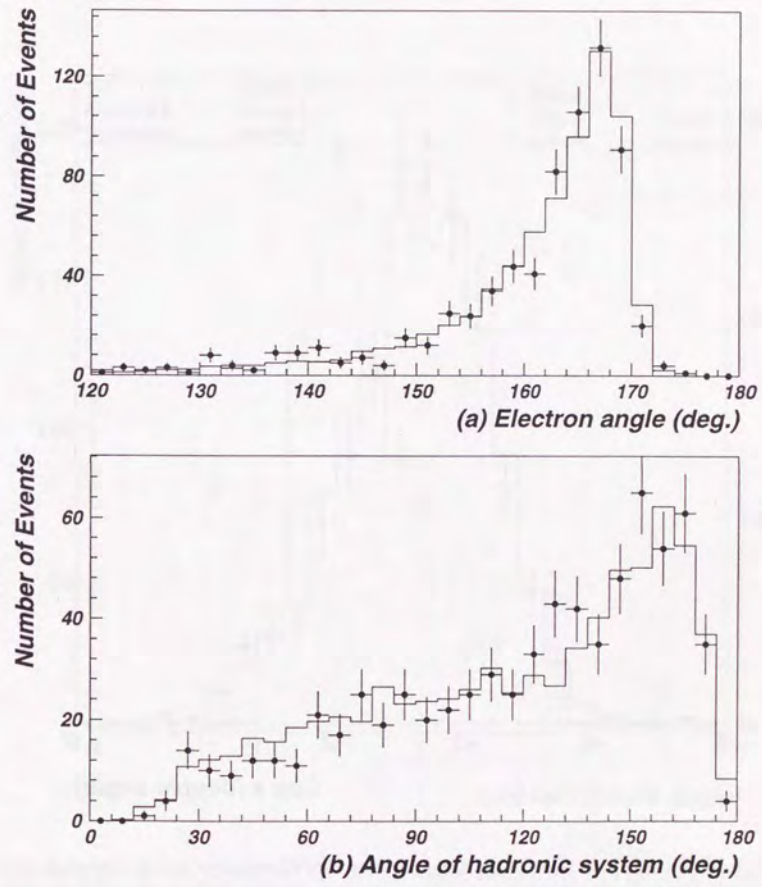

Figure 6.15: (a) Angular distribution of scattered electrons in the NC samples. (b) Angular distribution of the final hadronic system. The data are shown as points with statistical errors and Monte Carlo expectation is shown by the histogram.

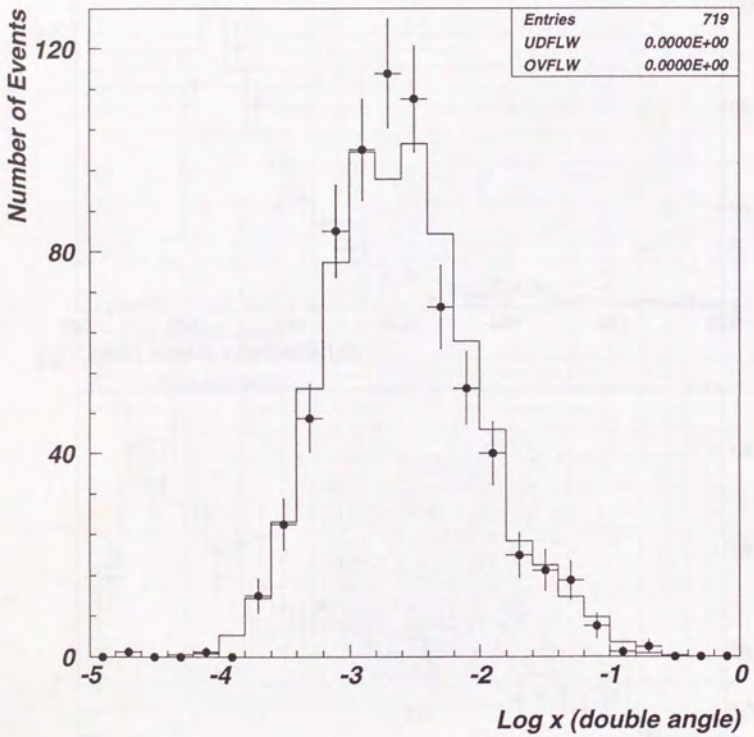

Figure 6.16: Bjorken x by the double angle method for NC samples (points with statistical errors) and Monte Carlo expectation (histogram) normalized with the measured integrated luminosity.

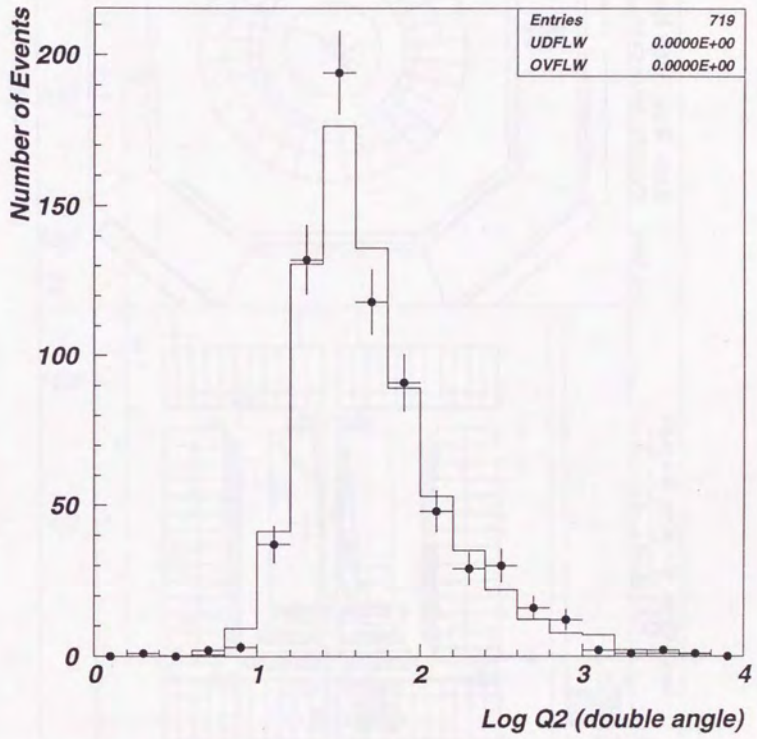

Figure 6.17: Q^2 (in GeV^2) by the double angle method for NC samples (points with statistical errors) and Monte Carlo expectation (histogram) normalized with the measured integrated luminosity.

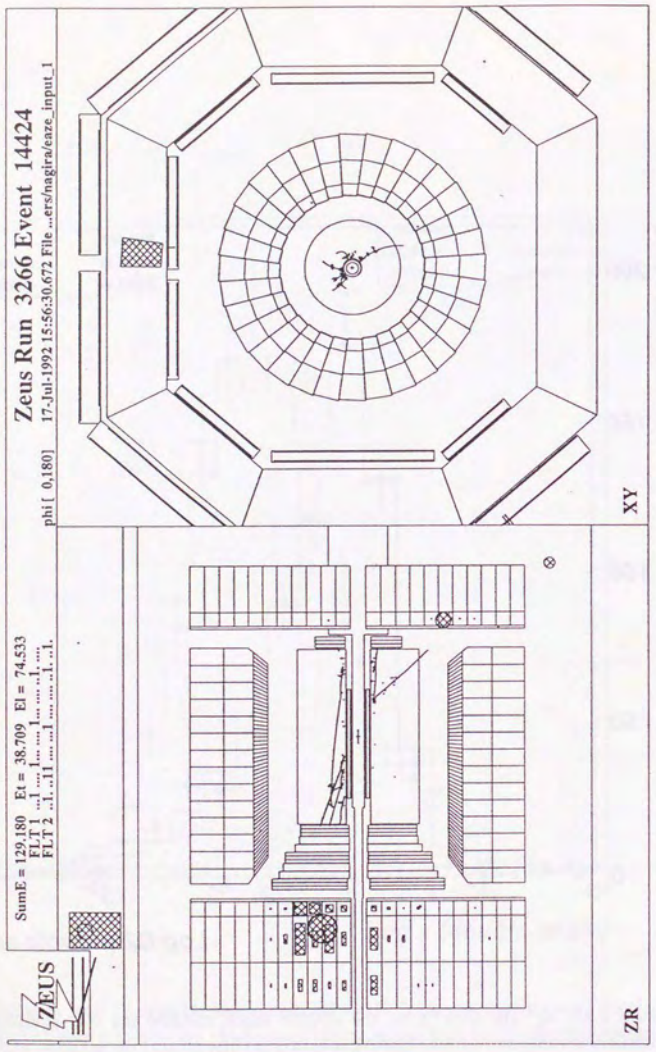

Figure 6.18: A picture of a typical NC event.

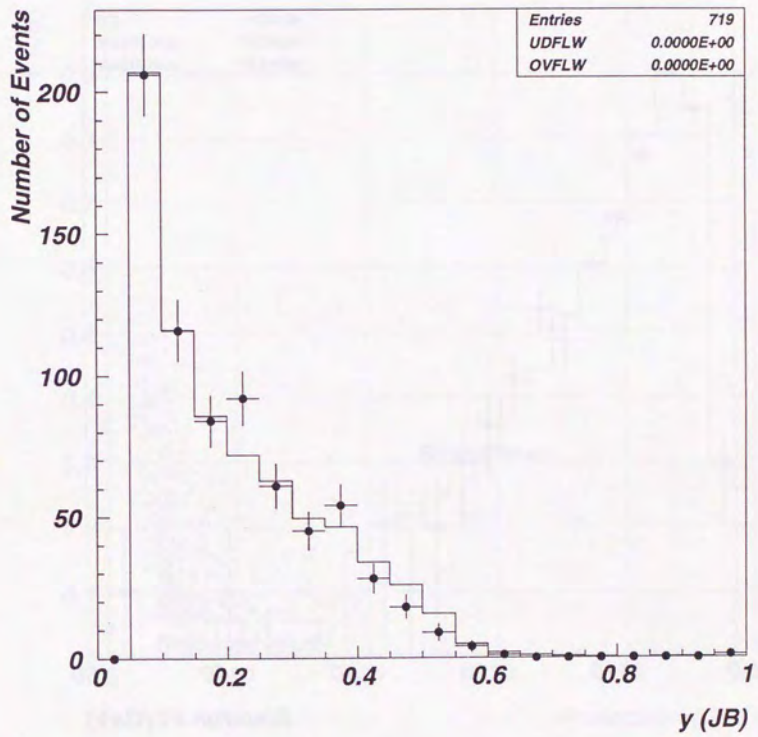

Figure 6.19: Distribution of y_{JB} for NC samples (points with statistical errors) and Monte Carlo expectation (histogram).

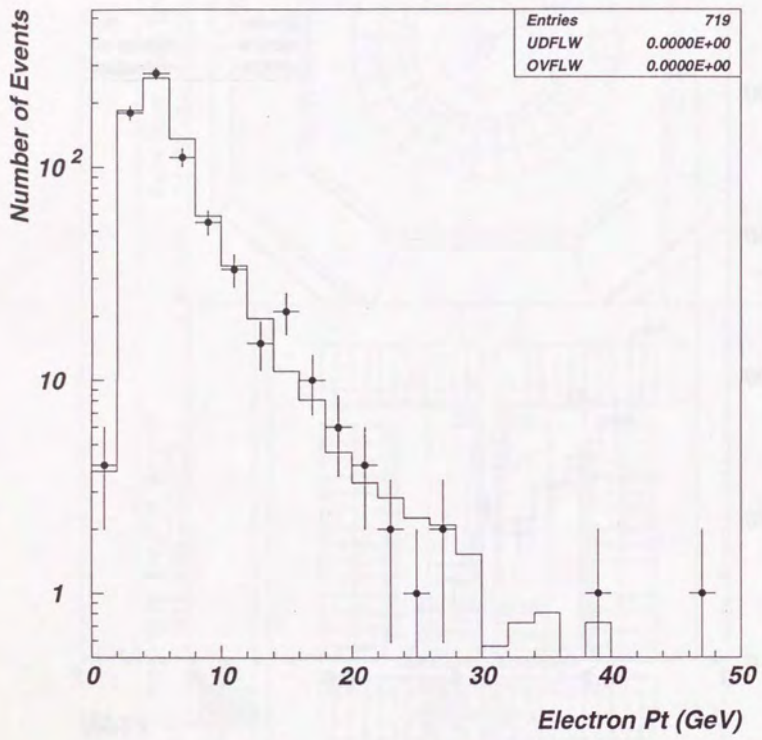

Figure 6.20: Distribution of electron Pt for NC samples (points with statistical errors) and Monte Carlo expectation (histograms).

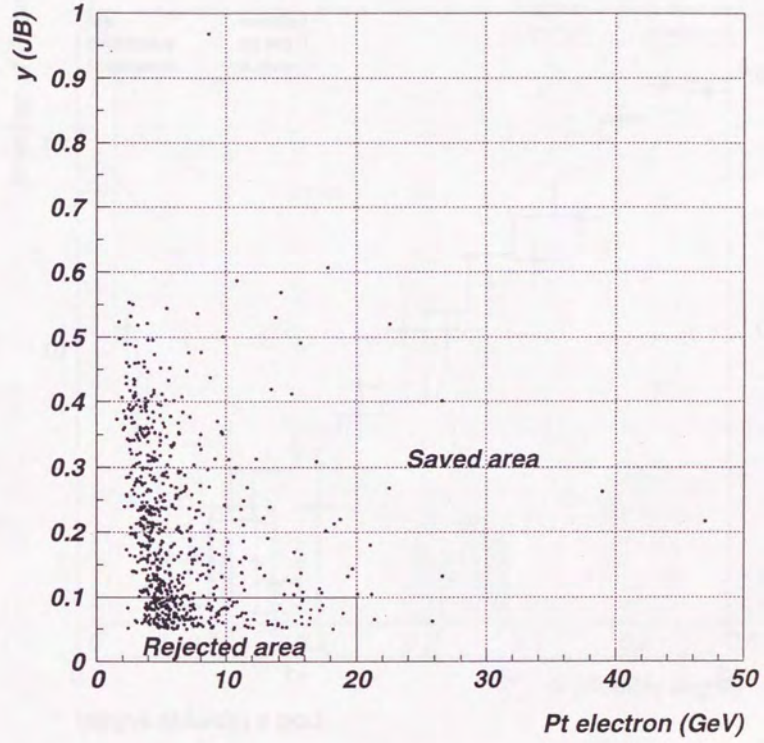

Figure 6.21: NC samples in y_{JB} vs. electron Pt (P_t^{elec}) plane. Events with $y_{JB} > 0.1$ or $P_t^{elec} > 20$GeV were saved.

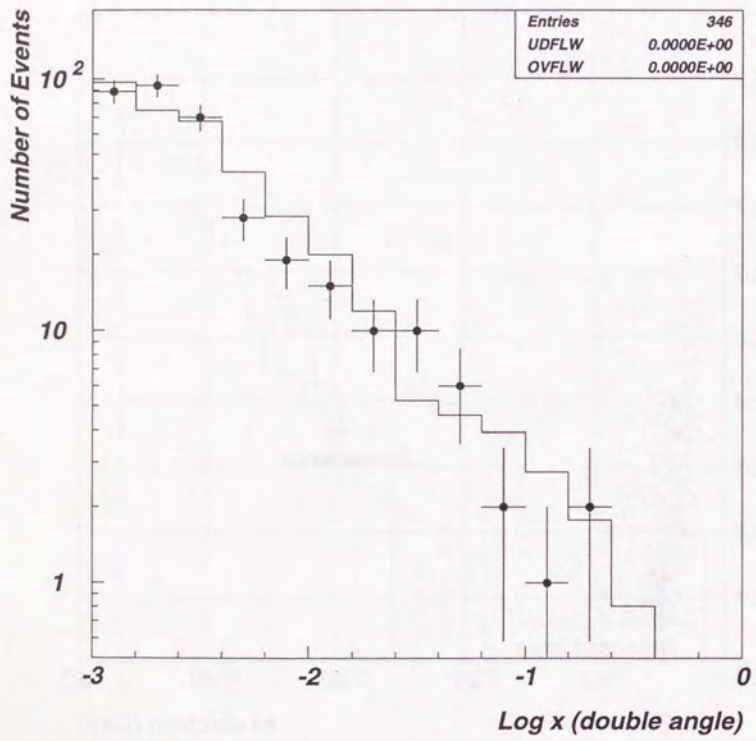

Figure 6.22: Bjorken x by the double angle method for LQ search samples (points with statistical errors) and Monte Carlo data (histogram).

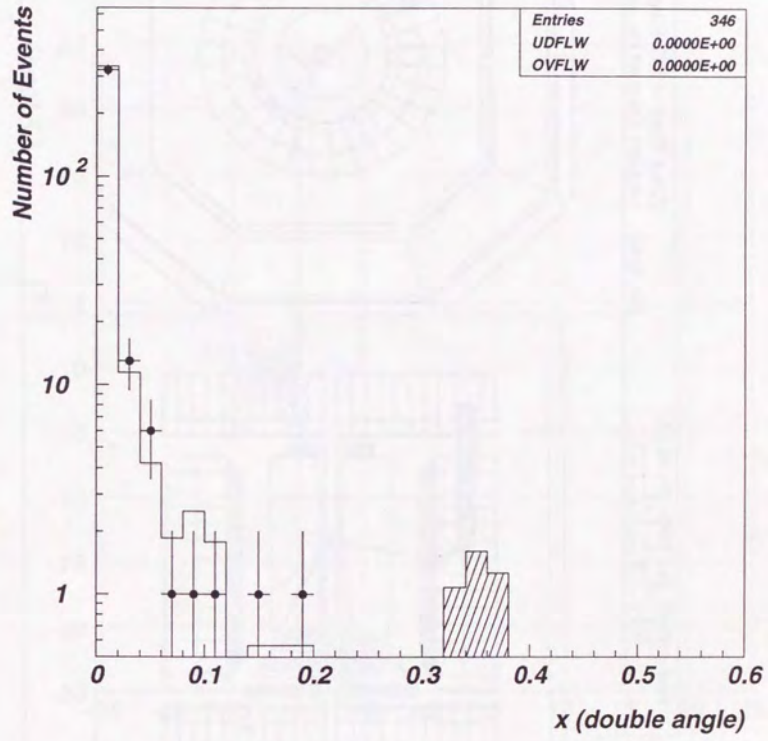

Figure 6.23: x_{DA} for LQ search samples (points with statistical errors) and Monte Carlo NC data (histograms). The displayed range $0 \leq x_{DA} \leq 0.6$ corresponds to $0 \leq M_{LQ} \leq 230GeV$. No event is found in $x_{DA} > 0.2$ (or $M_{LQ} > 130GeV$). The expected LQ signal (for S_0) with $M_{LQ} = 175GeV$, $g_R = 0.31$, $g_L = 0$ is shown as the shaded histogram.

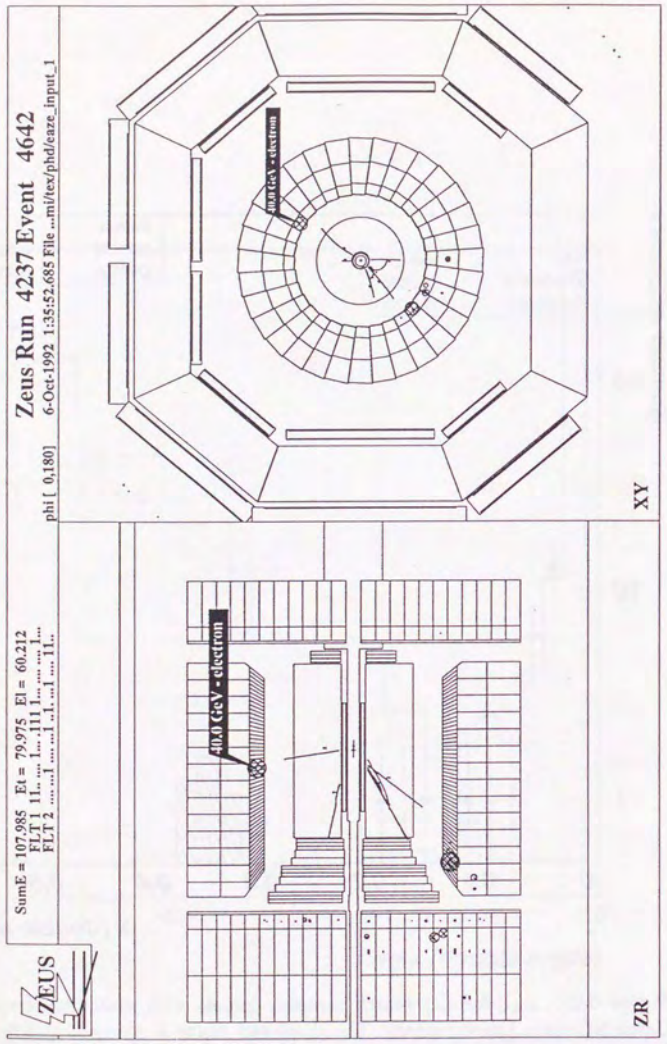

Figure 6.24: A high-x, high-Q^2 event in the LQ search samples.

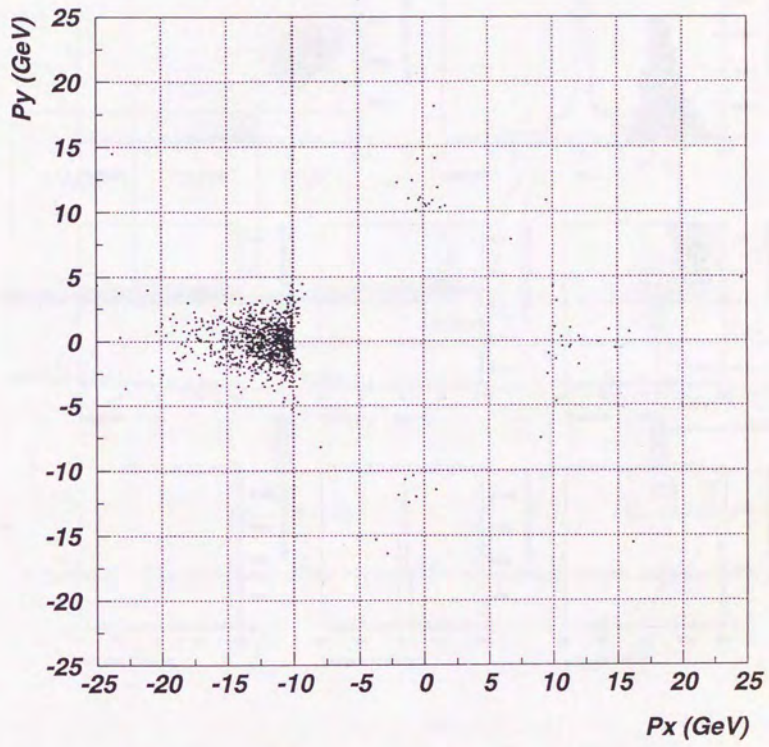

Figure 6.25: Py vs. Px for CC candidates after vertex cut. The Px asymmetry is due to the activity on the C4 collimator.

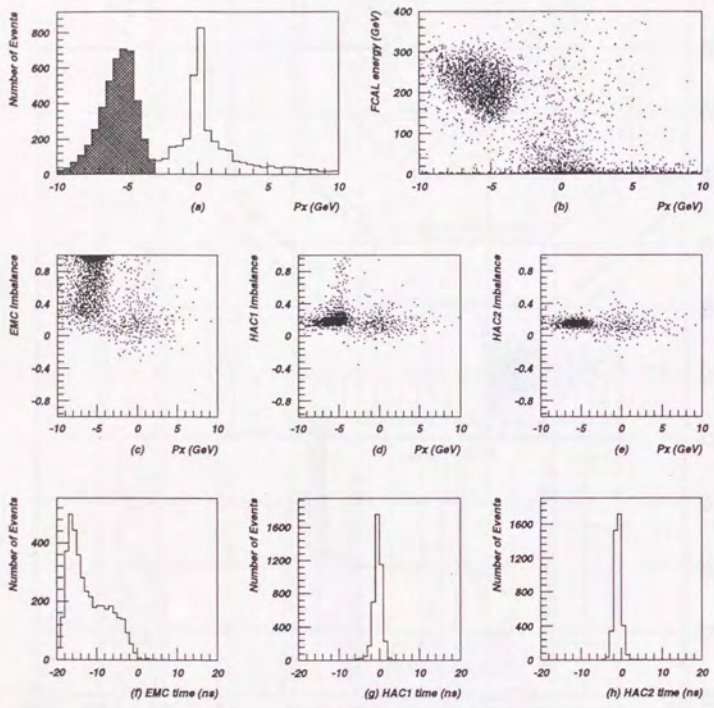

Figure 6.26: Various distributions related to the background events due to the activity on C4. (a) Px distribution. In addition to a primary peak at centered at 0, a secondary peak (shaded) at ~ -5GeV is also seen. (b) FCAL energy vs. Px. (c)(d)(e) Left-right energy imbalance of the most energetic EMC, HAC1, HAC2 towers, respectively. (f)(g)(h) Time distributions for the same towers.

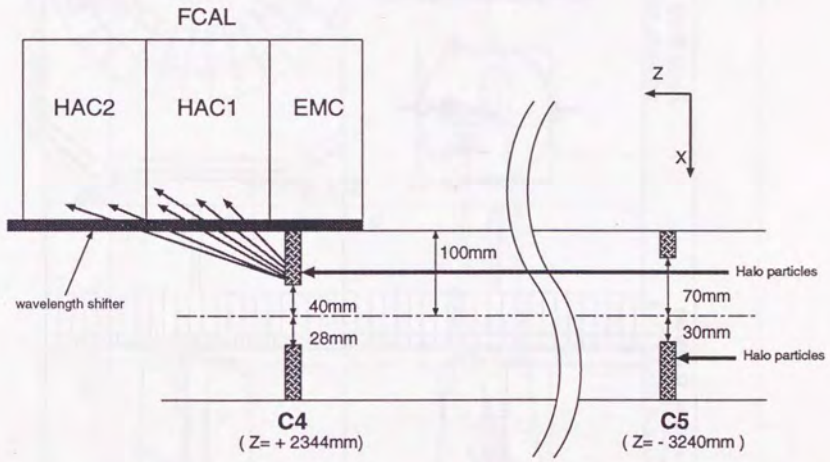

Figure 6.27: The schematic of the origin of Px asymmetry. Beam halo particles hit the C4 collimator.

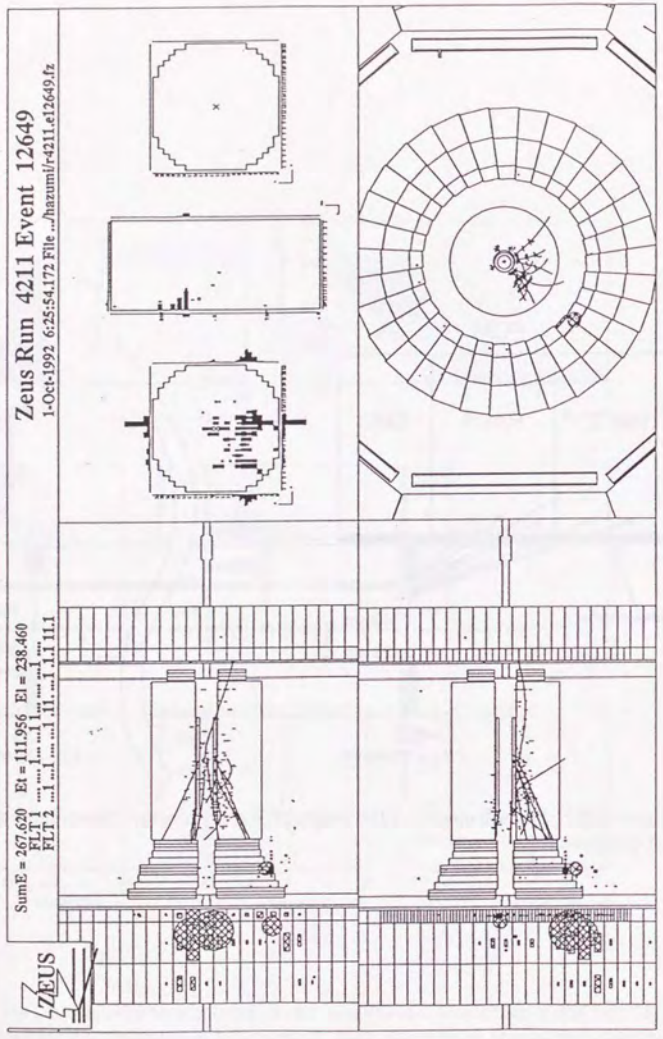

Figure 6.28: A picture of the CC candidate with the highest $Q^2(\sim 10^4 GeV^2)$.

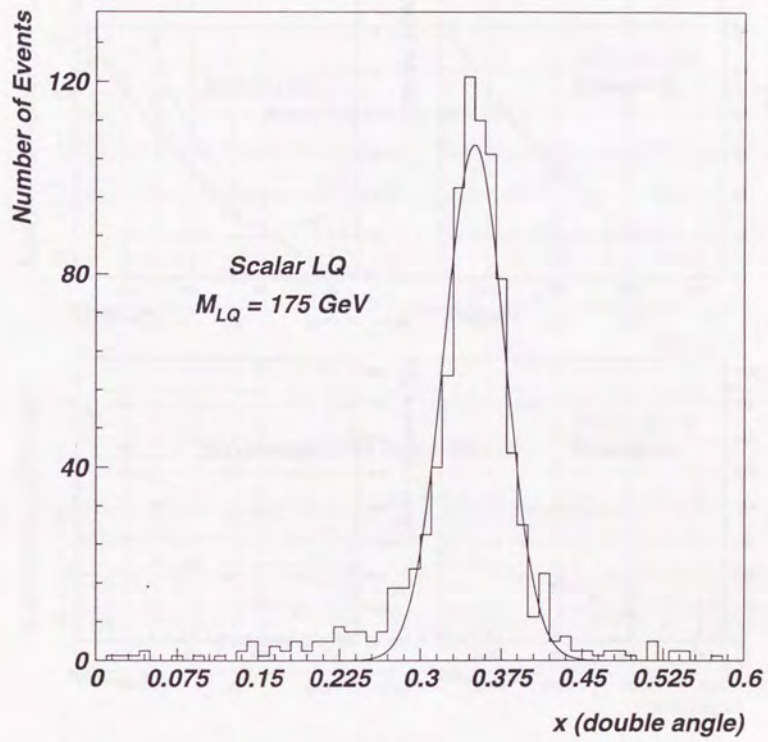

Figure 7.1: The x_{DA} distribution for scalar LQ $\rightarrow$ eq with $M_{LQ} = 175GeV$. Also a Gaussian fit to the peak is shown. From the fit, the mean (=0.35) and the standard deviation (=2.8×10^{-2}) are obtained.

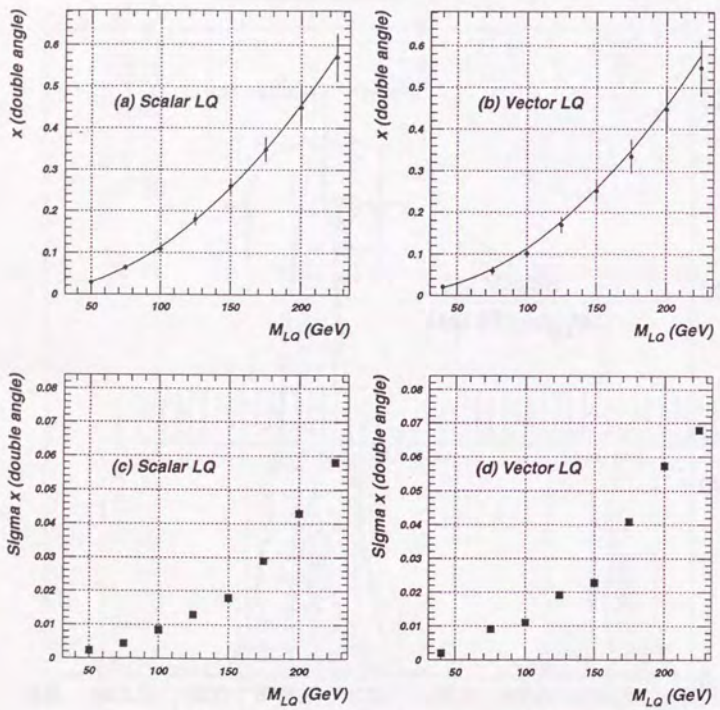

Figure 7.2: (a) Mean of x_{DA} vs. M_{LQ} for scalar LQ. The error bar on each point is the standard deviation obtained by the Gaussian fitting. The solid line is for $x_{DA} = M_{LQ}^2/s$. (b) The same for vector LQ. (c) Standard deviation of the x_{DA} distribution for scalar LQ. (d) The same for vector LQ.

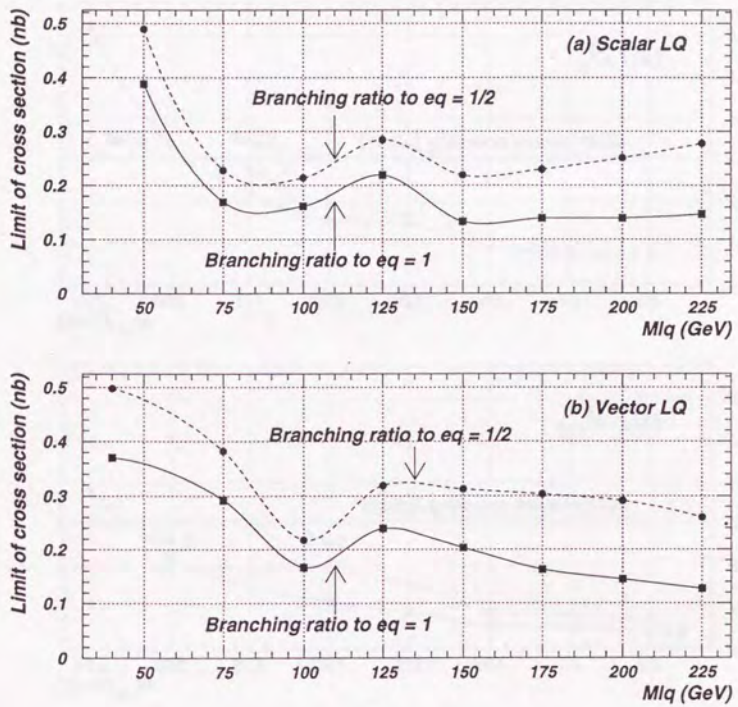

Figure 7.3: The 95% confidence upper limits on the cross sections of LQ. (a) Scalar Leptoquarks. (b) Vector Leptoquarks.

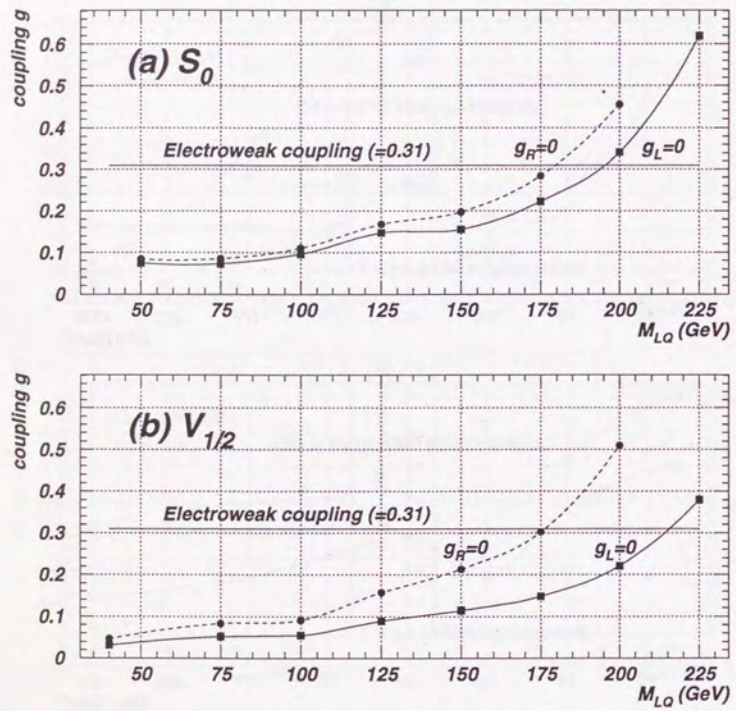

Figure 7.4: The 95% confidence upper limits on the couplings of LQ. (a) Scalar Leptoquark S_0. (b) Vector Leptoquark ($V_{1/2}$).